Towards the Engineering of Pulsed Photoconductive Antennas

Garufo, Alessandro

DOI
10.4233/uuid:3850fd4d-9256-4925-88bb-9679da5f3aaf

Publication date
2017

Document Version
Final published version

Citation (APA)
Garufo, A. (2017). *Towards the Engineering of Pulsed Photoconductive Antennas*. [Dissertation (TU Delft), Delft University of Technology]. https://doi.org/10.4233/uuid:3850fd4d-9256-4925-88bb-9679da5f3aaf

Towards the Engineering of Pulsed Photoconductive Antennas

Towards the Engineering of Pulsed Photoconductive Antennas

PROEFSCHRIFT

ter verkrijging van de graad van doctor
aan de Technische Universiteit Delft,
op gezag van de Rector Magnificus Prof. ir. K.C.A.M. Luyben,
voorzitter van het College van Promoties,
in het openbaar te verdedigen op donderdag 01 juni 2017 om 10:00 uur

door

Alessandro GARUFO

Master of Science in Telecommunications Engineering,
Università degli studi di Siena, Italië,
geboren te Rome, Italië.

This dissertation has been approved by the:

promotor: prof. dr. ir. A. Neto
copromotor: dr. ir. N. Llombart

Composition of the doctoral committee:

Rector Magnificus	Chairman
Prof. dr. ir. A. Neto,	Delft University of Technology
Dr. ir. N. Llombart,	Delft University of Technology
Independent members:	
Prof. dr. P. Siegel,	California Institute of Technology, United States
Prof. dr. J. Stake,	Chalmers University of Technology, Sweden
Dr. ir. P. de Maagt,	European Space Agency, Netherlands
Prof. dr. ing. A. Freni,	University of Florence, Italy
Prof. dr. ir. P. M. Sarro,	Delft University of Technology, Netherlands
Reserve member:	
Prof. dr. ir. L. C. N. de Vreede,	Delft University of Technology, Netherlands

European Research Council

Established by the European Commission

The work presented in this thesis has been performed at TU Delft and financed by the European Research Council starting grants ERC-2011-StG Grant AAATSI 278794.

Keywords: photoconductivity, photoconductive antenna, THz source, THz technology, equivalent circuit, dispersion, leaky wave antenna, lens antenna, ultra-wideband antenna, ultra-wideband array.

Cover design by: Alessandro Garufo.

Printed by: Ipskamp Drukkers B.V., Enschede, Netherlands.

An electronic version of this dissertation is available at: http://repository.tudelft.nl/

ISBN 978-94-028-0657-1

To my family and Carol

Contents

Chapter 1

Introduction

In recent years, Terahertz (THz) technology has attracted the interest of researchers for its potential applications in a variety of domains. In particular, THz sensing has found application in security screening, medical imaging, spectroscopy, and non-destructive testing [1–15]. The emergence of all these applications has been driven by the availability of photoconductive antennas (PCAs), which have made available bandwidth in the THz spectrum at relatively low cost, thank to several breakthroughs in photonics, and semiconductor technology [16–23]. PCAs are optoelectronic electromagnetic sources that resort to optically pumped semiconductor materials. They exploit the photoconductivity phenomenon to generate and radiate power over a broadband up to the THz frequencies.

However, nowadays such devices suffer of low radiated power levels, which make them usable only in niche short-range applications (e.g. spectroscopy), and typically render slow the system (e.g. imaging system), in which are employed because of the long integration time involved in order to detect the radiated signal.

The ambition of this work is to solve this bottleneck by proposing some design strategies that could provide much higher power available from PCA sources. Early in this research project, it was understood that the key component that was limiting the design of THz sources was the lack of adequate tools comparable to those typically used by electrical engineers in lower frequency regime (i.e microwave frequencies).

In order to overcome such limitations, in this research project it has been developed a Thévenin or Norton equivalent circuit for the photoconductor generator of PCAs, providing a tool for analyzing the generation of the THz electromagnetic energy, and evaluating the average power radiated by PCAs. Moreover, the radiated power by the PCAs is heavily affected by the QO channel involved. Therefore, it is necessary an accurate analysis of the efficiency and dispersion of the PCAs radiation through the Quasi-Optical (QO) channel from the source to the detector involved. Hence, the tools to analyze such channel have been also developed. Thanks to both Norton equivalent circuit and the electromagnetic model of the QO channel, it is now possible to estimate the entire power budget from the source to the detector for the first time.

This research work is focused on the development of a Norton equivalent circuit for the photoconductor generator of PCAs, and the electromagnetic analysis of the radiation of

such devices through the QO channel by using such tools. The developed Norton equivalent circuit allows to evaluate the impedance of the equivalent generator of the photoconductive source, once that the electrical properties of the material, the features of the laser power, and the bias voltage are fixed.

Indeed, such equivalent circuit has been used to design a new array-type THz source, resorting to the concept of connected array [24–30]. Such solution can increase dramatically the amount of radiated power over the entire bandwidth, by avoiding the thermal failure of the device dividing high laser power among multiple feeding points. Moreover, the adoption of connected array minimizes the dispersion thanks to the intrinsic capacity of the proposed connected array structure to radiate broad band pulses without distortions.

The research developed within this work has been performed in the framework of the following research project *Advanced Antenna Architectures for THz Sensing Instruments* (AAATSI), which has been financed by the European Research Council, ERC-2011-StG Grant AAATSI no. 278794.

The research work presented in this thesis has led to a number of journal and conference publications, and an international patent listed on pp. 141–144.

1.1 Photoconductive Sources in THz Applications

THz sources have attracted significant attention in the recent time, because of the potential of the use of the THz regime in many applications. The terahertz frequencies are usually referred to the range from 0.3 THz to 3 THz [10], which lies between the microwave band and the infrared band, although different higher and lower limits can be found in the literature.
The terahertz emission has a smaller wavelength compared to the millimeter wave (MMW), as result THz imaging system can provide higher resolution than the MMW system. Molecules and crystals of materials have unique spectral fingerprints in the THz regime, making the use of THz radiation useful to identify materials unambiguously (e.g. THz spectroscopy system) [3]. Moreover, THz radiation is not affected by strong absorption into opaque materials as the optical frequencies, making it usable to detect concealed objects (e.g, THz imaging system) [31]. These features of the THz emission makes THz system useful for a large variety of practical applications (e.g. near-field imaging, tomography, packaging inspection, security, monitoring polymeric compounds, quality control of pharmaceutical products, and art conservation). This section gives an overview of the two main families of application on which the topic of this work is focused.

1.1.1 THz Time-Domain Spectroscopy (THz TDS) System

THz Time-Domain Spectroscopy (THz TDS) systems resort THz radiation to identify and analyze the physical properties of a wide variety of materials, tissue, and substances [1, 4–6, 11]. A general scheme of a THz TDS system is composed a THz emitter and detector; an optical system, which drives and focuses the laser excitation on the emitter

and the detector; and a reflectors chain, which guides the THz emission from the emitter to the detector, as it is illustrated in Fig. 1.1.

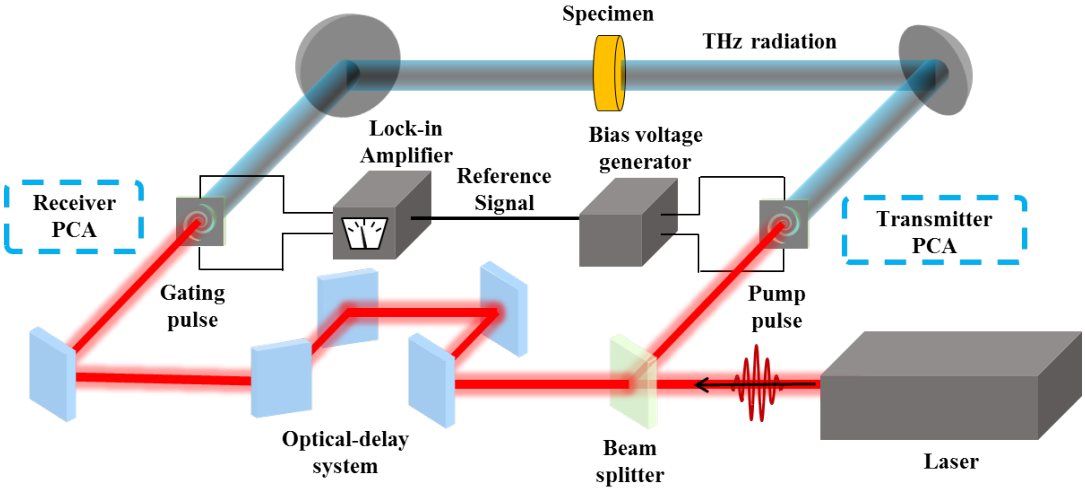

Figure 1.1: General scheme of a THz time domain spectroscopy (TDS) system.

The laser beam generated by a femtosecond pulsed laser is split in two beams, a pump beam and a probe beam. The emitter is a PCA, it is excited by the pump beam and it is biased by a voltage generator, which allows the generation of a pulsed current through the gap of the antenna, which in turn feeds the surrounding antenna. The bandwidth of such pulsed current is up to the THz frequencies, depending of the characteristic of the photoconductor material (e.g. LTG-GaAs [23, 32, 33], LTG-InGaAs [34], LTG-GaSb [35], LTG-InGaAs/InAlAs [36, 37]). The probe beam is driven by the optical delay stage to the detector, (e.g. PCA [18] or Electro-Optic (EO) crystal [38]), and it is used to sample the THz pulses coming from the reflectors chain. The PCA as a receiver works in similarly to the emitter, the probe beam is used to excite the detector and the electric field, which accelerates the free carriers on the gap, is induced by the coupling of the THz electric field incoming from the emitter with the antenna structure. The current generated in the PCA detector, related to the THz field at the instant of the sampling, is acquired by means of a lock-in procedure. The detection by means of an EO crystal exploits the non linearity of the crystal, in relation to an incoming THz electric field. The linear polarized probe beam passes through the EO crystal, the non linearity of the crystal under effect of the THz electric field, changes the orientation of the polarization of the probe beam, according to the intensity of the THz field at the instant of the sampling. Using a quarter-wavelength plate and a Wollaston prism, the probe beam incoming from the EO crystal is split in two orthogonal linear polarized beams. The current generated by a balanced pair of photodiodes, proportional to the difference of the polarizations of the two laser beams, is acquired by a lock-in procedure. Varying the optical delay of the probe beam at different instant of sampling, the entire THz pulse is acquired.

In order to perform the spectroscopic analysis of a specimen, the transmitted THz

pulse is measured after the transmission through the QO system with (sample signal) and without (reference signal) the specimen to analyze. The signals are characterized by their relevant spectra, by means of their Fourier Transform (FT), and the spectra are used to extract the complex index of refraction of the sample.

The bandwidth and the dynamic range of the TDS systems are limited by the noise floor of the system, since the measurements are not meaningful when the spectral components of the reference signal reach the noise floor. A better understanding of the coupling between the photoconductor generator and the detector through the entire QO channel involved would be beneficial for the design of these systems. Indeed, this would allow to design more efficient sources and QO channels, allowing to increase the dynamic range and the bandwidth of the system.

1.1.2 THz Imaging System

Presently, a large variety of practical applications are discussed for THz systems. They range from security (e.g. body scanners) through the monitoring of industrial production processes [2, 7–10, 12–15, 39]. Many of those applications involve THz imaging. A general scheme of a THz imaging system does not differ substantially from the THz TDS system scheme illustrated in the previous section, but they have to be able to scan the item (e.g. body, luggages, industrial products, etc.) that has to be inspected. One of the advantages to use THz imaging system is that it can provide higher spatial resolution than the MMW system, because of the wide band signal involved, allowing to detect different layers of the item under inspection. Another advantage of the THz imaging system is the possibility to localize concealed items or to perform non destructive inspection, thanks to the lower absorption of the radiation at THz frequencies than the optical frequencies. Moreover, resorting to the capability to perform spectroscopic analysis, as described in the previous section, combined with the above mentioned properties, a THz imaging system can be able also to detect different substances or material during the scanning. As drawback, the scanning takes typically several minutes or longer using the actual technology [39–42]. Such scanning time is acceptable in scientific applications, and they may be tolerable if more information is required from the inspection of items, as supplement to other faster scanning technology (e.g. X-ray scanners). The long scanning time is directly connected to the low power level detected by the receiver. Indeed, to recover the entire signal completely and uniquely, long integration times are needed in order to extract the signal from the noise.Therefore, the generation of large field of view images with the actual technologies takes from several minutes to some hours [39–42].

In order to increase the performances of the system and to reduce the scanning time, a clear characterization of the dispersion of the QO channel (source-to-detector) is needed. Having a clear picture of the coupling between the source and the detector would allow to design more efficient QO channel, increasing the detected power by the receiver. As result, the integration time to detect the signals would decrease, speeding up dramatically the acquisition time of the image.

1.2 Photoconductive Antennas: State of the Art

The main components of a typical photoconductive antenna include a metallization layer, where the antenna geometry is patterned, a photoconductive substrate and a dielectric (e.g. HRFZ-Si) lens. A general scheme is depicted in Fig. 1.2(a).

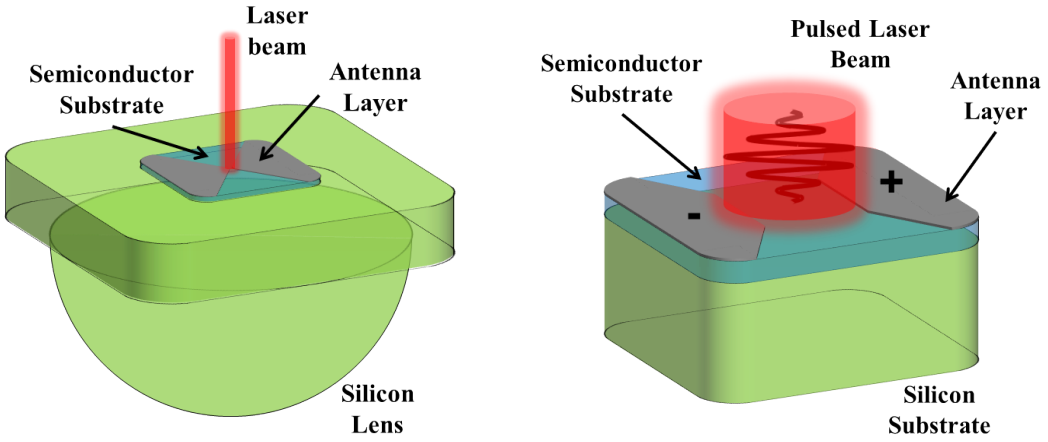

(a) (b)

Figure 1.2: Photoconductive antenna structure: a) General structure of a photoconductive antenna, b) Feeding gap of a photoconductive antenna.

Considering the gap structure of a PCA depicted in Fig. 1.2(b), the two metallizations of the antenna are biased by a voltage, providing a bias field to the photoconductive gap. The gap is also excited by pulsed laser beam, Pulsed Wave (PW) mode, which changes the conductivity of the material in the gap, because of the excitation of the electrons from the valence band to the conduction band. The electric field, induced by the bias voltage (transmission) or by an incoming electromagnetic field (reception), accelerates the free carriers in the conduction band, generating a time-varying current through the photoconductive gap. The spectrum of the current, generated in transmission, is frequency dependent, according to the features of the photoconductor. The antenna fed by such current radiates an electromagnetic field. The spectrum of such electromagnetic field depends on the spectrum of the current, the coupling between the photoconductive generator and the antenna, the radiation properties of the antenna structure, and its coupling with the dielectric lens.

The next two subsections present an overview of the state of the art about the technology commonly used for PCAs and their limitations will be pointed out.

1.2.1 Photoconductive Lens Antennas

Because of the intrinsic broadband spectrum of the current generated in the photoconductor gap, the dispersion and the radiation efficiency of the antennas has a big impact on the spectrum of the radiated field. Most of the antenna structures used nowadays, in

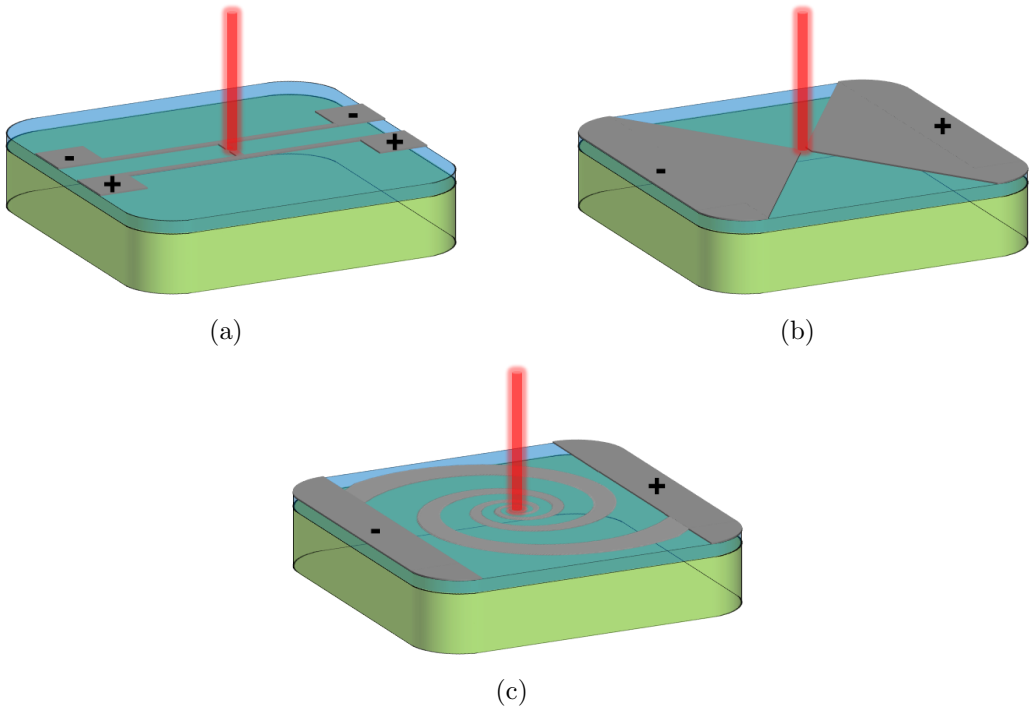

Figure 1.3: Antenna geometries for photoconductive antennas: a) Auston-switch antenna, b) bow-tie antenna, c) logarithmic spiral antenna.

commercial technologies [39–42], use different dipole antenna structures, proposed in the early age of the THz PCA technology [20, 43, 44].

The geometry of a photoconductive dipole antenna, sometimes called as Auston-switches named as its first proposer, is shown in Fig. 1.3(a). The dipole is well know to be intrinsically a narrow band antenna, making such solution not suitable to radiated efficiently energy distributed over a large bandwidth. In the last two decades, many works have aimed to improve the radiation efficiencies of the PCAs, resorting to established microwave engineering concepts as self-complementary structures, log-periodic antenna [45–47], spiral antenna [48–52], an bow-tie antenna [53]. The typical geometry of a bow-tie and logarithmic spiral antenna are shown in Fig. 1.3(b)-1.3(c). However, even such structures coupled with a dense dielectric lens suffer of high dispersion and poor radiation efficiency as it has shown for the Auston-switch and bow-tie antennas in [54], and for spiral antennas in Chapter 5 of this thesis, since the antennas are required to operate over a frequency bandwidth that exceed an octave. A detailed analysis of the dispersion and coupling through the QO channel of such photoconductive antennas is presented in Chapter 3.

1.2.2 Large Area Photoconductive Emitters

As a consequence of the dispersivity and the radiation efficiency, which affect existing PCAs performances, these devices suffer of low power emitted. Typical values of radiated

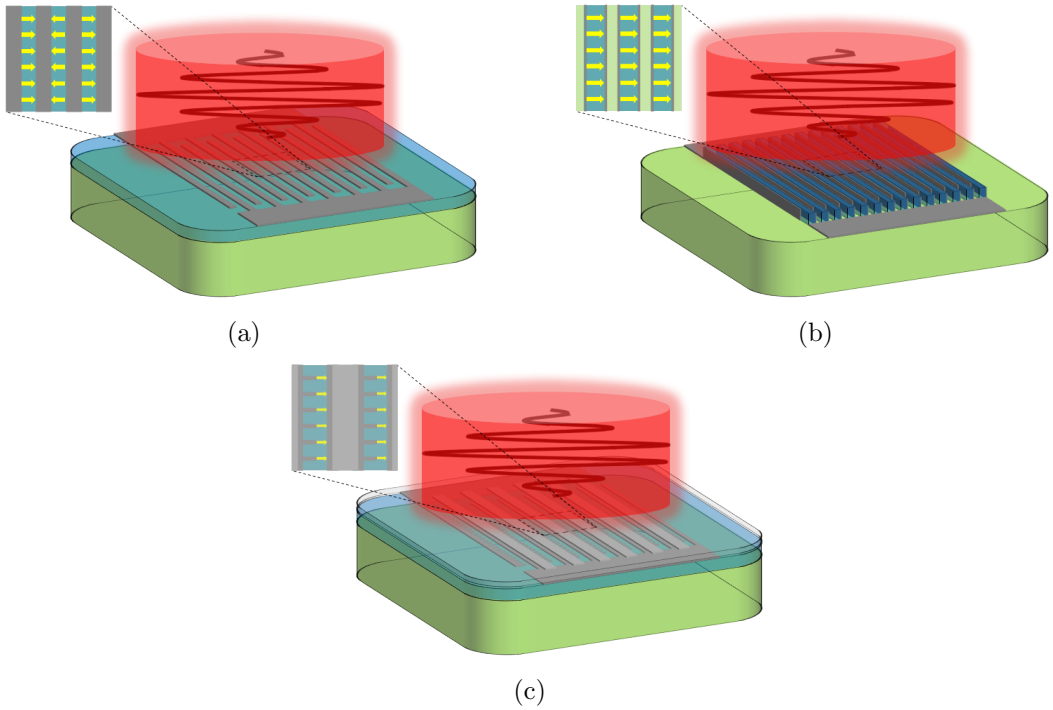

Figure 1.4: Large area emitters: a) interdigitated electrodes emitter presented in [62], b) etched interdigitatded electrodes presented in [70], c) plasmonic emitters presented in [74]. The yellow lines represent the excited dipoles in the photoconductor material.

power do not exceed few tens of μW [42], when they operate in the PW mode. Increasing the laser power and applied bias voltage do not provide a suitable solution due to the thermal breakdown of the device and the saturation of the photocurrent [55–59], which occur at high laser power illumination. To overcome such limits different solutions have been proposed as large area aperture emitters [55, 56, 60, 61], large area interdigitated electrodes emitters [62–74]. Some of these structures are shown in Fig. 1.4.

Despite the aim to increase the radiated power of the THz radiation avoiding the saturation effects and thermal breakdown, all these solutions are also not very efficient. The large area emitters are not efficient to generate high radiated power because the spreading of the laser power over a wider area of photoconductor material makes difficult the generation of strong currents on the photoconductive gap to achieve efficient radiation. Despite different technological solutions have been implemented for interdigitated electrodes emitters, these structures are not suitable to radiated energy over a large bandwidth, because they are basically array configurations of small dipoles, having an intrinsic resonant behavior.

A more detailed discussion about the problems of the state of the art of large area emitters is provided in Chapter 6.

1.2.3 Equivalent Circuits in the Literature

In recent years different equivalent circuits for photoconductive source have been presented aiming to describe the coupling between the photoconductor generator and the antenna both for the CW [2,75,76], and PW [77,78] laser operating mode. This section will discuss only the equivalent circuits developed for PW mode, which are shown in Fig. 1.5.

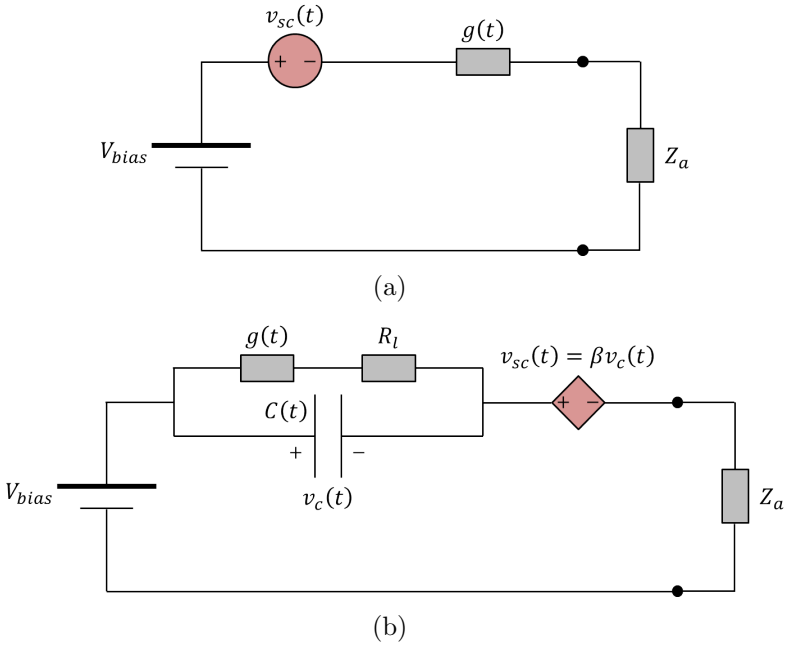

Figure 1.5: Equivalent circuits for PCAs in PW mode presented in literature: a) circuit proposed in [77], and b) circuit proposed in [78].

Such equivalent circuits are derived starting from the classical electrodynamic model, which describes the generation of free carriers in the semiconductor material when it is optically pumped. Knowing the time-varying free carriers density in the semiconductor gap of the antenna under optical illuminations allows to derived the time-varying conductance of the gap, and the time-varying current flowing through the gap when a bias voltage is applied.

More in details, both equivalent circuits, shown in Fig. 1.5, represent the photoconductor gap by a time-varying conductance $g(t)$, and the antenna by an impedance Z_a, assumed to be real and frequency-independent over the operative bandwidth. The substantial difference is the modeling of the space-charge screening effect in the gap. In the circuit shown in 1.5(a), this effect is modeled as a time-varying voltage generator $v_{sc}(t)$. Whereas the circuit depicted in 1.5(b), the space-charge screening is considered introducing a dependent voltage generator $v_{sc}(t)$, controlled by the voltage $v_c(t)$ across a time-varying capacitor $C(t)$, which takes into account for the accumulation of the carriers near the gap electrodes. Moreover, the circuit takes into account of the electrode losses by a resistance R_l. In both circuits, the equivalent circuit elements are connected in series to a bias voltage

generator V_{bias}.

Despite the fact that these equivalent circuits are useful to have a qualitative physical insight about the generation of the transient current across the semiconductor gap when it is optically pumped, they are not suitable for the analysis and the design of the antenna features at each frequency over the operative THz bandwidth. Firstly, these equivalent circuits are time domain representations of the photoconductive source, which does not allow to represent the antenna load as complex impedance at each frequency. In fact, in both circuits the antenna is represented as a frequency independent real impedance, which render inaccurate the analysis of the coupling between the antenna and the photocoductive source, and moreover it does not allow the analysis of the dispersion introduced by the antenna structure on the radiated spectrum of the pulse. Secondly, these circuits are hybrid equivalent circuits due to the simultaneous presence of biasing and THz circuit components operating at different frequency regime. These circuits are not able to represent the THz energy generation over the operative bandwidth. A Thévenin/Norton equivalent circuit [79], which takes into account for the laser, electrical and geometrical parameters of the photoconductive generator, needs to be developed to efficiently design photoconductive antennas.

The lack of such equivalent circuit for photoconductive antennas has been the motivation to develop a Norton equivalent circuit for photoconductive sources in this research work, in order to provide a tool which allows to the engineers to design more efficient photoconductive antennas, resorting to vast heritage of wide band microwave engineering. The detailed derivation of the Norton equivalent circuit is discussed in Chapter 2.

1.3 Novel Contribution of This Thesis

Starting by the theoretical formulation of the photogeneration of free carriers in photoconductor material, an engineering tool for analyzing and designing photoconductive antennas has been developed, and it is presented in this thesis. Thanks to the development of this tool, and to the adoption of an accurate electromagnetic model of the QO channel used for characterization of PCA, an in depth analysis of the performances of photoconductive antennas is presented. Moreover, the better understanding of the coupling between the photoconductor generator and the antenna, provided by the proposed equivalent circuit, has led to propose a design solution of a novel photoconductive array source, able to radiate power efficiently over a wide operative bandwidth. Last but not least, a study of the performances of logarithmic spiral lens antenna is discussed, addressing the dispersion problem which affected such antennas and proposing a solution to enhance the radiation performances limiting the dispersion over a wide bandwidth.

The novel aspects that have been proposed in this research work can be summarized as follow:

- A Norton equivalent circuit for the photoconductive source localized in the gap of PCAs. This circuit representation of the source constitutes a powerful design tool, as it allows to maximize the output power as function of the geometry of the gap,

the properties of the semiconductor, and the features of the laser pump. Moreover, it provides a clear description of the coupling between the photoconductor generator and the antenna over the operative bandwidth.

- For the first time, the energy spectrum and the average power radiated by the PCAs can be estimated, thanks to the use of the Norton equivalent circuit for the photoconductor generator.

- An electromagnetic model of the QO (source-to-detector) channel, which allows a complete characterization of the power budget from the source to the detector.

- An accurate analysis of the most common used PCA geometries in terms of dispersion, radiation efficiency, and coupling with the measurement system over the operative bandwidth. Such analysis provides a clear view about the dispersion of energy spectrum radiated by the PCAs through the measurement channel. The results are experimentally validated by power and spectrum measurements of PCA prototypes. The devices have been fabricated and the measurements campaign have been performed at the Institute of Microwave and Photonics of the School of Electronic and Electrical Engineering at University of Leeds, Leeds, United Kingdom, with whom a scientific collaboration has been established in the framework of this research project.

- An analysis of the radiation of spiral antennas as feed of dense dielectric lenses, and a solution to enhance the performances of lens spiral antennas over a wide band.

- The design of a photoconductive connected array coupled with an array of microlenses, aiming to increase dramatically the power radiated respect to the current state of the art. The use of such structure coupled to an array of microlenses, which focus a large laser beam on the periodically placed photoconductive gap, is able to provide high value of radiated power over the wide operative bandwidth, avoiding all the limitations of which have affected all the existing structures of the state of the art.

1.4 Outline of the Thesis

The topics of the thesis are the following: Chapter 2 presents a Norton equivalent circuit for analyzing and designing PCAs; Chapter 3 discusses the analysis of the most common used antenna lens geometries for PCA; and Chapter 4 shows the analysis of the QO channel typically used to measure and characterize the PCAs, and an experimental validation of the analysis is provided by power and spectra measurements; Chapter 6 presents a design of a new photoconductive emitter able to radiate more efficiently high level of power over a large bandwidth; finally Chapter 5 discusses the analysis of the radiation performances of logarithmic spiral antennas as feed of dense dielectric lenses, respectively.

More in detail, the thesis is organized as follow:

- **Chapter 2** presents the derivation of a Norton equivalent circuit for the photoconductor generator of PCAs. The equivalent circuit takes into account for the electrical properties of the photoconductor material, the features of the laser excitation, and the geometrical dimensions of the photoconductor gap. It allows to derive the energy spectra and the power radiated by PCAs. The circuit is a powerful tool, since it allows the analysis of the radiation performances of PCAs in terms of efficiency and dispersion over the operative bandwidth.

- **Chapter 3** presents an accurate electromagnetic analysis of most common used PCA geometries coupled to dense dielectric lens and the reflectors chain typically involved in THz TDS system. The analysis quantify the efficiency and the gain of the lens antennas under analysis, and the reflectors chain when it is used in combination with the analyzed PCAs.

- **Chapter 4** presents the analysis of the entire QO channel (source-to-detector). The equivalent circuit, proposed in Chapter 2, in combination with the electromagnetic model, presented in Chapter 3, allows to analyze the dispersion of the energy spectrum from the source to the detector, providing a meaningful insight about the entire QO channel. The analysis is validated by experimental measurements of the detected power and spectra of PCA prototypes.

- **Chapter 5** presents the analysis of the radiation of dense dielectric lenses fed by logarithmic spiral antennas. The analysis shows how to control the radiation patterns of the spiral by changing the geometrical parameters of the antenna, allowing to achieve high aperture efficiency over a large bandwidth when the spiral antenna is coupled with an elliptical lens. Moreover, it is shown that the directivity of the spiral antenna inside the dielctric can be increased by using an air gap between the dielectric lens and the antenna feed, allowing to achieve lens directive patterns without sidelobes and reducing the dispersivity of the radiated pulse.

- **Chapter 6** presents a design of a PCA in array configuration based on the concept of connected array coupled with an array of microlenses. The photoconductive connected array is designed in order to maximize the radiated power by the device. The simulated results of the spectrum and power radiated by such design are provided, showing clearly the enhancement of the radiated power of two orders of magnitude with respect to the state of the art, making it an effective solution to the lack of high power radiated by the current PCA devices.

- **Chapter 7** concludes with a review of the most significant results presented in this thesis and an outlook on possible future developments.

Chapter 2

Norton Equivalent Circuit for Pulsed Photoconductive Antennas

A novel equivalent circuit of photoconductive feeds is introduced for describing the coupling between such feeds and antennas. The proposed circuit effectively describes the mechanism of feeding the antenna by the semiconductor when this latter is illuminated by a laser operating in a pulsed mode. Starting from the classical continuity equation, which models the free carriers density with respect to the laser power pump and the semiconductor features, a Norton equivalent circuit in the frequency domain is derived, which takes into account the electrical properties of the semiconductor material, the features of the laser excitation, as well as the geometrical dimensions of the electrodes, which couples antenna to the semiconductor material. The proposed circuit allows an estimation of the energy spectrum and, consequently, the average power radiated by photoconductive antennas. Therefore, the proposed model provides an effective tool for analyzing and designing photoconductive antennas.

2.1 Introduction

In recent years, Terahertz (THz) technology has attracted the interest of researchers for its variety of applications [1–11, 31, 80–82]. The emergence of all these applications has been driven by the availability of photoconductive antennas (PCAs), which have made available bandwidth in the THz spectrum at relatively low cost [1, 2, 4, 31], [18, 37, 57, 76–78, 83–86].

In photoconductive antennas the basic mechanism for the THz power generation and detection relies on semiconductor materials pumped by laser. Specifically, when a laser source impinges on a semiconductor with an appropriate carrier frequency, it provides the required energy for the electrons to move from the valence band to the conduction band, and free electrons-holes pairs are generated. The presence of free carrier pairs produces a change of the conductivity of the material, which becomes a photoconductor. The laser pump source typically operates in two different modes; i.e., Continuous Wave (CW) mode [2], [76] or Pulsed Wave (PW) mode [2], [18], [83]. The conductivity of the semicon-

ductor material changes periodically in time according to the laser operating mode and the lifetime of the carriers in the semiconductor. Applying a biasing voltage (in transmission), inducing an electric field across the semiconductor gap, or impinging with THz radiation (in detection), these free charges are accelerated. A time varying current is induced across the photoconductive gap, because of the acceleration of the free carriers. This effect is clearly localized on the gap, however it induces a global propagation of electromagnetic fields in the surrounding of the antenna structure. The propagating signal has frequency components that depend on the modulating signal of the laser pump and the semiconductor response to the laser excitation, as well as the geometrical features of the structures connected to the electrodes. Some frequencies will be more or less excited depending on the frequency response characterizing the surrounding structures.

The maximum available power of a single PCA in transmission is limited by the number of charges that can be excited to the conduction band of the semiconductor, by their mean velocity, by the coupling of the current in the gap with the surrounding antenna structure, and by the thermal failure of the device [84], [76]. The thermal failure is associated with an increase of temperature in the photoconductive material. The main causes of Joule heating are the direct laser power absorption from the material and the THz photocurrents induced due to the biasing voltage through the gap. In order to take into account all these aspects, in recent years different hybrid equivalent circuits have been developed for both the CW [2], [76], [86] and the PW operating mode [77], [78]. Specifically for the PW operating mode, none of them however constitutes a frequency domain equivalent Thévenin or Norton circuit [79] representative of the THz radiation, because of the simultaneous presence of biasing and THz components in such circuits. Such models provide a useful qualitative physical insight of the radiation mechanism, but they are not suitable for the analysis and design of antenna features at each THz frequency. Moreover, Thévenin or Norton circuits are crucial for describing the coupling between the photoconductive generator and the antenna. Without an equivalent Thévenin or Norton circuit which takes into account all of the laser, electrical, and geometrical parameters of the photoconductive generator, it is not feasible to efficiently design photoconductive sources. In this work we propose a simple and effective Norton equivalent model for PW operating mode, which takes into account all these aspects and is therefore useful for describing the coupling between the photoconductive feed and the radiating antenna. A validation of the proposed equivalent circuit via power and spectrum measurements of some PCA prototypes will be shown in Chapter 4.

The chapter is structured as follows: Section 2.2 briefly summarizes the model used for describing the electrical properties of the photoconductive material; Section 2.3 is devoted to the description of the equivalent Norton circuit derivation; Section 2.4 discusses the behaviour of the equivalent generator with respect to the various parameters involved in the model. Section 2.5 shows the use of the proposed equivalent circuit to estimate the energy spectrum and the relevant average power radiated by the photoconductive antenna along with some numerical results for three different antenna structures. Section 2.6 contains some concluding remarks.

2.2 Photoconductivity Model

Referring to Fig. 2.1, let us consider the problem under analysis composed by a small volume, with dimensions (W_x, W_y, W_z), of photoconductive material (e.g., Low-Temperature-Grown Gallium Arsenide, LTG–GaAs) in the origin of the reference system. Its conductive properties are tuned by means of a laser excitation $\mathbf{s}_{laser}(\mathbf{r};t)$, where $\mathbf{s}$ represents the time-varying Poynting vector associated with the laser beam.

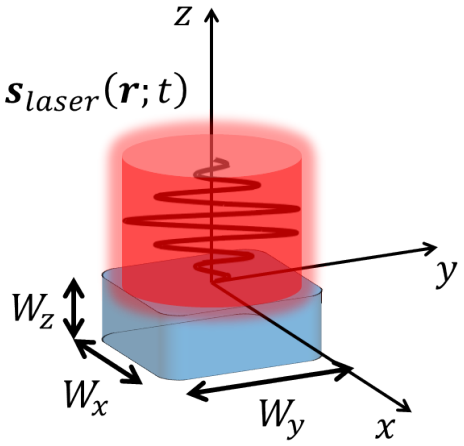

Figure 2.1: Photoconductor volume (in dark blue) illuminated by a pulsed laser beam (in red).

The conductivity σ of the semiconductor can be expressed in terms of the charge carrier density n per unit of volume and the relevant carrier mobility μ through the equation:

$$\sigma(\mathbf{r};t) = e\,\mu\,n(\mathbf{r};t) \tag{2.1}$$

where e is the elementary charge. The conductivity is related to both electron and hole carriers. However, in photoconductive materials, since transient mobility of the holes is less than that of the electrons, the last mainly contribute to the conductivity [56]. The time and spatial dependence within the semiconductor are due to the laser pump which induces an increase of density of the free carriers. This phenomenon has been investigated in the literature for both CW laser operating mode [2,76], and PW laser operating mode [2,18,83]. The main formulas used in the proposed model are reported in Appendix A. As result, the conductivity of the photoconductor volume can be expressed as:

$$\sigma(\mathbf{r};t) = e\,\mu\,\frac{1}{2\pi}\int_{-\infty}^{+\infty} N(\mathbf{r};\omega)\,e^{j\omega t}\,\mathrm{d}t \tag{2.2}$$

where $N(\mathbf{r};\omega)$ is the spectrum of the carrier density distribution $n(\mathbf{r};t)$ obtained by means of the temporal Fourier Transform (FT) $N(\mathbf{r};\omega) = FT[n(\mathbf{r};t)]$. Such a spectrum is expressed in terms of the semiconductor and laser source parameters as shown in Appendix A:

$$N(\mathbf{r};\omega) = \left(1-|\Gamma|^2\right)\frac{1-e^{-\alpha W_z}}{W_z}H(\omega)\,|\tilde{\mathbf{s}}_n(\boldsymbol{\rho}, z=0)|\,\tilde{S}(\omega) \tag{2.3}$$

with $-W_z \leq z \leq 0$, and where the volumetric carrier densities have been averaged and uniformly distributed along z. In (2.3), assuming that the laser beam illuminates the photoconductor orthogonally, $|\tilde{\mathbf{s}}_n(\boldsymbol{\rho}, z=0)|\,\tilde{S}(\omega)$ is the spectrum of the time-varying envelope of the Poynting vector distribution of the laser source evaluated at the interface between the air and the semiconductor, and it only depends on the z-transverse vector $\boldsymbol{\rho}$. The term $H(\omega) = \tau/[hf_g(1+j\tau\omega)]$ is the frequency response of the semiconductor material to the laser excitation, where h is the Planck constant; f_g is the frequency associated with the energy band-gap $E_g = hf_g$, which separates the valence band from the conduction band in the crystal lattice of the photoconductor; α is the laser power absorption coefficient of the material; Γ is the Fresnel reflection coefficient at the air-semiconductor interface; and τ is the lifetime of the free carriers in the photoconductor. In order to induce the electron band-to-band transitions in the photoconductor, the frequency of the carrier f_{laser} of the pulsed laser in the PW mode (or the two laser carrier frequencies in the CW mode) has to be greater than the band-gap frequency, i.e., $f_{laser} > f_g$.

The corresponding conductivity change lasts as long as the laser pumping continues (CW mode), or in the case of very short bursts of laser power (PW mode), the conductivity change continues until all electron-hole pairs have recombined and the initial balance is restored.

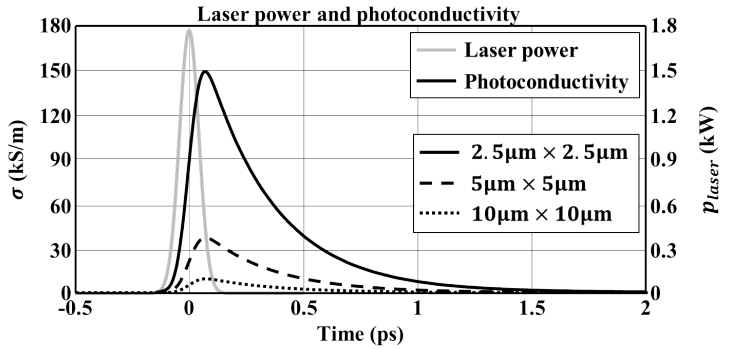

Figure 2.2: Simulated time-dependency of the bulk conductivity of a photoconductor material illuminated by a laser operating in PW mode when the laser pump (light grey line) is focused on different gap sizes and no voltage bias is applied. The curves (black lines) refer to the bulk conductivity when the laser beam, with average power $P_{ave} = 30\,\text{mW}$, is focused with a $-3\,\text{dB}$ power density distribution on the gap areas: the dotted line refers to a gap area of $10\,\mu\text{m} \times 10\,\mu\text{m}$, the dashed line refers to a gap area of $5\mu\text{m} \times 5\,\mu\text{m}$, whereas the solid line refers to a gap area of $2.5\,\mu\text{m} \times 2.5\,\mu\text{m}$.

As an example, in Fig. 2.2 the time-dependent behaviour of the average bulk conductivity in the photo-excited volume of a photoconductor is shown when it is illuminated by a single pulse of a laser operating in PW mode. The results refer to a Gaussian laser beam profile with diameter at $-3\,\text{dB}$ D_{laser} equal to the size of the volume-illuminated-surface $D_{laser} = W_x = W_y$, operating at a frequency $f_{laser} = 375\,\text{THz}$ (800 nm), with a repetition rate of $f_p = 80\,\text{MHz}$, a pulse width of $\tau_p = 100\,\text{fs}$, and a laser average power $P_{ave} = 30\,\text{mW}$. In particular, we considered a photoconductor volume of thickness $W_z = 2\,\mu\text{m}$; an absorption coefficient $\alpha = 10^6\,\text{m}^{-1}$; a carrier lifetime $\tau = 0.3\,\text{ps}$; carrier

mobility $\mu = 300\,\mathrm{cm}^2/\mathrm{Vs}$, [56,87,88]. It is worth noting that the mobility of the LTG-GaAs is strongly dependent by the manufacturing process, in particular by the annealing process [23,89]. Without such process the material provides very low value of dark resistance, when a bias voltage is applied. This results in high working temperature of the material, which involves a substantial decreasing of the transient carriers mobility [19,21,89–91].

It is evident from Fig. 2.2 that the conductivity of the photoconductor can be increased focusing the laser power onto smaller area.

2.3 Equivalent Norton Circuit Model for Photoconductive Sources

A photoconductive antenna is an optoelectronic device which is used to emit and receive electromagnetic power in the THz frequency bandwidth. It is typically obtained by placing thin metallizations on a slab of photoconducting material which is illuminated by a laser beam $\mathbf{s}_{laser}(\mathbf{r};t)$, as it is shown in Fig. 2.3.

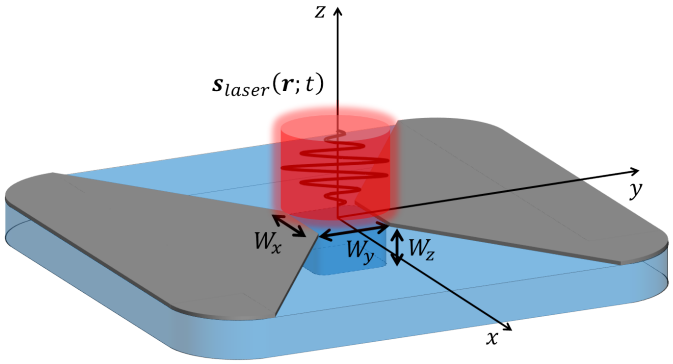

Figure 2.3: Photoconductive antenna gap representation.

The performances of such device are affected by various phenomena, i.e., the interaction between the laser source and the semiconductor, the geometrical parameters of the active gap which feeds the antenna, and the electromagnetic radiative properties of the entire structure. In order to take into account all these aspects, different equivalent circuit models have been proposed in [2,76–78,86] by using different approximations. However, until now, there is no theoretical model in terms of an equivalent Thévenin or Norton circuit [79], which is applicable for both CW and PW modes and that takes into account the frequency behaviour of both the current distributions in the excited photoconductive area and the coupling to the antenna at the same time. Thévenin and Norton equivalent circuits are the classical tools used in electronic engineering for quantifying and maximizing the power radiated by an antenna [79]. The absence of such model makes the investigation of the impedance matching between the photoconductive source and the antenna very difficult.

In this work we propose a novel Norton equivalent circuit for modelling the PCA feeding mechanism. In the model we assume that the photoconductive gap dimensions of the antenna, Fig. 2.3, are small in terms of the wavelength (the wavelength relevant to the highest frequency of the pulse bandwidth in PW mode or the wavelength of the beat frequency in the CW mode). In the model we also assume that the laser spot dimension is comparable or bigger than the gap size, in order to get a reasonable uniform illumination of the gap. Saturation effects due to high level of laser fluence on the gap are not considered [56]. Moreover, the screening effects due to the space-charge screening [77], and due to radiation field screening [56] are also neglected.

2.3.1 Time-Domain Circuit Representation

A schematic representation of a generic PCA is depicted in Fig. 2.4(a). The antenna is connected to a biasing voltage and its input terminals to the photoconductive material. The photoconductor in the gap between the terminals is excited by a modulating laser with a field distribution, $\mathbf{s}_{laser}(\mathbf{r};t)$. This schematic representation can be depicted circuitally, Fig. 2.4(b), with concentrated quantities rather than the distributed quantities introduced in (2.1).

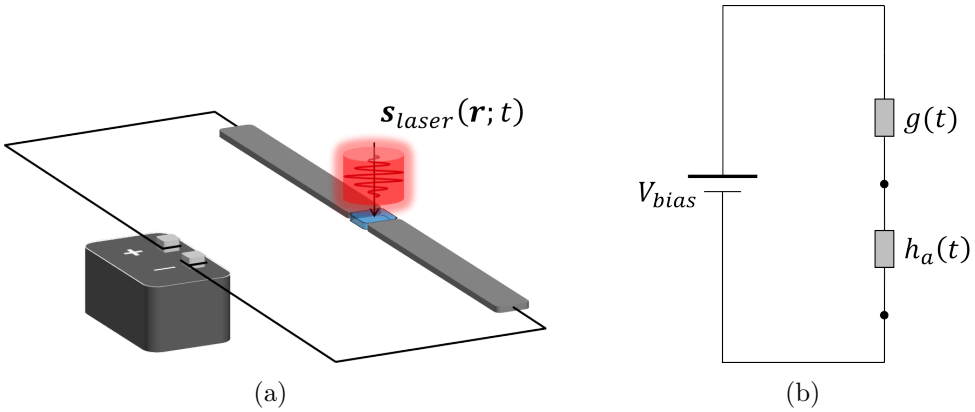

Figure 2.4: a) Photoconductive antenna schematic representation. b) Photoconductive antenna time domain circuit representation.

Specifically, the circuit is composed by three components, the first one is the bias voltage V_{bias}. The second one is a time-varying conductance $g(t)$, which represents the electrical properties of the gap. The third one is an impulsive response $h_a(t)$, which represents the antenna in time-domain.

The time-varying conductance $g(t)$ is derived applying the Ohm's law to the photoconductor gap, starting from the general constitutive relation of the photoconductor medium:

$$\mathbf{j}(\mathbf{r};t) = g_\sigma(\mathbf{r};t) \otimes \mathbf{e}(\mathbf{r};t) = \int_{-\infty}^{t} g_\sigma(\mathbf{r};t-\tau)\,\mathbf{e}(\mathbf{r};\tau)\,\mathrm{d}\tau \tag{2.4}$$

where $\mathbf{j}(\mathbf{r};t)$ is the current density flowing through the photoconductor gap, $g_\sigma(\mathbf{r};t)$ is the current impulsive response of the photoconductor material to an applied electric field,

and $\mathbf{e}(\mathbf{r};t)$ is the total electric field on the semiconductor gap. Here, the only significant current is oriented along $\hat{\boldsymbol{y}}$ with reference to Fig. 2.3. The current impulse response to an applied electric field $g_\sigma(\mathbf{r};t)$ of the photoconductor is assumed to be instantaneous [92], so in (2.4) it can be assumed that $g_\sigma(\mathbf{r};t-\tau) = \sigma(\mathbf{r};\tau)\,\delta(t-\tau)$, where $\sigma(\mathbf{r};t)$ is the photoconductivity defined by (2.1) and (2.3). Therefore, (2.4) can be rewritten as:

$$\mathbf{j}(\mathbf{r};t) = \sigma(\mathbf{r};t)\,\mathbf{e}(\mathbf{r};t) \tag{2.5}$$

From (2.5) the current flowing across each transverse section of the photoconductor can be calculated by

$$i(y;t) = \int_{-\frac{W_x}{2}}^{\frac{W_x}{2}} \int_{-W_z}^{0} \mathbf{j}(\mathbf{r};t)\cdot\hat{\boldsymbol{y}}\,\mathrm{d}z\,\mathrm{d}x \tag{2.6}$$

The current flowing through the gap can be evaluated as the current spatially averaged over the gap:

$$i(t) = \frac{1}{W_y}\int_{-\frac{W_y}{2}}^{\frac{W_y}{2}} i(y;t)\,\mathrm{d}y \tag{2.7}$$

and the voltage drop as

$$v(t) = -\int_{-\frac{W_y}{2}}^{\frac{W_y}{2}} \mathbf{e}(\mathbf{r};t)\cdot\hat{\boldsymbol{y}}\,\mathrm{d}y \approx e_y(0;t)\,W_y \tag{2.8}$$

Therefore, the current flowing across the gap can be approximated as

$$i(t) \approx g(t)\,v(t) \tag{2.9}$$

where $g(t)$ is the time dependent conductance of the photoconductor gap:

$$g(t) = \frac{1}{W_y^2}\int_{-\frac{W_y}{2}}^{\frac{W_y}{2}}\int_{-\frac{W_x}{2}}^{\frac{W_x}{2}}\int_{-\frac{W_z}{2}}^{0} \sigma(\mathbf{r};t)\,\mathrm{d}z\,\mathrm{d}x\,\mathrm{d}y \tag{2.10}$$

As shown in Appendix B, the time-varying conductance can be rewritten as the product of two terms:

$$g(t) = \eta(W_x, W_y, W_z, A_{laser})\,\tilde{g}(t) \tag{2.11}$$

The first term η quantifies the laser power absorption efficiency of the photoconductor gap, and it takes into account the spillover of the laser beam with respect to the photoconductor gap, the reflection at the interface air-photoconductor, and the laser power absorption property of the photoconductor:

$$\begin{aligned}\eta(W_x, W_y, W_z, A_{laser}) = \left(1-|\Gamma|^2\right)\frac{1-e^{-\alpha W_z}}{W_z}\cdot \\ \cdot\frac{1}{A_{laser}}\int_{-\frac{W_y}{2}}^{\frac{W_y}{2}}\int_{-\frac{W_x}{2}}^{\frac{W_x}{2}}\int_{-\frac{W_z}{2}}^{0}\left|\tilde{\mathbf{s}}_n(\boldsymbol{\rho};z=0)\right|\mathrm{d}z\,\mathrm{d}x\,\mathrm{d}y\end{aligned} \tag{2.12}$$

where $A_{laser} = \int_{-\infty}^{+\infty}\int_{-\infty}^{+\infty} \tilde{\mathbf{s}}_n(\boldsymbol{\rho}, z=0)\cdot\hat{\mathbf{z}}\,\mathrm{d}x\,\mathrm{d}y$ is the area of the spatial distribution with unitary amplitude of the laser beam Poynting vector at the photoconductor interface (Appendix C). The second term $\tilde{g}$ contains the time-varying behavior of the conductance g:

$$\tilde{g}(t) = \frac{A_{laser}}{W_y^2} e\,\mu\,h(t) \otimes \tilde{s}(t) \tag{2.13}$$

where $h(t) = IFT[H(\omega)]$ defines the impulsive response of the photoconductor material, and $\tilde{s}(t)$ is the time-varying envelope of the laser pulse.

As mentioned before the antenna is represented with its time-domain impulsive response $h_a(t)$, which is depicted in series, since its current is the same current as that which flows through the gap. In a time-domain analysis, the evaluation of the field radiated by the antenna typically involves a time convolution integral, which depends on the geometry and the antenna radiation mechanism. However, this time-domain approach is not suitable for analyzing the spectral behavior of the antenna. To avoid such problem, antennas are typically studied in frequency-domain and are circuitally characterized by means of an impedance $Z_a(\omega)$.

2.3.2 Derivation of the Norton Circuit Model

In order to study the coupling between the photoconductor gap and the antenna, it is useful to use an equivalent Norton circuit. Norton's theorem states that, in the frequency domain the current flowing in a load at the terminals of a complex linear electrical system can be obtained by replacing the entire system with only two equivalent components: an equivalent current generator and an equivalent impedance. Fig. 2.5(a) presents such an equivalent circuit, when the load is assumed to be the antenna under analysis. The Norton equivalent frequency domain current generator requires the evaluation of the spectrum of the current generator $I_g(\omega)$ flowing at the terminals of the antenna, when the antenna itself is short-circuited (Fig. 2.5(b)). Considering that the gap dimensions are small in terms of the wavelength and they are comparable with the laser spot size, the field contributions due to the electron and hole local separation mechanism and to the electrodes scattering do not significantly change the applied bias field intensity [77, 93], and the total electric field in the volume of the gap can be approximated with the applied bias electric field $\mathbf{e}(\mathbf{r};t) \approx -V_{bias}/W_y\hat{\mathbf{y}}$. Consequently, the short-circuit current flowing across the gap, according to (2.9), is defined as $i_g(t) \approx g(t)\,V_{bias}$ and its spectrum is obtained simply performing the FT of the time-domain current derived by the time-domain description, i.e.:

$$I_g(\omega) = FT[i_g(t)] \tag{2.14}$$

From (2.9) and (2.11):

$$I_g(\omega) = \eta(W_x, W_y, W_z, A_{laser})\,\frac{A_{laser}}{W_y^2} e\,\mu\,H(\omega)\,\tilde{S}(\omega)\,V_{bias} \tag{2.15}$$

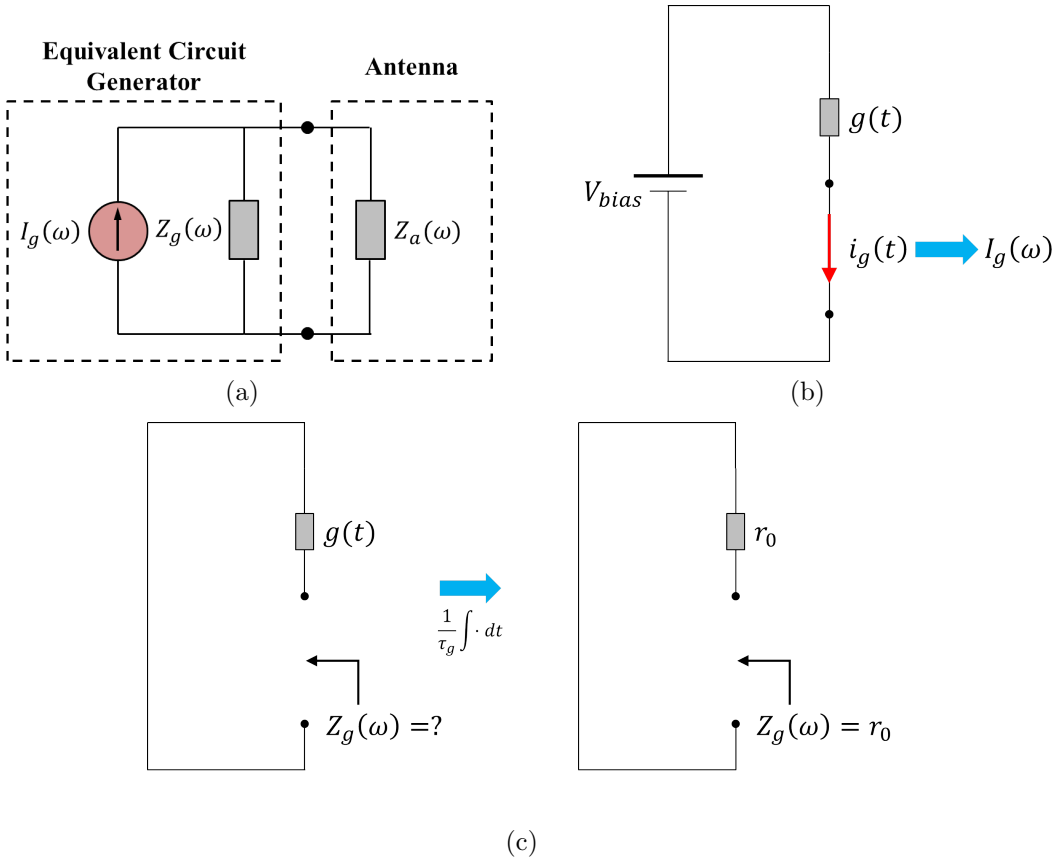

Figure 2.5: Equivalent Norton circuit schematic derivation.

Note that $i_g(t)$ well approximates the current flowing in the photoconductive gap in absence of the antenna, when the gap is small and illuminated with laser beams with diameter comparable or bigger than the gap size, as discussed in [93].

The equivalent Norton generator impedance is the impedance $Z_g(\omega)$ exhibited at the antenna terminals, in absence of the antenna (Fig. 2.5(c)) for each frequency, when the bias voltage generator is removed. From the circuit, it is evident that it represents the impedance at the terminals of the photoconductor gap. However, $Z_g(\omega)$ is not simply the FT of the time-varying resistance, but it is the ratio of voltage and current spectra at the terminals for each frequency:

$$Z_g(\omega) = \frac{V(\omega)}{I(\omega)} \tag{2.16}$$

Since one has no easy way to evaluate (2.16), due to the various physical phenomena involved in the photoconductor when it is illuminated by a laser beam [92], we introduce a zero-th order approximation considering to have a constant conductance $g(t)$, when the photoconductor is illuminated and that at each frequency the relation between the voltage and the current spectra in the photoconductor is instantaneous. In detail, the equivalent Norton impedance can be approximated as the inverse of the average conductance g_0 of the

time-varying conductance $g(t)$ (Fig. 2.5(c)) on the time interval τ_σ where the conductivity of the gap is different from zero:

$$Z_g(\omega) \approx r_0 = \frac{1}{g_0} = \frac{1}{\frac{1}{\tau_\sigma}\int_{\tau_\sigma} g(t)\,\mathrm{d}t} \tag{2.17}$$

By using (2.11) and the results in Appendix A, the average conductance is:

$$g_0 = \eta(W_x, W_y, W_z, A_{laser})\,\frac{A_{laser}}{W_y^2} e\,\mu\,\frac{1}{\tau_\sigma} H(\omega = 0)\,\tilde{S}(\omega = 0) \tag{2.18}$$

It is worth nothing that in (2.18), τ_σ is the time duration of the pulsed conductivity in the PW mode, defined as the time interval where the conductivity is above one hundredth of its peak value as it is shown in Fig. 2.6(a), or the period of the conductivity in the CW mode. For the PW mode τ_σ defines a reasonable time interval in which one can do an average of the time-varying conductance pulse. As it will be shown in the next section (Fig. 2.6(a)), the chosen value guarantees an interval sufficiently long for considering the entire pulse and, at the same time, not too long to consider a time-range where the conductance is ideally zero. This time interval constitutes the time-range in which the antenna is effectively excited and, consequently, for estimating the mean value of the equivalent generator impedance. Therefore, the mean resistance r_0 depends on the mean number of carriers which are in the conduction band of the photoconductor during the pulse duration in the PW operating mode, or during the period of the beat frequency in the CW operating mode.

2.4 Numerical Results

By using the same parameters for the photoconductor used in the example in Section 2.2, the values of the photoconductor time-varying resistance and the relevant mean values are reported in Fig. 2.6. When the photoconductor is not illuminated, the equivalent Norton resistance assumes extremely high values, which depend on the intrinsic free carrier concentration in the photoconductor. On the contrary, when the photoconductor is illuminated by the laser, it is theoretically possible to realize a matching between the equivalent Norton generator and the antenna. In order to reach this matching, it is necessary to focus the laser power on a small gap. The limitation comes from the thermal failure associated with high laser power concentration.

The generator resistance depends on many parameters as the mobility of the carriers, the geometry of the gap, the intensity of the laser, and the spot size of the laser, as it is shown in (2.18). The dependency of the generator resistance with respect to these parameters is shown in Fig. 2.7, where the fixed features of the laser and the photoconductor are the same listed in Section 2.2.

Fig. 2.7(a) shows that the generator resistance increases as the laser beam diameter increases compared to the area of the gap; i.e., focusing the laser power on a smaller area decreases the resistance of the photoconductor, as is expected by (2.18). By decreasing

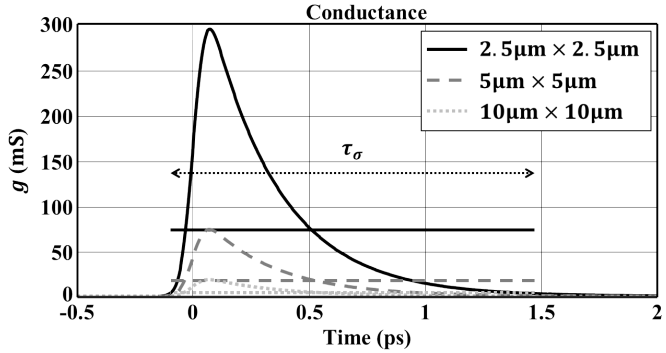

(a)

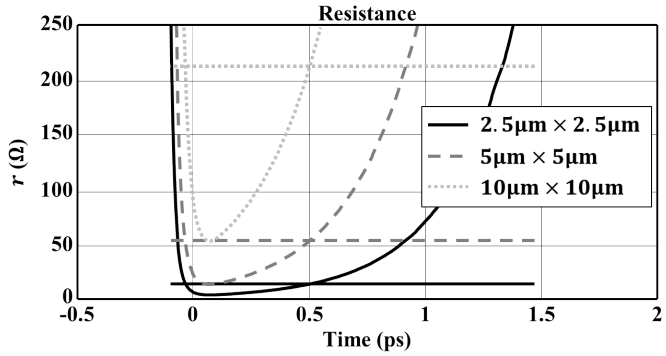

(b)

Figure 2.6: Time-dependency of the generator a) conductance and its related b) resistance of the photoconductor material illuminated by a laser operating in PW mode. The laser beam, with average power $P_{ave} = 30\,\mathrm{mW}$, is focused on different gap sizes. The light grey dotted line refers to the laser beam diameter at $-3\,\mathrm{dB}$ focused on a gap area of $10\,\mu\mathrm{m} \times 10\,\mu\mathrm{m}$, the dark grey dashed line refers to the laser beam diameter at $-3\,\mathrm{dB}$ focused on a $5\,\mu\mathrm{m} \times 5\,\mu\mathrm{m}$ area, whereas the black sold line refers to the laser beam diameter at $-3\,\mathrm{dB}$ focused on a $2.5\,\mu\mathrm{m} \times 2.5\,\mu\mathrm{m}$ area. The straight lines refer to the related mean values during the pulse duration τ_σ.

the size of the laser beam, more laser power is absorbed by the photoconductor material and the resistance value decreases up to where the laser beam illuminates homogeneously the entire photoconductor gap area. The range of validity of these results is the following: the laser beam has to be comparable or bigger than the gap area, since a laser beam size smaller than the area gap implies zones not illuminated by the laser with very high resistance values. In such cases a spatial distribution of the resistance has to be taken into account for the evaluation of the generator resistance. Finally, the behaviour of the generator resistance with respect to the transient free carriers mobility is shown in Fig. 2.7(b). The free carriers mobility is a feature of the semiconductor, that changes according on the manufacturing process of the material itself. In particular, for the LTG-GaAs the mobility of the free carriers is strongly affected by the temperature used in the growing process and by the annealing procedure [19, 21, 23, 88–91].

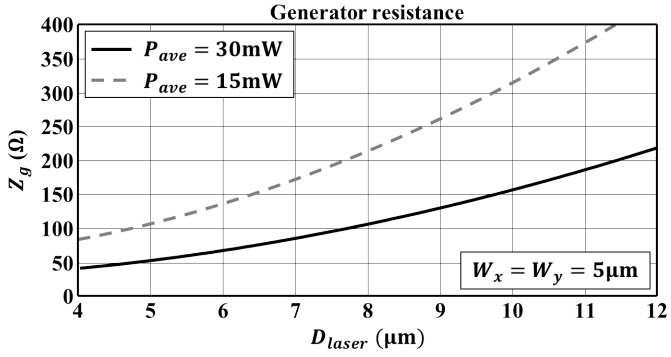

(a)

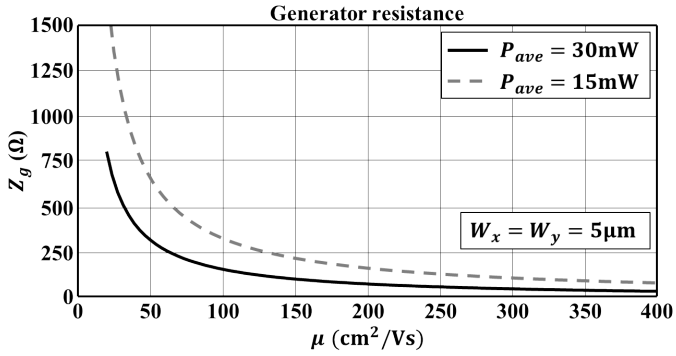

(b)

Figure 2.7: Parameters dependency of the generator resistance of a photoconductor material illuminated by a laser operating in PW mode: a) laser beam size dependency; and b) carriers mobility dependency. The fixed features of the laser and the photoconductor material are the same listed in Section 2.2.

2.5 Energy Spectrum and Average Power Radiated

The evaluation of the energy spectrum and the power radiated by the PCA is shown in this section, calculated from the equivalent circuit model proposed in Section 2.3.

By supposing a finite energy voltage signal $v(t)$ and its related current signal $i(t)$, it is possible to derive the instantaneous power $p(t)$, and consequently the energy of the signal as:

$$E = \int_{-\infty}^{+\infty} p(t)\,\mathrm{d}t = \int_{-\infty}^{+\infty} v(t)\,i(t)\,\mathrm{d}t \tag{2.19}$$

The energy can be evaluated also knowing the spectra of the voltage and current signal, resorting to the generalized Parseval's theorem:

$$E = \int_{-\infty}^{+\infty} v(t)\,i(t)\,\mathrm{d}t = \frac{1}{2\pi}\int_{-\infty}^{+\infty} V(\omega)\,I^*(\omega)\,\mathrm{d}\omega \tag{2.20}$$

where $V(\omega) = FT[v(t)]$ and $I(\omega) = FT[i(t)]$ are the spectra of the voltage and current signals, respectively. The current signal $i(t)$ is not conjugate in (2.20), because it is a real

signal. The product of the voltage spectrum $V(\omega)$ and the conjugate current spectrum $I(\omega)$ in (2.20) represents the energy spectrum associated with the voltage $v(t)$ and current $i(t)$ signals.

Referring to the Norton equivalent circuit in Fig. 2.5(a), by using formulas (2.15) and (2.17), one can calculate the spectrum of the current generator $I_g(\omega)$ and the generator impedance $Z_g(\omega)$ of the photoconductor, respectively. Given the antenna impedance $Z_a(\omega)$, which can be estimated by using analytical formulas or by numerical tools, the spectrum of the current $I_a(\omega)$, flowing in the antenna, can be easily evaluated. By knowing the spectrum of the current flowing into the antenna $I_a(\omega)$ and the antenna impedance $Z_a(\omega)$, it is possible to derive the energy spectrum associated with the antenna:

$$E_s(\omega) = V_a(\omega) I_a^*(\omega) = Z_a(\omega) \left| \frac{Z_g(\omega)}{Z_a(\omega) + Z_g(\omega)} \right|^2 |I_g(\omega)|^2 \tag{2.21}$$

The energy generated by the PCA can be evaluated by integrating (2.21), using relation (2.20):

$$E_{source} = \frac{1}{2\pi} \int_{-\infty}^{+\infty} E_s(\omega) \, \mathrm{d}\omega \tag{2.22}$$

The result of this integral is a real quantity, because of the Hermitian symmetry of the spectrum. Assuming that the antenna is lossless, it represents the energy of the pulse radiated by the antenna, since it is related to the real part of the antenna impedance. Since the PCA radiates pulses periodically with a period $T_p = 1/f_p$, where f_p is the repetition rate of the laser, the average power radiated by the antenna can be calculated as:

$$\bar{P}_{source} = \frac{E_{source}}{T_p} \tag{2.23}$$

The energy spectrum $E_s(\omega)$ associated with the antenna can be related to the energy spectrum $E_s^{max}(\omega)$ of the maximum available energy, when the antenna load is matched to the photoconductor equivalent generator impedance, as:

$$E_s(\omega) = \eta_m(\omega) E_s^{max}(\omega) \tag{2.24}$$

where the matching efficiency $\eta_m(\omega)$ is defined as the ratio between the power $P_{source}(\omega)$ radiated by the antenna and the power available $P_{available}(\omega)$ provided by the photoconductor gap to a matched load antenna, at each frequency i.e.,

$$\eta_m(\omega) = \frac{P_{source}(\omega)}{P_{available}(\omega)}. \tag{2.25}$$

As an example, we apply the above discussed analysis to three different antenna geometries, i.e., the Auston-switch, the bow-tie, and the spiral antenna (Fig. 2.8), which are the most common geometries for PCA found in the literature, [1, 2, 4, 31].

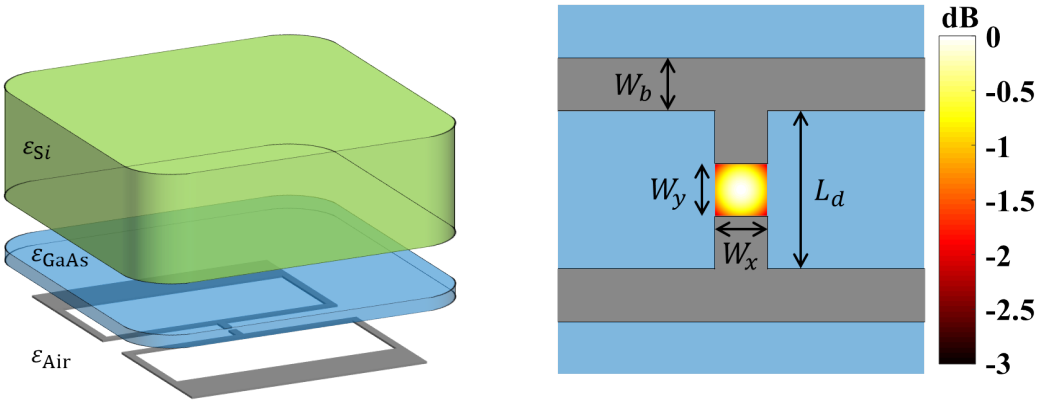

(a)

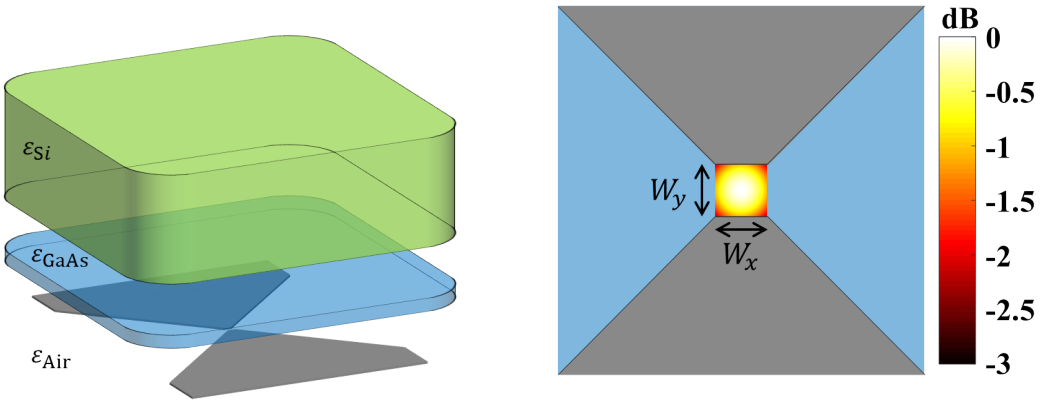

(b)

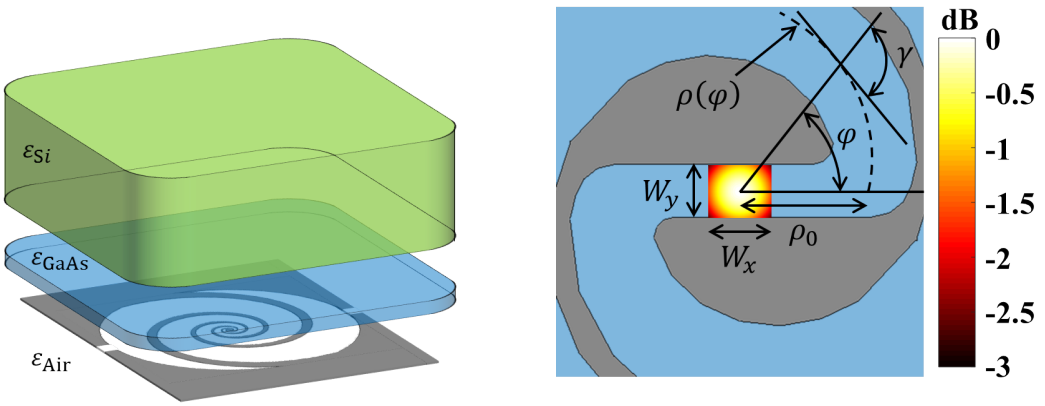

(c)

Figure 2.8: PCA geometries and structures: the dark blue slab represents the chip of photoconductive material; the green thick slab depicts the silicon semi-infinte medium; whereas the antenna metallizations are depicted in grey. a) Auston-switch antenna: gap size $W_x = W_y = 10\,\mu$m, dipole length $L_d = 30\,\mu$m and bias lines width $W_b = 10\,\mu$m. b) Bow-tie antenna: gap size $W_x = W_y = 10\,\mu$m and tapering angle 90°. c) Logarithmic spiral antenna: $\rho(\varphi) = \rho_0 e^{a\varphi}$ with $\varphi \in [0, 2\pi N]$, starting radius $\rho_0 = 23\,\mu$m, curvature angle $\gamma = 76.5°$, winding number $N = 2.6$, tapering angle $\delta = 150°$ and gap width $W_y = 10\,\mu$m. In the zoom of the gap of each antenna, the normalized laser power density distributions on the gaps, used for the evaluation of the energy spectrum, are shown.

The Auston-switch and the bow-tie do not present any particular design features, and the logarithmic spiral has been designed according to Chapter 5 with the limitation of designing a gap with length $W_y = 10\,\mu$m. The geometrical features of the antennas are listed in the caption of Fig. 2.8. The maximum sizes of the antennas are the same for all the three geometries $3\,\text{mm} \times 2\,\text{mm}$. The layered structure is the same for all of all three antennas: the antenna metallization is placed on a slab of $2\mu m$ LTG-GaAs, which is grown on a semi-insulating GaAs wafer, $525\,\mu$m thick with $\varepsilon_{GaAs} = 13$ (typical size and permittivity of a GaAs substrate used for PCAs). The antenna chip has been simulated by the EM commercial software [94], by considering the structure radiating between free space and a semi-infinite dense dielectric with $\varepsilon_{Si} = 11.9$, in order to approximate the effect of the presence of a silicon dielectric lens [54], typically used for such kind of devices for enhancing the directivity of the antenna.

The energy spectra radiated by the antennas in the silicon layer are derived by using (2.21) and are shown in Fig. 2.9, assuming that the photoconductive gaps are illuminated by a laser average power $P_{ave} = 30\,\text{mW}$, with a Gaussian beam of diameter at $-3\,\text{dB}$ $D_{laser} = 10\,\mu$m, a repetition rate $f_p = 80\,\text{MHz}$, pulse duration $\tau_p = 100\,\text{fs}$, and a bias voltage $V_{bias} = 40\,\text{V}$. Referring to Fig. 2.8, the sizes of the gap area illuminated by the laser beam for the three geometries have been considered as: $W_x = W_y = 10\,\mu$m for the Auston-switch and the bow-tie antenna, while $W_x = 12\,\mu$m and $W_y = 10\,\mu$m for the logarithmic spiral antenna due to the geometry of its gap. The features of the photoconductor

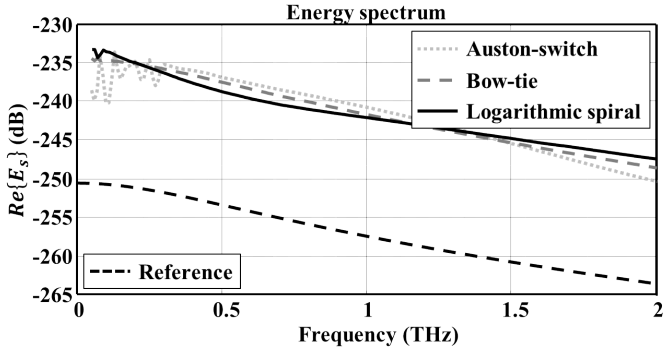

Figure 2.9: Simulated energy spectra E_s generated by the three antennas under analysis. The black dashed line is the reference energy spectrum, generated by the equivalent current generator $I_g(\omega)$ of the antennas, connected to a reference load $R = 1\,\Omega$.

material are the same used in Section 2.2 and Section 2.4 for the free carriers mobility. It is worth noting that the photoconductor generator is mismatched under such working conditions, providing a generator impedance $Z_g = 214\,\Omega$ for the Auston-switch and bow-tie antennas, and $Z_g = 193\,\Omega$ for the logarithmic spiral. The energy spectra of the antennas present almost the same behavior at the higher frequencies of the spectrum. Significant differences can be noticed at the lower frequencies where they show different behaviours due to the finiteness of the different geometries, which results in different resonance behaviours. Referring to (2.22)–(2.23), the average power $\bar{P}_{source}$ generated by the antennas

is practically the same: 342 μW, 339 μW, and 326 μW, respectively for the Auston-switch, bow-tie, and logarithmic spiral.

For sake of completeness, the reference energy spectrum, evaluated considering the equivalent current generator of the antennas connected to a reference load $R = 1\,\Omega$ at each frequency is also shown in Fig. 2.9.

It is worth noting that, referring to Table 2.1, the power $\bar{P}_{source}$ estimated for the antennas in the previous numerical example, does not constitute the maximum available power, because of the mismatching between the photoconductor equivalent circuit and the antenna impedance. Indeed, a gap with the same size of the antennas gap $W_x = W_y = 10\,\mu$m, illuminated with the same average laser power $P_{ave} = 30\,$mW, and same applied bias voltage $V_{bias} = 40\,$V, provides a higher available power $\bar{P}_{available}$, if it is connected to a matched antenna load, as it is shown in the first row of Table 2.1. Moreover, in Table 2.1 it is shown that focusing the same laser power on smaller gap, and keeping the same applied bias electric field on the gap, $E_{bias} \simeq V_{bias}/W_y$ (second column), does not change the maximum available power $\bar{P}_{available}$ provided by the source. Indeed, by focusing the laser beam on smaller gaps (columns one, three, and four in Table 2.1), the impedance of the equivalent generator decreases (fifth column in Table 2.1), whereas the current of the equivalent generator increases. In the sixth column of Table 2.1, we report the average current $\tilde{I}_g$ of the pulse on the time interval τ_σ. The resulting available power $\bar{P}_{available}$ for all the gap sizes is shown in the last column of Table 2.1.

Table 2.1: Estimated generator impedance Z_g, average current $\tilde{I}_g$ of a pulse on the time interval τ_σ, and available power $\bar{P}_{available}$ provided by the photoconductor gap using an average power of the laser $P_{ave} = 30\,$mW, and an applied bias electric field $E_{bias} = 4\,\text{V}/\mu$m.

Gap size	V_{bias} ($E_{bias} = 4\,\text{V}/\mu\text{m}$)	D_{laser}	**Fluence**	Z_g	$\tilde{I}_g$	$\bar{P}_{available}$
$10\,\mu\text{m} \times 10\,\mu\text{m}$	40 V	$10\,\mu$m	$0.21\,\text{mJ/cm}^2$	$214\,\Omega$	188 mA	$469\,\mu$W
$5\,\mu\text{m} \times 5\,\mu\text{m}$	20 V	$5\,\mu$m	$0.87\,\text{mJ/cm}^2$	$54\,\Omega$	376 mA	$469\,\mu$W
$2.5\,\mu\text{m} \times 2.5\,\mu\text{m}$	10 V	$2.5\,\mu$m	$3.47\,\text{mJ/cm}^2$	$13\,\Omega$	752 mA	$469\,\mu$W

A complete analysis of the energy spectrum and power radiated by the photoconductive antennas, together with a validation of the proposed equivalent circuit via power and spectrum measurements of some prototypes, will be shown and discussed in detail in Chapter 4.

2.6 Conclusions

In this chapter a novel Norton equivalent circuit model has been proposed to characterize the feed of photoconductive antennas. In particular the focus is on the pulsed operation mode (PW mode). The model takes into account the properties of the semiconductor material, the geometrical parameters of the source, and the laser excitation involved. The equivalent circuit can be used to evaluate the energy spectrum and the average power

radiated by a PCA. The model clarifies that the power generated and radiated by commonly used photoconductive antennas is in the order of some hundreds of microwatt. Instead, how much power can be used depends on the quasi optical coupling to the receiver. This aspect will be addressed in Chapter 4, together with an experimental validation. Therefore the equivalent circuit provides an effective tool to design and analyze PCAs, since it can be used to estimate and maximize the power radiated by PCAs.

Chapter 3

Analysis of the State of the Art of Photoconductive Antennas

This chapter presents the electromagnetic analysis of the most used antenna geometries for pulsed photoconductive antennas and the analysis of the their coupling with the reflectors chain, typically used for the measurements of such devices. The radiation behavior of the lens antennas, composed by photoconductive antenna and dielectric lens, are evaluated in terms of lens antenna efficiency, stressing all the losses which affect the radiation performances of these antenna feed geometries. Moreover, the coupling between such lens antennas and the reflectors chain is also investigated, leading to the evaluation of the the spillover and polarization efficiencies, which affect the radiation performances of the reflectors chain fed by such lens antennas. The results of such analysis will be used in Chapter 4, where the electromagnetic model of the entire experimental QO channel (source-to-detector) for PCAs will be discussed and used to compute the power budget of PCAs, resorting to the Norton equivalent circuit developed in Chapter 2.

3.1 Description of the Antenna Geometries

The three most common photoconductive antenna geometries that can be found in the literature have been analyzed. The antenna geometries are Auston switch, bow-tie, and logarithmic spiral antenna, which are shown in Fig. 3.1. All the structures have been designed to have the same maximum physical size, and the same distance of the feeding gap electrodes, in order to have a fair comparison of their performances. The Auston-switch and the bow-tie have standard design features, the logarithmic spiral has been designed according to Chapter 5 with the limitation of designing a gap with the same size of the other geometries. In detail, the geometrical features of the antennas are listed in the caption of Fig. 3.1. All antenna geometries have been assumed to be printed at the interface of a GaAs chip $\varepsilon_{GaAs} = 13$ with height $H_{GaAs} = 527\,\mu$m (the blue slab depicted in Fig. 3.1). A silicon lens with relative permittivity $\varepsilon_{Si} = 11.9$, radius $R_{lens} = 5\,$mm, and extension length $E_{lens} = 0.16 R_{lens}$ was chosen in order to increase the directivity of the

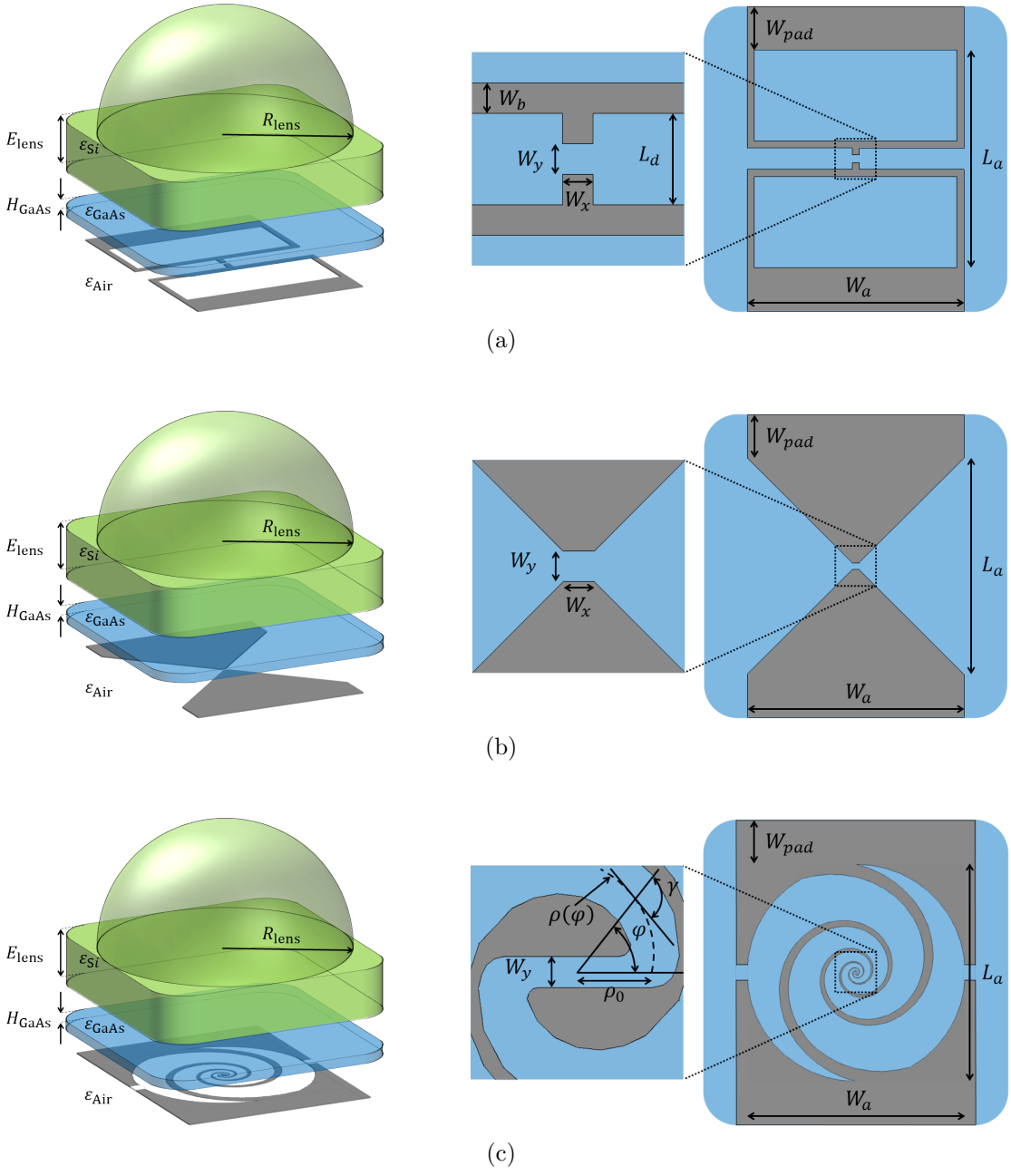

Figure 3.1: PCA prototype geometries under analysis. The blue slab represents the chip of photoconductive material; the green thick slab depicts the silicon lens; whereas the antenna metallizations are depicted in grey. a) Auston-switch antenna: gap size $W_x = W_y = 10\,\mu$m, dipole length $L_d = 30\,\mu$m and bias lines width $W_b = 10\,\mu$m. b) Bow-tie antenna: gap size $W_x = W_y = 10\,\mu$m and tapering angle 90°. c) Logarithmic spiral antenna: $\rho(\varphi) = \rho_0 e^{a\varphi}$ with $\varphi \in [0, 2\pi N]$, starting radius $\rho_0 = 23\,\mu$m, curvature angle $\gamma = 76.5°$, winding number $N = 2.6$, tapering angle $\delta = 150°$ and gap width $W_y = 10\,\mu$m. All three geometries have the same overall sizes and the bias pads width: $L_a = 2\,$mm, $W_a = 2\,$mm, and $W_{pad} = 0.5\,$mm.

antennas, obtaining almost an unidirectional radiation. The extension length was chosen to get an overall extension length, including the thickness of the chip, close to the ideal hyperhemispherical extension of the lens $0.29R_{lens}$. The choice of the hyperhemispherical lens has been dictated by the requirement of a constant lens directivity over the entire operative bandwidth, in order to maximize the aperture efficiency of the reflector.

3.2 Analysis of the Lens Antennas

The geometries have been simulated using an EM commercial software [94], assuming that the antenna chip radiate between free space $\varepsilon_{air} = 1$ and a semi-infinite dense dielectric medium $\varepsilon_{Si} = 11.9$ (the green thick slab depicted in Fig. 3.1), in order to simulate the presence of a dense dielectric lens [54].

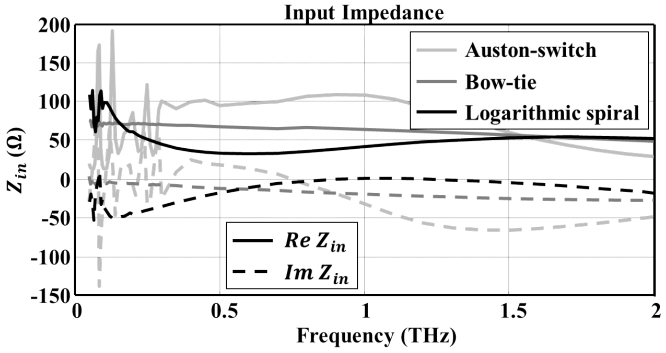

Figure 3.2: Simulated input impedance of the antenna geometries under analysis.

The input impedance of the simulated antennas is shown in Fig. 3.2. The imaginary parts of the impedance are smaller than the real parts for almost the entire bandwidth of interest. Different behaviors of the impedance are more emphasized at the lowest frequencies, due to the different resonance behaviors because of the finiteness of the different geometries.

The simulated radiation patterns in the semi-infinite dielectric (Primary fields) have been used to compute the fields radiated by the dielectric lens (Secondary fields) via a Physical Optic (PO) approach [30, 95].

3.2.1 Radiation Patterns Inside the Dielectric Lens

The simulated primary fields are shown in Section D.1 of Appendix D. The radiation patterns are plotted as co-polarization (Co-pol) and cross-polarization (Cross-pol) according to Ludwig's third definition [96] for the linear polarized antenna geometries, Auston-switch and bow-tie. Whereas the radiation patterns of the logarithmic spiral are plotted in Right-Handed Circular Polarization (RHCP) and Left-Handed Circular Polarization (LHCP), combining the two orthogonal linear polarization according to Ludwig's third

definition [96]. The same definitions are adopted for representing the radiation patterns outside the lens and outcoming from the reflectors chain that will be discussed below.

The radiation patterns of the Auston-switch (Section D.1.1) at lower frequencies do not illuminate uniformly the lens surface, due to the fact that the long bias lines contribute strongly to the radiation, radiating the fields mainly towards the lateral part of the lens. This effect is mitigated at higher frequencies, when the central small dipole becomes relevant with respect to the wavelength. The bow-tie antenna presents a more uniform illumination of the lens (Section D.1.2), but anyway most of the radiation is directed towards the lateral part of the lens, because of the leaky-wave phenomena that affects the planar antennas when they radiates at the interface of two dielectrics [97, 98]. Whereas, the illumination provided by the logarithmic spiral is more uniform and symmetric on the surface of the lens (Section D.1.3), and it is directed mainly towards the upper part of the lens surface as it is described in chapter 5. At higher frequencies the symmetry of the radiation patterns is degraded, since the inner part of spiral is too big in order to radiates symmetric patterns. Such limitation was dictated by the fact that the gap of the spiral had to be designed with the same size of the gap of the other antenna geometries.

3.2.2 Radiation Patterns Outside the Dielectric Lens

The simulated secondary patterns radiated by the dielectric lens, fed by the antenna feeds under analysis, are shown in Section D.2 in appendix D.

As consequence of the no efficient illumination of the lens provided by the Auston-switch, the dielectric lens fed by such antenna feed is not able to focus properly the fields in the broadside direction (Section D.2.1). This effect is mainly present at the lower frequencies, where the long bias line have a strong impact on the lens illumination. At higher frequencies, when the small dipole becomes relevant with respect to the wavelength, and the illumination of the lens surface is slightly more homogeneous, the secondary beams show a more clear beam pointing to broadside. The dielectric lens fed by the bow-tie antenna radiates more clear beams towards the broadside direction (Section D.2.2), due to the no uniform illumination of the upper part of the lens surface, the beams present some asymmetries on different planes, presenting different beam widths on different φ-planes. Moreover, the beams are broader than the ones that provide by an uniform illumination of the lens. Finally, thanks to the symmetric and homogenous illumination of the lens surface provided by the logarithmic spiral, the secondary patterns of the logarithmic spiral lens antennas presents more symmetric and narrower beams with respect to those ones provided by the other antennas (Section D.2.3).

For the analysis of the lens antenna fed by the three antenna geometries, all the losses which affect the radiation performance of the lens antennas have been computed and they have been quantified in terms of efficiency. In details, the following efficiencies have been evaluated: the front-to-back efficiency η_{fb}, defined as the ratio of power radiated in the semi-infinite dielectric medium and the total power radiated into the dielectric medium and backwards in the air; the polarization efficiency η_p, defined as the power radiated by the co-polar component and the total power radiated by both the polarizations; the reflection

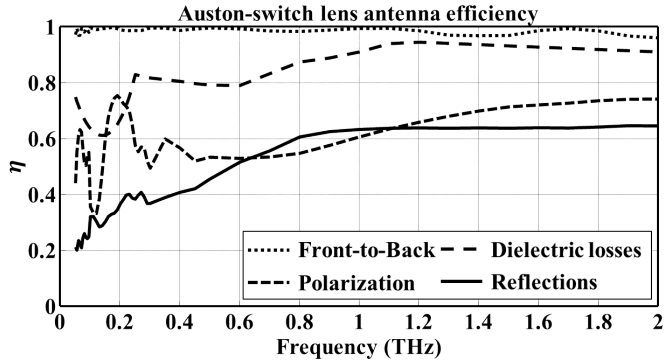

(a)

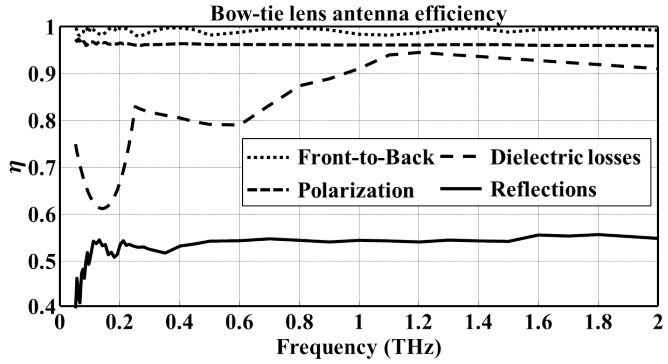

(b)

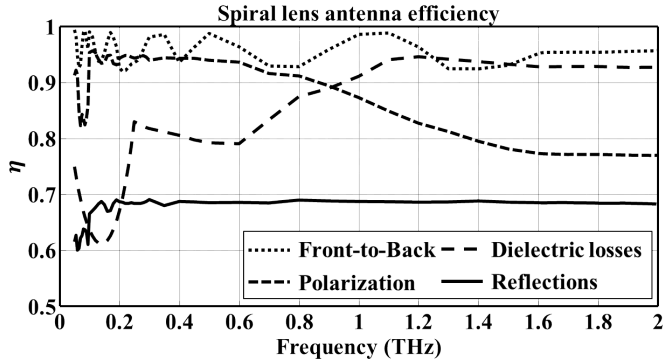

(c)

Figure 3.3: Efficiency of the dielectric lens fed by the antenna feed under analysis.

losses efficiency η_r at the lens-air interface, defined as the power radiated outside the lens (Secondary fields) and the power radiated inside the dielectric lens (Primary fields); and finally, the dielectric losses efficiency η_{dl} in the silicon according to [99]. Such efficiencies are shown in Fig. 3.3. The main contribution of losses for all the antennas comes from the reflection losses. The spiral which illuminates mainly the upper part of the lens surface

is less affected by such reflections, while the bow-tie presents higher reflections due to the strong illumination of the lateral part of the lens surface. At the lower frequencies, the reflections are even more accentuated for the Auston-switch, which also provides the lower polarization efficiency, because of the bias lines.

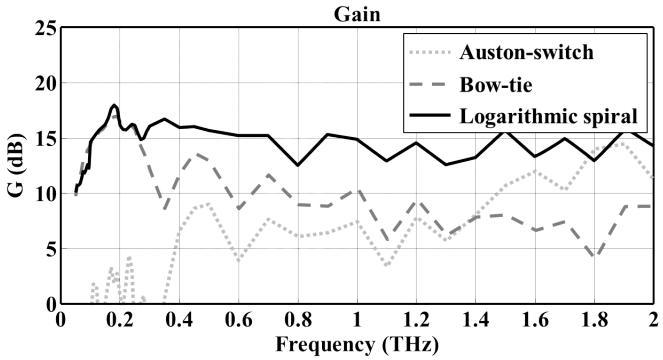

Figure 3.4: Simulated Gain of the lens antennas under analysis.

Finally, Fig. 3.4 shows the broadside gain of the three lens antennas under analysis over the operative bandwidth. The gain of the co-polar component has been computed taking into account for the losses previously mentioned, as follow:

$$G_{co}(f) = \eta_{fb}(f)\,\eta_r(f)\,\eta_{dl}(f)\,D_{co}(f) \tag{3.1}$$

where D_{co} is the directivity of the co-polar component at broadside direction. For the spiral lens antenna, which provides the best lens surface illumination, the behavior of the gain is quite constant over the frequency thanks to the selected extension length of the dielectric lens, whereas the bow-tie and the Auston-switch lens antennas provide a lower gain.

3.3 Analysis of the Reflectors Chain Performance Fed by the Lens Antennas

The reflectors chain of the measurement system used for experimental validation, which will be discussed in the Chapter 4, is shown in Fig. 3.5(a). It was composed of two 90° off-axis parabolic reflectors, and the sensor was coupled with the reflectors chain by means of a conical horn antenna WR-10 [100]. The features of the system are listed in its caption. The position of the PCA source with respect to the first reflector has been chosen in such a way to match the phase center of the hyperhemispherical lens antenna, placed behind the antenna plane $\Delta_{pc}^{PCA} = 16\,\text{mm}$, with the focal point of the parabolic reflector, $d_{t,1} = f_{R1} - \Delta_{pc}^{PCA} = 84\,\text{mm}$ as it shown in the left inset of Fig. 3.5(a). The conical horn WR-10 [100] connected to the sensor, with aperture diameter $D_{horn} = 16.3\,\text{mm}$ and length $L_{horn} = 35.5\,\text{mm}$, was located in such way that the phase center of the fundamental

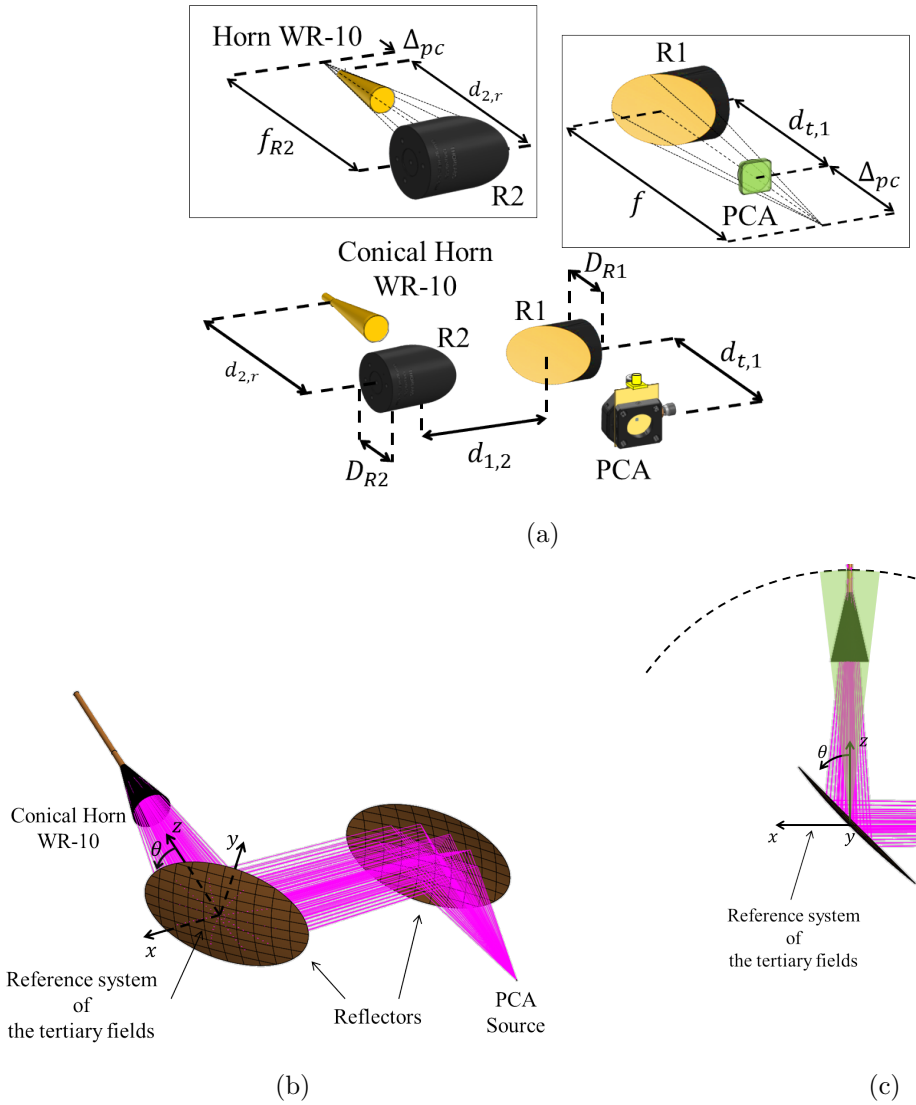

Figure 3.5: Measurement system under analysis. a) Measurement system geometry (source-to-detector); the geometrical features of the setups are: reflectors diameter $D_{R1} = D_{R2} = 50.8$ mm: reflectors f-number $f_{\#1} = f_{\#2} = 2$; distance emitter-first reflector $d_{t,1} = 84$ mm; distance reflectors $d_{1,2} = 95$ mm. The distance second reflector-horn antenna was $d_{2,r} = 90$ mm. b) EM model used in [101] for the analysis of the system. The purple lines represents the geometrical optic (GO) rays of the electromagnetic radiation from the PCA source to the conical horn antenna of the detector sensor. c) Reference system and semisphere surface for the evaluation of the tertiary fields in Section D.3 in Appendix D.

mode of the horn antenna, placed behind the horn mouth connected to the waveguide at a distance $\Delta_{pc}^{Horn} = 10$ mm, was at the focal point of the second reflector of the QO system, $d_{2,r} = f_{R2} - \Delta_{pc}^{Horn} = 90$ mm as it is shown in the right inset in Fig. 3.5(a).

The EM analysis of the reflectors chain fed by the three lens antennas has been performed by using a commercial software [101]. The radiation patterns discussed in the previous section, and shown in Section D.2 in the Appendix D have been used as feed for

the reflectors chain. The pair of reflectors have been simulated by a PO approach [101]. The simulated radiation patterns outgoing from the reflectors chain (Tertiary fields) are shown in Section D.3 of the Appendix D. Considering the reference system placed at the center of the second reflector surface, the radiation patterns have been evaluated on a semisphere with radius equal to the focal length of the reflector.

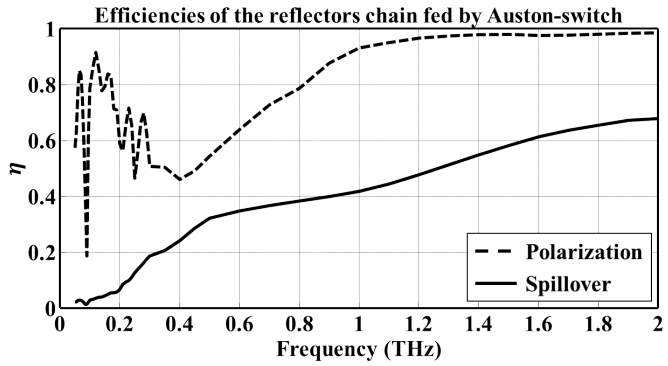

(a)

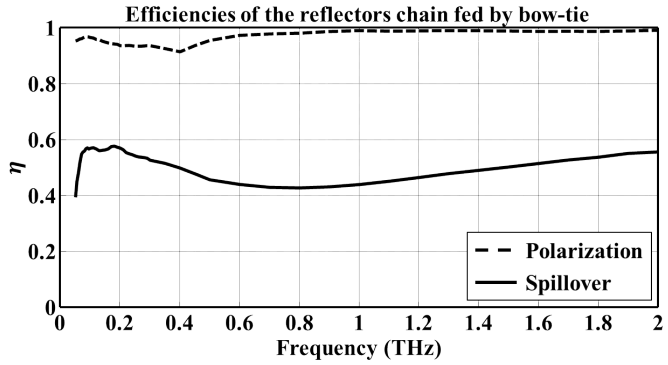

(b)

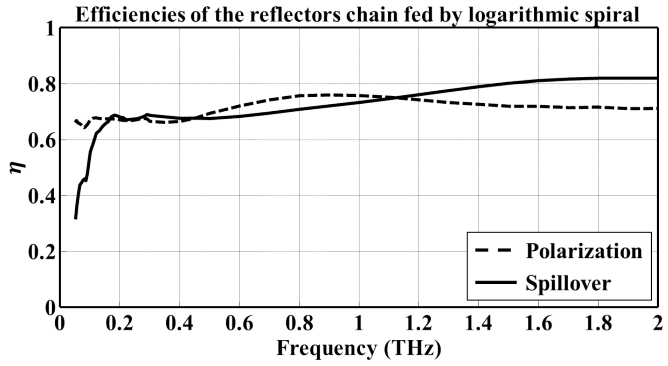

(c)

Figure 3.6: Efficiency of the reflectors chain fed by the lens antennas under analysis.

The radiation patterns of all the three geometries present an asymmetric behavior, because of the off-axis configuration of the reflectors. For the analysis of the reflectors chain, the losses due to the spillover and the polarization have been computed and their relevant efficiencies are shown in Fig. 3.6. The spillover efficiency introduced by the system η_{sp} has been defined as the ratio of the power captured by the second reflector of the chain and the incoming power of the system, and the polarization efficiency η_p has been defined as the outgoing power from the chain of the co-polar component and the total outgoing power radiated by both the polarizations (co-polar and cross-polar components). The spillover efficiency provided by the reflectors chain fed by the logarithmic spiral and the bow-tie lens antennas present a quite flat behavior over the operative bandwidth, thanks to quite constant directivity of the lens antennas, which illuminate the first reflector. The logarithmic spiral lens antenna present a higher spillover efficiency because it provides a higher directivity than the bow-tie. On the contrary, the Auston-switch provides a low spillover efficiency at lower frequencies, due to the fact that the dielectric lens does not focus the radiation towards the first reflector of the chain as it is shown in Section D.2.1 of Appendix D.

3.4 Conclusions

The electromagnetic analysis of the most used of photoconductive lens antennas and their coupling with a typical reflectors chain, used for measuring the power radiated by such devices, has been presented in this chapter. The analysis of the performances of the lens antennas stresses that the power radiated by the antenna feeds is mainly affected by the reflection losses at the lens-air interface. This is due to the wide radiation patterns radiated by the antenna feeds inside the dielectric. Moreover, it has been shown that the reflectors chain affects strongly the electromagnetic radiation, which propagates through the system, introducing spillover losses. Among the three antenna geometries, the Auston-switch provides the most critical behavior. In fact, in addition to the reflection losses, the not homogenous lens surface illumination, provided by this antenna feed, causes the dielectric lens is not able to focus properly the electromagnetic fields, making such lens antenna not suitable for feeding a reflectors system. The electromagnetic analysis of the lens antennas and their coupling with the reflectors chain is crucial when the devices have to be characterized by measurements, since it permits to have a clear picture of the losses on the power budget of the measurements system. The results of such analysis will be used in Chapter 4, where power and spectrum measurements of the photoconductive antenna prototypes analized in this chapter will be discussed, in order to provide an experimental validation of the Norton equivalent circuit developed in Chapter 2.

Chapter 4

Analysis of the Experimental QO Channel Power Budget

This chapter presents the experimental validation of the Norton equivalent circuit model discussed in Chapter 2. To this goal different prototypes of photoconductive antenna sources have been manufactured and assembled. The absolute powers generated and their pertinent spectra have been measured. In order to obtain a validation of the original equivalent circuit proposed, an auxiliary electromagnetic analysis of the complete setup, including the quasi optical links for the signals from the antenna feeds to the detectors had to be developed. By using the combined theoretical model (circuit and quasi optics), an excellent agreement is achieved between the measured and estimated power as well as the spectra. This agreement fully validates the circuit model, which can now be used to design new photoconductive antennas, including electrical features of the semiconductor materials, as well as the details of the antenna gaps and the purely quasi optical components.

4.1 Introduction

Many researchers have characterized the performances of PCAs [18, 20, 45, 51, 56, 57, 64, 67, 74] using measurements in the past. However, in most cases the analysis of the results was presented without having a characterization of the Quasi-Optical (QO) channel, which typically includes the lens antenna (PCA + lens), a chain of reflectors, and the detector. Such channels are typically extremely inefficient, causing the power detected to be smaller, in the order of tenths, than the one generated by the PCA. The lack of such quasi optical characterization for the channel typically renders impossible to calculate how much power was actually generated by the source, giving rise to the wide spread use of arbitrary units. In Chapter 2 of this thesis, a model to estimate the power radiated by a pulsed PCA source, based on its geometrical electrical and optical operating parameters has been presented. In this chapter a measurement setup is discussed, prototypes of standard PCAs are presented, and the absolute powers generated by the PCAs and their pertinent spectra have been measured. In order to deconvolve the impact of the quasi-optical path, a dedi-

cated accurate electromagnetic model for the channel has been developed, so that a power complete budget from the source to the detector has been characterized and completely validated by measurements.

The most commonly used geometries for PCAs have been chosen for the analysis: Auston-switch, bow-tie, and logarithmic spiral antennas, which have been characterized electromagnetically in Chapter 3. One prototype of each geometry has been manufactured, maintaining for all these sources the same geometrical gap dimensions, the semiconductor material, and the same optical and bias excitations. The power measurement setup was composed of an optical system that guides and collimates the laser beam, a QO channel, and a power detector. Two power detectors have been used (and the specific features of both have been retained in the analysis): a cryo-cooled bolometer with a high sensitivity and fast response [102], and a calorimetric power meter with a lower sensitivity and a slower response [100]. The bolometer has been calibrated and the power meter has been characterized with the same commercially available source [42]. Excellent agreement between the detectors gives high confidence on the accuracy of the power measurements. Moreover, spectral measurements have been carried out by using a different setup where an Electro-Optic (EO) crystal paired with balanced photodiodes was employed to measure the time-domain signal and spectrum.

The estimation of the power budget of each antenna has been made by computing the energy spectrum generated using the circuit model in Chapter 2, and then propagating coherently the associated waves to the detectors. A good agreement between the measurements and the theoretical results is found, certainly within the limited uncertainties of the measurement setup and material properties. The comparative analysis of the performances of the different PCAs provides clear evidence of the major impact of the antenna properties of the sources. The relevant detected energy spectra of the devices is significantly affected by the direction, within the lens, in which the relevant THz power generated is launched [54].

The present validation of the novel equivalent circuit allows the vast range of wide band microwave engineering tools that have been developed mostly for analyzing detectors in radiometric domains to be extended to PCA antenna design. The results of this chapter can be expected to open the way for more standard engineering optimization of wide band coherent THz sources [103].

The chapter is organized as follow: Section 4.2 describes the manufactured photoconductive antenna prototypes; Section 4.3 describes the measurement setups used for the power measurements; Section 4.4 presents the electromagnetic model which describes the measurement setups in terms of power efficiency; Section 4.5 discusses the estimation of the radiated and detected energy spectra and the relevant mean power for the different PCA prototypes; Section 4.6 and Section 4.7 present the power and spectrum measurement results and the relevant comparisons against the ones predicted by theoretical model, respectively. Finally, Section 4.8 discusses some concluding remarks.

4.2 PCA Prototypes Description

Three different photoconductive antenna geometries have been manufactured, in order to measure their radiated power and compare it with the results derived by the equivalent circuit model discussed in Chapter 2. The chosen antenna geometries are an Auston switch, a bow-tie, and a logarithmic spiral antenna, already discussed and analyzed in Chapter 3. The Auston-switch and the bow-tie have standard design features. The logarithmic spiral has been designed according to Chapter 5 with the limitation of designing a gap of length $W_y = 10\,\mu$m. The geometrical features of the antennas are listed in the caption of Fig. 3.1 in Chapter 3.

The three different devices were fabricated on the same semiconductor wafer. The layers structure of the chip is shown in Fig. 4.1(a). It is composed of a $2\,\mu$m thick LTG-GaAs layer grown on a 400 nm thick AlGaAs layer with 0.75% of Al content; itself grown on a GaAs buffer layer of thickness 200 nm placed on a $525\,\mu$m thick SI-GaAs wafer. The relative permittivity of the chip layers is about $\varepsilon_{GaAs} = 13$.

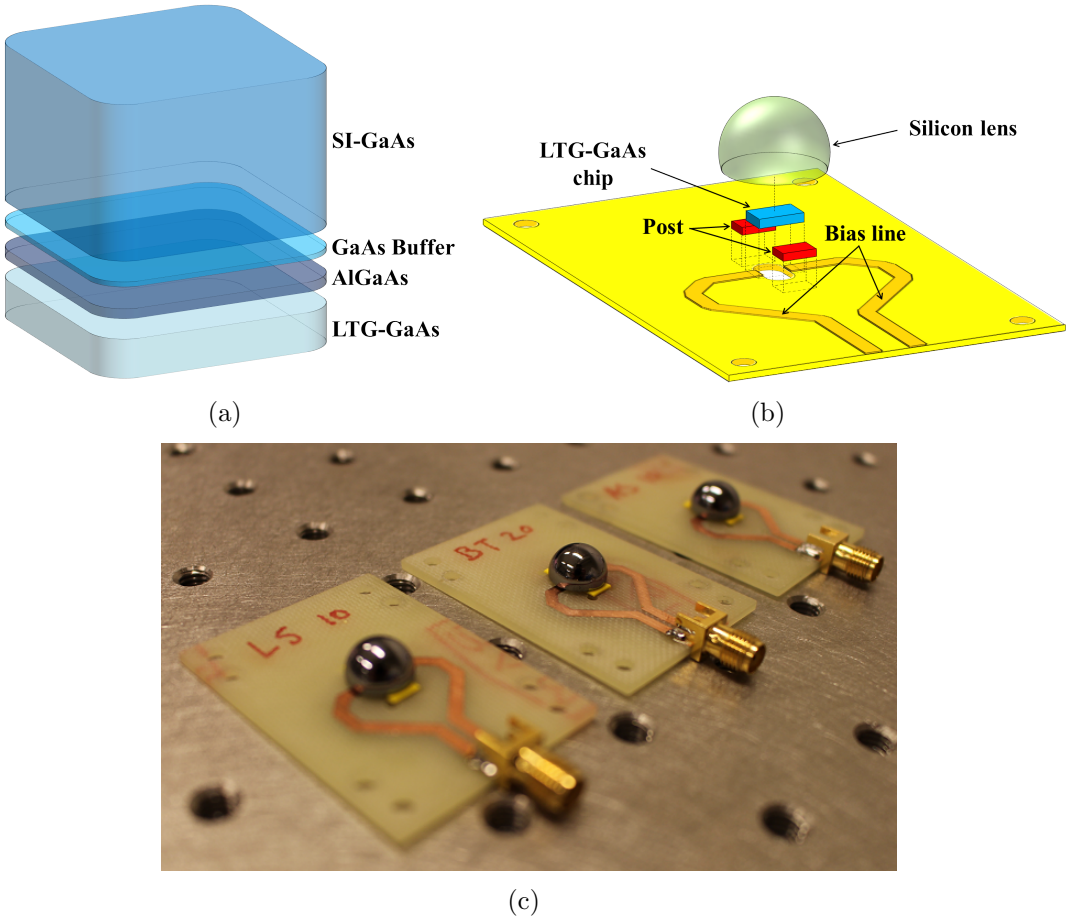

Figure 4.1: Photoconductive antenna prototypes and their components: a) layered structure of the LTG-GaAs chip used for the PCA prototypes, b) structure of the PCB used for biasing the PCAs, c) photoconductive antenna prototypes.

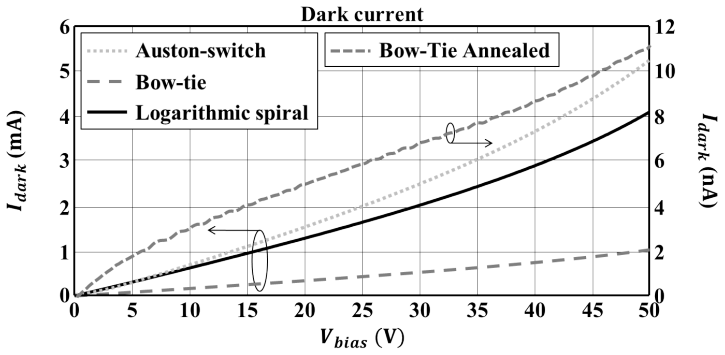

Figure 4.2: Measured dark current of PCA prototypes.

For most devices, the samples were fabricated without annealing [23, 89]. The lack of such process in the fabrication of the material results in low values of dark resistivity of the LTG-GaAs and, subsequently, high values of dark current in the devices, as it is shown in Fig. 4.2.

For comparison, an additional device, a bow-tie with identical geometrical details, has been manufactured on an annealed LTG-GaAs wafer [23]. Because of the annealing process such device presents a much lower dark current than the corresponding not annealed device, as it is also shown in Fig. 4.2.

Each antenna chip was mounted on a Printed Circuit Board (PCB), gluing the bias pads on the two bias lines printed on the PCB by means a conductive silver glue. On the opposite side of the patterned antenna metalization, a silicon lens with relative permittivity $\varepsilon_{Si} = 11.9$, diameter $D_{lens} = 10\,\text{mm}$, and extension length $E_{lens} = 0.16R_{lens}$ is placed. The extension length was chosen to get an overall extension length, including the thickness of the chip, close to the ideal hyperhemispherical extension of the lens $0.29R_{lens}$. The choice of the hyperhemispherical lens has been dictated by the requirement of a constant directivity over the entire operative bandwidth, in order to match a reflectors chain. The gluing of the lens has been made on two posts placed on the sides of the PCB aperture and slightly lower than the chip, in order to minimize any possible gap between the chip and the lens interface due to the glue itself, Fig. 4.1(b). The alignment procedure has ensured an accuracy of about $20\,\mu\text{m}$ on the placement of the lens with respect to the antenna center. The gluing procedure of the chip and the lens was performed in clean room (SRON, see Acknoledgment), in order to minimize the possible presence of dust particles. To provide the biasing voltage to the PCB lines, a SMA connector was soldered at the end of the bias lines. The fabricated PCA prototypes are shown in Fig. 4.1(c).

4.3 QO Channel Description

The power measurements have been carried out using the two different measurements setups shown in Fig. 4.3. Both setups were composed of the same optical and QO systems:

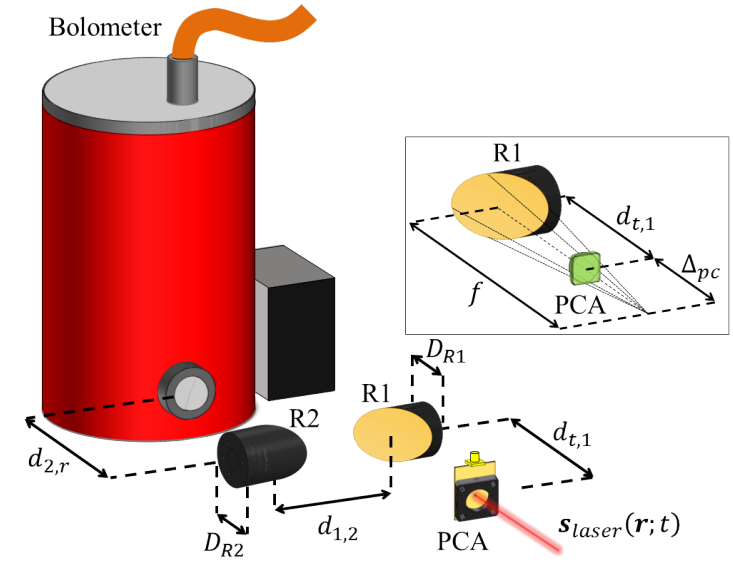

(a)

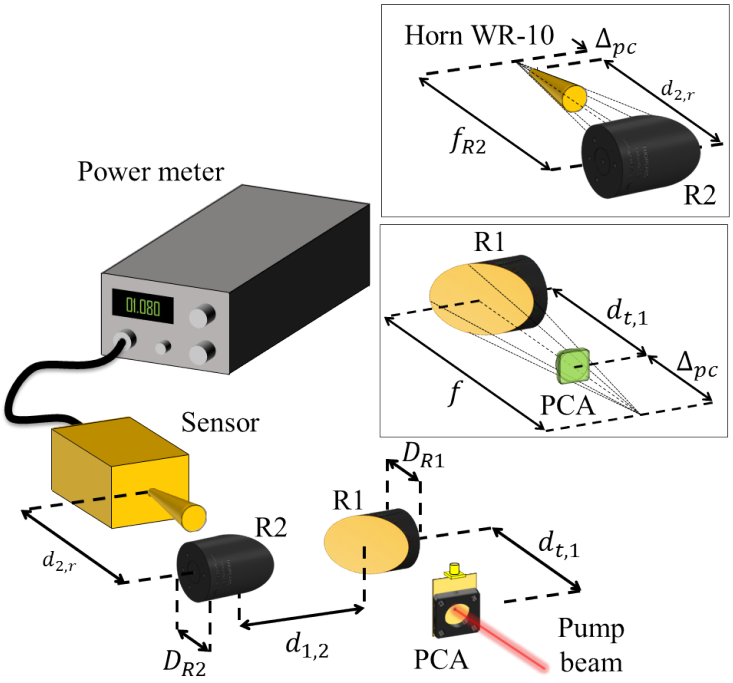

(b)

Figure 4.3: Measurement setups used to measure the power radiated by the photoconductive antenna prototypes, the optical system is not depicted in the figures. The geometrical features of the setups are: reflectors diameter $D_{R1} = D_{R2} = 50.8\,\text{mm}$: reflectors f-number $f_{\#1} = f_{\#2} = 2$; distance emitter-first reflector $d_{t,1} = 84\,\text{mm}$; distance reflectors $d_{1,2} = 95\,\text{mm}$. a) Bolometer based setup used for the alignment procedure. The distance second reflector-bolometer aperture was $d_{2,r} = 80\,\text{mm}$. b) Power meter based setup. The distance second reflector-horn antenna was $d_{2,r} = 90\,\text{mm}$.

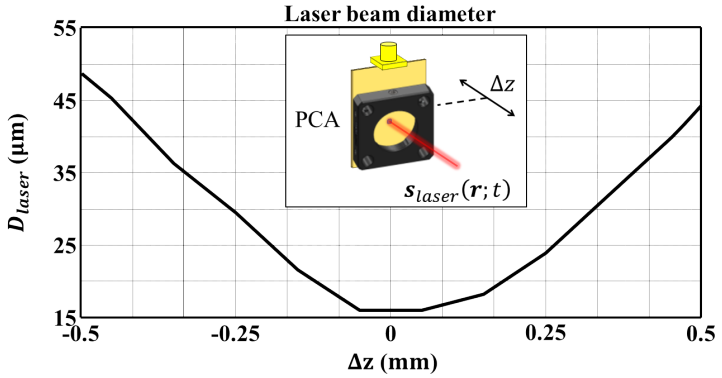

Figure 4.4: Measured laser beam diameter at −3 dB around the focal point of the laser focusing lens.

the first one was used to drive and focus the laser excitation $\mathbf{s}_{laser}(\mathbf{r};t)$ on the antennas' gap; whereas, the second one was used to focus the THz radiation emitted by the PCAs onto the detector. The only differences between the setups were the two different power detectors used.

A pulsed laser was used for the experiment. The laser presents the following features: carrier frequency $f_{laser} = 375$ THz (800 nm), pulse duration $\tau_p = 100$ fs, and pulse repetition rate $f_p = 80$ MHz.

The optical path of the laser beam ends with a 2.5 cm diameter achromatic lens with a focal length of 4.5 cm. The lens was used to focus the laser beam on the photoconductor gap of the PCA under test. The position of the focusing lens has been chosen so that the focal point of the focusing lens have been matched with the nominal position of the antenna gap. Since the uniform illumination of the entire surface of the focusing lens with the laser was not achieved, the actual numerical aperture of the lens was reduced. For this reason the width of the laser beam has been measured. Fig. 4.4 shows the laser beam diameter at −3 dB measured by means of the knife-edge technique on a longitudinal range of 1 mm and centered at the focal point of the focusing lens. The minimum laser beam diameter (−3 dB power level with respect to the maximum) obtained by such lens was $D_{laser} = 16.5\,\mu$m, which ensured a nearly uniform illumination of the PCAs' gap, once the antenna gap was aligned to the laser beam at the focal point of the lens. The QO system was composed of two 90° off-axis parabolic reflectors. The features of the system are listed in the caption of Fig. 4.3. The position of the emitter with respect to the first reflector has been chosen in such a way to match the phase center of the hyperhemispherical lens antenna, placed behind the antenna plane $\Delta_{pc}^{PCA} = 16$ mm, with the focal point of the parabolic reflector, $d_{t,1} = f_{R1} - \Delta_{pc}^{PCA} = 84$ mm as it shown in the insets of Fig. 4.3(a)-4.3(b). The first detector, used to perform the alignment procedure, was a cryo-cooled bolometer [102]. The bolometer was operating at a temperature of 4 K with a lock-in frequency of 167 Hz, to reach a sensitivity of about $-35\,\text{dB}\mu$. A Winston cone, with f-number $f_{\#} = 3.5$, mounted on the cold plate, collected the power coming from the QO system. The aperture of the bolometer was at a distance $d_{2,r} = 80$ mm from the center of

Figure 4.5: Measurement setup used for the alignment of the photoconductive antenna and the laser beam.

the second reflector of the QO system. The calibration of the bolometer was performed by using an autocalibrating absolute Power Meter [104] and a commercial photomixer [42], in order to derive the calibration factor to be used for converting the voltage readout of the lock-in amplifier in the measured power. The bolometer was used to perform the alignment of the antenna gap with the laser beam, as well as to measure the radiated power of the PCA prototypes.

The second detector, used for the measurement, was a room temperature calorimetric power meter [100], where the sensor is coupled with the QO system via a conical horn antenna WR-10. Performing an off-on-off measurement procedure [100, 105], such detector can reach a sensitivity of $-5\,\mathrm{dB}\mu$. The characterization of such detector was also performed by using a commercial photomixer with known output power [42] and it is shown in detail in Appendix E. The conical horn WR-10 [100] connected to the sensor, with aperture diameter $D_{horn} = 16.3\,\mathrm{mm}$ and length $L_{horn} = 35.5\,\mathrm{mm}$, was located in such way that the phase center of the fundamental mode of the horn antenna, placed behind the horn mouth connected to the waveguide at a distance $\Delta_{pc}^{Horn} = 10\,\mathrm{mm}$, was at the focal point of the second reflector of the QO system, $d_{2,r} = f_{R2} - \Delta_{pc}^{Horn} = 90\,\mathrm{mm}$ as it is shown in the inset in Fig. 4.3(b). For both the setups a 5 mm thick filter screen of Polytetrafluoroethylene (PTFE) was placed between the second reflector and the detector, in order to screen possible InfraRed (IR) power coming from the source (this screen is not depicted in Fig. 4.3). A picture of the measurement setup with the bolometer is shown in Fig. 4.5.

4.4 Analysis of the QO Channel

For sake of compactness, only the analysis of the power meter setup is shown in this section. The same analysis can be conducted for the bolometer setup.

The three antenna chip geometries, mentioned in Section 4.2, have been simulated by the EM commercial software [94], assuming the chip structure to radiate between free space and a semi-infinite dense dielectric medium, which simulates the presence of the dielectric silicon lens [54].

By using the simulated radiation patterns from the lens, shown in Appendix D.2, the power P_l radiated by the lens has been computed as the integral of the radiated power density distribution outside the lens. The radiation efficiency of lens antenna η_l have been evaluated as the ratio between the power P_l and the power P_{source} generated at the input port of the antenna at each frequency:

$$\eta_l(\omega) = \frac{P_l(\omega)}{P_{source}(\omega)} \tag{4.1}$$

η_l takes into account the front-to-back losses; the dielectric losses of the silicon according to [99], and the reflection losses at the lens interface [95]. The metalizations ohmic losses have not been considered since they are negligible. The lens antenna efficiency of each prototypes is shown in Fig. 4.6(a). The logarithmic spiral and the bow-tie lens feeds present a quite constant efficiency behaviour over the operative bandwidth. The spiral lens antenna is slightly more efficient than the bow-tie lens antenna because of the broadside radiation of the spiral feed inside the lens, as shown in Chapter 5, which decreases the reflection losses with respect to the bow-tie antenna, which indeed illuminates consistently the lateral part of the lens [54]. More critical is the radiation efficiency of the Auston-switch lens antenna. The long bias lines contribute strongly to the radiation at the lower frequencies, illuminating the lens mainly in the lateral part and resulting in very high reflection losses [54].

In order to analyze the behaviour of the QO system when it was fed by the PCA prototypes, the electromagnetic behaviour of the reflectors system has been simulated by means of a PO approach implemented in the commercial software [101]. The fields used to illuminate the first reflector was the one estimated by the PO lens simulations. The power P_{rs}, captured by the last reflector, has been evaluated as the integral of the radiated power density distribution of the electromagnetic field impinging on the surface of the last reflector of the reflectors system. The reflectors system efficiency η_{rs} is defined as the ratio between the power P_{rs} and the power P_l at each frequency:

$$\eta_{rs}(\omega) = \frac{P_{rs}(\omega)}{P_l(\omega)} \tag{4.2}$$

η_{rs} takes into account the spillover losses of the reflectors chain. The reflectors system efficiency for each prototype illumination is shown in Fig. 4.6(b). The hyperhemispherical lens geometry, discussed in Section 4.2, has been chosen in such a way that the first

reflector was illuminated with radiation pattern beams at about $-10\,\mathrm{dB}$ over the entire bandwidth, then the antennas were placed at the position where their phase center and the focus of the first reflector were matched. The choice of this location for the lens antennas also permits the reflector surface to be fed with a nearly constant phase radiation pattern. The highest spillover efficiency is from the reflectors system fed by the logarithmic spiral lens antenna over the entire bandwidth due to the better lens illumination. The broadside field radiated by the spiral lens feed illuminates more homogeneously the upper part of the lens, see Chapter 5, resulting in more focused beams radiated by the lens. The lower spillover efficiency provided by the reflectors system fed by the bow-tie is due the consistent illumination of the lateral part of the lens [54], which indeed results in broader radiated beams in one plane with respect to an ideal uniform lens illumination. Concerning the Auston-switch feeding, since it illuminates the lateral part of the lens at the lower frequencies [54], the patterns radiated by the lens are not well focused, thus spreading the radiated energy outside the reflector area. Consequently the reflectors system suffers from high spillover losses. At the higher frequencies, the radiation of the small dipole becomes more relevant than the one that comes from the long bias line, thus providing a more homogeneous illumination of the upper part of the lens similar to the bow-tie, which results in a reduction in the spillover and an increase in efficiency.

Finally, the coupling between the beam emerging from the last reflector, shown in Appendix D.3, and the detector has been simulated by a Method of Moment (MoM) implemented in the commercial software [101]. The input electromagnetic field to the MoM was the one calculated by the simulation of the reflectors system. The power P_d, impinging on the sensor at the end of the waveguide inside the detector, has been evaluated by integrating the power density distribution of the electromagnetic field traveling inside an infinite waveguide. The detector efficiency for quantifying the coupling between the field focused by the reflectors system and the detector has been defined as the ratio between the power P_d and the power P_{rs} at each frequency, namely:

$$\eta_d(\omega) = \frac{P_d(\omega)}{P_{rs}(\omega)} \tag{4.3}$$

η_d takes in to account the coupling losses between the reflectors system, the conical horn antenna, and the waveguide inside the detector. The detector efficiency of each prototypes is shown in Fig. 4.6(c). The position of the detector has been chosen in such a way that the phase center of the fundamental mode of the conical horn antenna was matched with the focus of the second reflector, in order to maximize the coupling between the reflectors system and the detector. The reflectors system fed by the bow-tie and the logarithmic spiral PCA present high coupling efficiencies with the detector. On the contrary, the reflectors system fed by the Auston-switch presents a lower coupling efficiency, especially at the lower frequencies, since the reflectors system suffers of the poor focusing of the beam into the detector. This is again due to the poor illumination of the reflectors system provided by the radiation pattern of the lens fed by the Auston-switch antenna. Since part of the power meter consists of a WR-10 waveguide, one can note that the detector does not absorb the power below the cut-off frequency of the fundamental mode of the waveguide

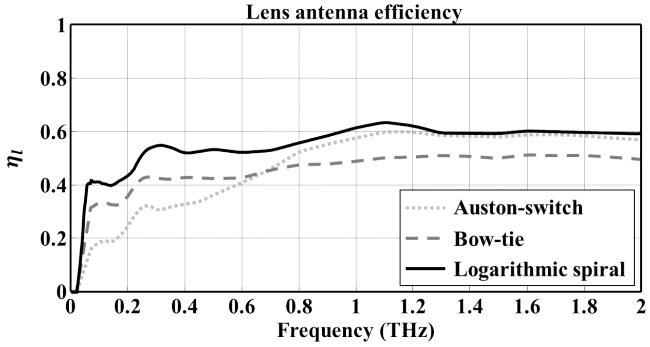

(a)

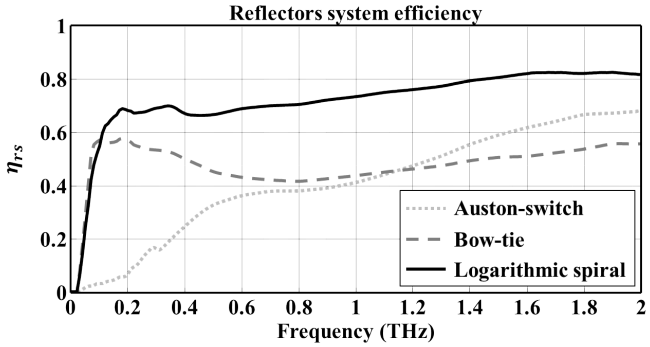

(b)

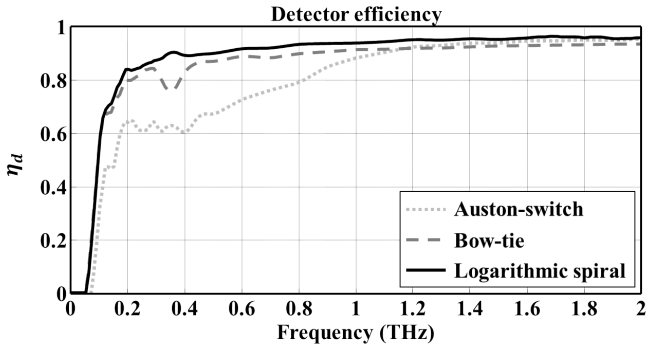

(c)

Figure 4.6: Simulated efficiencies of the measurement setup: a) lens antenna efficiency η_l, b) reflectors system efficiency η_{rs}, c) detector efficiency η_d.

$f_{c_{1,0}} = 59\,\mathrm{GHz}$. Moreover, because of the very large operative bandwidth, high-order modes are excited in the waveguide at the higher frequencies.

The product of the three efficiencies discussed above determines the efficiency η_{qo} of the entire QO channel at each frequency:

$$\eta_{qo}(\omega) = \eta_l(\omega)\,\eta_{rs}(\omega)\,\eta_d(\omega) \tag{4.4}$$

The QO efficiency η_{qo} is shown in Fig. 4.7. The measurement setup fed by the bow-tie presents a nearly flat total efficiency over the entire operative band. The logarithmic spiral presents a better total efficiency with an increasing behavior as the frequency increases. The higher efficiency provided by the logarithmic spiral feed with respect to the bow-tie feed is due to the better illumination of the lens provided by the pattern radiated by the spiral.

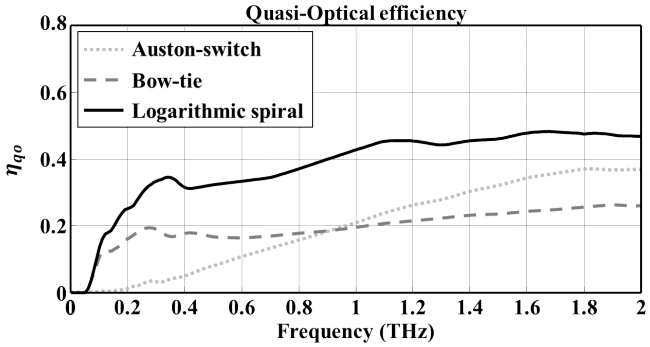

Figure 4.7: Simulated quasi-optical efficiency η_{qo} of the measurements setup.

4.5 Estimation of the Radiated and Measured Energy Spectra and Power

The energy spectra E_s associated to each PCA prototypes are calculated by using the Norton equivalent circuit described in Chapter 2 and the simulated antenna impedances discussed in Chapterchapter:analysis of the photoconductive antennas. The working parameters are a bias voltage $V_{bias} = 40\,\mathrm{V}$ and a laser average power $P_{ave} = 30\,\mathrm{mW}$. The laser power was assumed to be completely focused on the photoconductive gap according to laser beam measurement performed in the measurements setup. Therefore, for the calculation of the energy spectra, the laser beam diameter has been considered to be the minimum size measured, $D_{laser} = 16.5\,\mu\mathrm{m}$, as it shows in Fig. 4.4. Referring to Fig. 4.8, the sizes of the gap area illuminated by the laser beam for the three geometries have been considered as follows: $W_x = W_y = 10\,\mu\mathrm{m}$ for the Auston-switch and the bow-tie antenna, whereas $W_x = 12\,\mu\mathrm{m}$ and $W_y = 10\,\mu\mathrm{m}$ for the logarithmic spiral antenna due to the geometry of its gap.

The absorption coefficient and carrier lifetime of the LTG-GaAs layers used for the modeling of the PCA prototypes are $\alpha = 10^6\,\mathrm{m}^{-1}$ and $\tau = 0.3\,\mathrm{ps}$, respectively. The carriers mobility of the not annealed LTG-GaAs was considered to be $\mu = 60\,\mathrm{cm}^2/\mathrm{Vs}$, in agreement to what discussed in [89–91]. Such low values of carriers mobility is due to the fact that the material was manufactured without being annealed, thus resulting in a low resistivity material [23, 89]. This implies a high dark current (Fig. 4.2) and, subsequently, a high working temperature, which affects the carriers mobility [19, 61, 89–91]. Whereas,

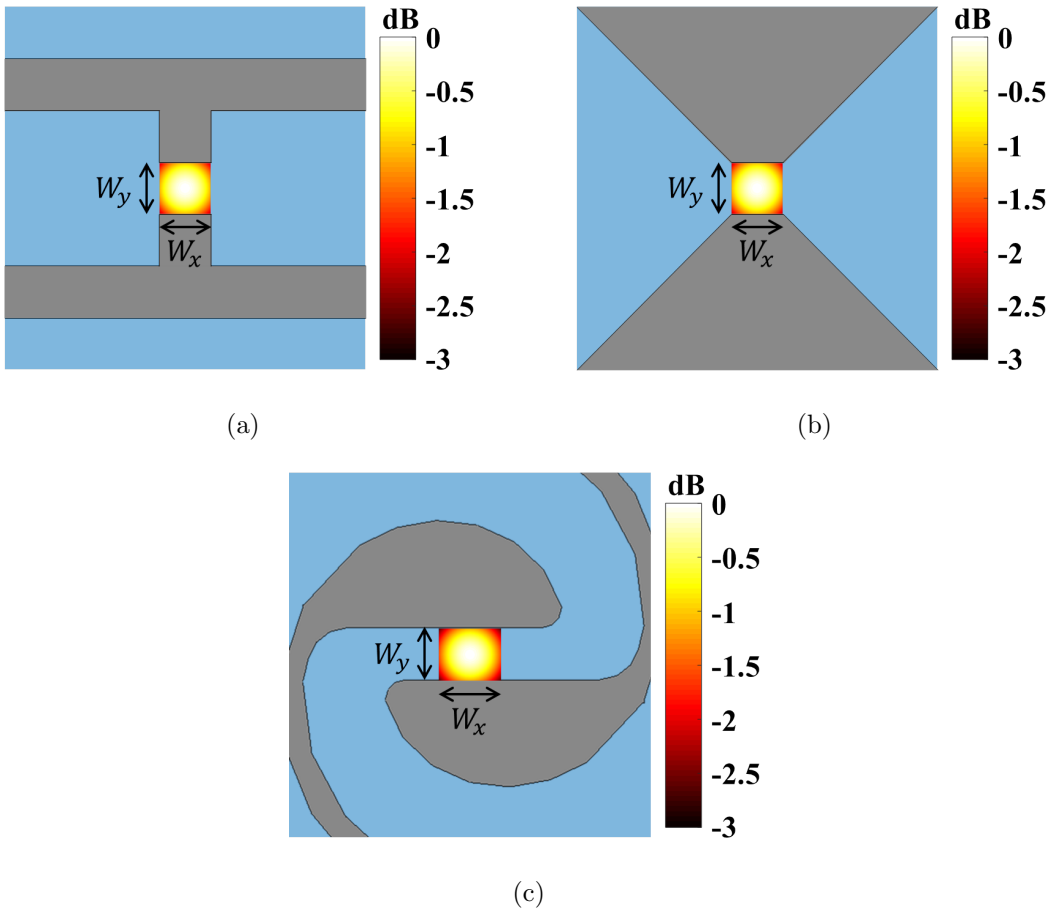

Figure 4.8: Laser beam illumination of the different antenna gaps for the evaluation of the energy spectra E_s radiated by the photoconductive prototypes.

the carriers mobility of the annealed LTG-GaAs was considered to be $\mu = 240\,\mathrm{cm}^2/\mathrm{Vs}$, in agreement with the discussion in [33, 56, 88].

The real part of the energy spectra radiated by the antennas are shown in Fig. 4.9(a). They have similar behaviour at the higher frequencies. Significant differences can be appreciated at the lower frequencies, where the antennas present different resonant behaviours due to the finite extents of the different structures.

Having the complete characterization of the measurement setup in terms of efficiency at each frequency, one can estimate the received energy spectrum E_m, starting from the generated energy spectrum of the antenna E_s as:

$$E_m(\omega) = \eta_{qo}(\omega)\, E_s(\omega) \tag{4.5}$$

The estimation of the real part of the measured energy spectrum is shown in Fig. 4.9(b). One can note that the different radiation features of the antennas, and the relevant interaction with the measurement system setup, affect the estimation of measured energy spectrum in different ways. The spectra of the logarithmic spiral and bow-tie are similar,

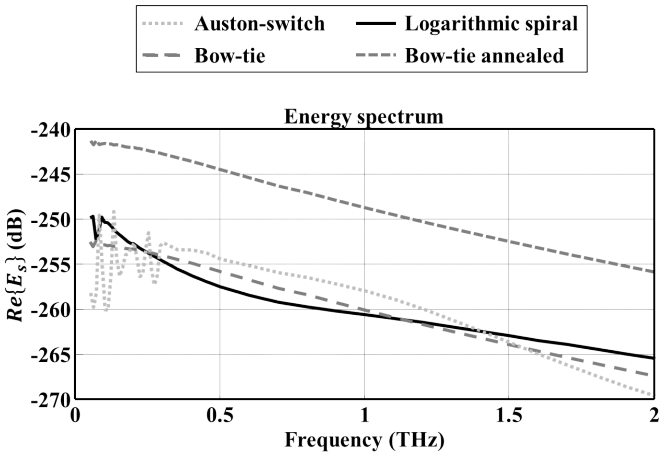

(a)

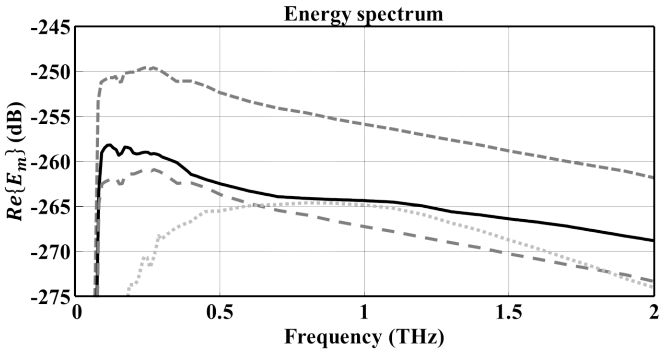

(b)

Figure 4.9: Simulated energy spectra of the PCA prototypes: a) generated energy spectra E_s; b) received energy spectra E_m.

showing only a different attenuation over the bandwidth, due to the higher lens reflection losses and spillover losses of the bow-tie antenna with respect to the logarithmic spiral. On the contrary, the estimation of the measured spectrum of the Auston-switch shows a strong attenuation of the components at the lower frequencies.

The single pulse radiated (E_{source}) and measured (E_{meas}) energy can be calculated by integrating the relevant energy spectrum, respectively, i.e.:

$$E_{source,meas} = \frac{1}{2\pi} \int_{-\infty}^{+\infty} E_{s,m}(\omega)\, \mathrm{d}\omega \tag{4.6}$$

Since the PCA radiates pulses periodically with a period $T_p = 1/f_p$, where f_p is the repetition rate of the laser, the average power radiated and measured can be calculated, respectively, as:

$$\bar{P}_{source,meas} = \frac{E_{source,meas}}{T_p} \tag{4.7}$$

Table 4.1: Estimated and measured average power of the PCAs.

	Generator Impedance Z_g	**Estimated Power**			**Measured Power**	
		$\bar{P}_{available}$	$\bar{P}_{source}$	$\bar{P}_{meas}$	**Bolometer**	**Power meter**
Auston-switch not annealed	$2.25\,\mathrm{k}\Omega$	$44.6\,\mu\mathrm{W}$	$5.8\,\mu\mathrm{W}$	$0.6\,\mu\mathrm{W}$	$0.4\,\mu\mathrm{W}$	$0.5\,\mu\mathrm{W}$
Bow-tie not annealed	$2.25\,\mathrm{k}\Omega$	$44.6\,\mu\mathrm{W}$	$5.0\,\mu\mathrm{W}$	$0.8\,\mu\mathrm{W}$	$0.8\,\mu\mathrm{W}$	$0.7\,\mu\mathrm{W}$
Logarithmic spiral not annealed	$1.90\,\mathrm{k}\Omega$	$51.7\,\mu\mathrm{W}$	$5.2\,\mu\mathrm{W}$	$1.4\,\mu\mathrm{W}$	$1.1\,\mu\mathrm{W}$	$1.2\,\mu\mathrm{W}$
Bow-tie annealed	$564\,\Omega$	$178.3\,\mu\mathrm{W}$	$67.7\,\mu\mathrm{W}$	$11.2\,\mu\mathrm{W}$	$10.3\,\mu\mathrm{W}$	—

As can be seen in Table 4.1 (fourth column), similar values of average power radiated $\bar{P}_{source}$ have been estimated for each antenna geometry with the not annealed LTG-GaAs substrate. A significant higher value is obtained with the annealed LTG-GaAs substrate. The values of the measured power $\bar{P}_{meas}$ of the three PCA prototypes (evaluated by the procedure mentioned above) are listed in the fifth column of Table 4.1. Comparing the not annealed devices first, as expected, the logarithmic spiral provides the highest value of detected power, meanwhile the Auston-switch provides the lowest one. However, all the antennas provide a poor total efficiency. Only the 28%, 16%, and 10% of the power $\bar{P}_{source}$ radiated by the spiral, the bow-tie, and the Auston-switch, respectively, is expected to be measured.

Furthermore, as can be seen in Table 4.1, under the working conditions, the equivalent Norton photoconductive generators, which fed the antennas, are mismatched since they present values of the equivalent generator impedance much higher than the real part of the input impedance of the antennas, which are on the wide operative bandwidth (i.e. $0.05\,\mathrm{THz} - 2\,\mathrm{THz}$) in a range of $30\,\Omega - 170\,\Omega$ for the Auston-switch, $50\,\Omega - 70\,\Omega$ for the bow-tie, and $30\,\Omega - 110\,\Omega$ for the logarithmic spiral. The annealed material presents a value of generator impedance much lower than the not annealed ones. However, this value is still too high to perform an ideal impedance matching with any antenna. Indeed, the radiated energy spectrum $E_s(\omega)$ can be related to the energy spectrum $E_s^{max}(\omega)$ associated to the maximum available energy provided to the antenna, if the antenna load matches the equivalent generator impedance, as defined by (2.25) in Chapter 2:

$$E_s(\omega) = \eta_m(\omega)\, E_s^{max}(\omega) \tag{4.8}$$

The maximum available average power $\bar{P}_{available}$ can thus be estimated by integrating the relevant energy spectrum:

$$\bar{P}_{available} = \frac{1}{2\pi T_p} \int_{-\infty}^{+\infty} E_s^{max}(\omega)\, \mathrm{d}\omega \tag{4.9}$$

The maximum available average power provided by the antennas under the working condition of the experiment are listed in the third column of Table 4.1. The results show

clearly that the power $\bar{P}_{source}$ radiated by the antennas is much lower than the available one $\bar{P}_{available}$, due to the fact that the photoconductor sources are mismatched with the antenna loads.

4.6 Measured Power of the PCA Prototypes

The power measurement procedure was composed by two phases, by using the two detectors described in Section 4.3. The cryo-cooled bolometer was used to perform the alignment of the antennas with the laser beam, because of the faster response of the bolometer with respect to the one of the power meter. Once that the optimal alignment of the antenna with the laser and the QO system was achieved, ensuring to have maximized the read out of the lock-in amplifier, the value of the measurement was acquired. After, the bolometer was replaced by the power meter sensor, and the measurement was acquired again, performing the off-on-off measurement procedure. The antennas under test were measured using the laser average power and bias voltage mentioned in Section 4.5. The devices were biased with a voltage square wave with frequency $f_{bias} = 7\,\text{kHz}$, and a duty cycle of 50%. A chopper was placed in the optical path before the focusing lens and provided the reference frequency of the lock-in amplifier. Similar values of average power have been measured by both detectors for each prototypes and they are listed in the last two columns of Table 4.1 (since during the power measurements of the annealed device the VDI power meter was not available, the relevant measure is not present in the table). In order to have a fair comparison between the values measured with both detectors, the readout of the power meter has been divided by the duty cycle factor of the bias voltage signal. The values of the measured powers of all the devices find a good agreement with the values of the detected power $\bar{P}_{meas}$ evaluated by using the proposed equivalent circuit.

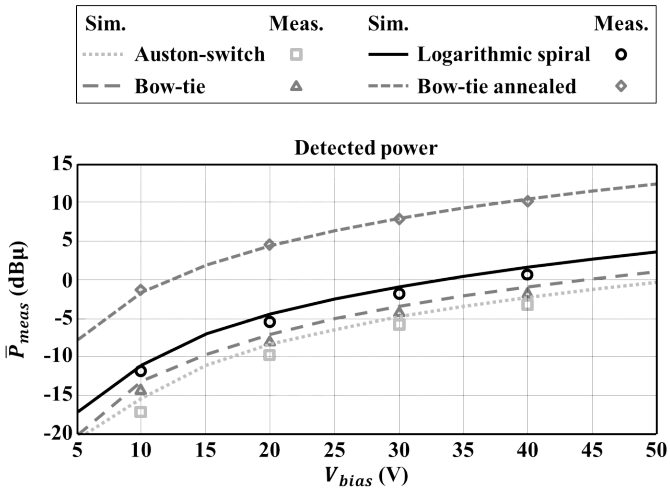

Figure 4.10: Measured power and power $\bar{P}_{meas}$ estimated by using the equivalent circuit versus the bias voltage applied of the PCAs.

Furthermore, a comparison between the power $\bar{P}_{meas}$ estimated and measured by varying the applied bias voltage is also shown in Fig. 4.10. In this case the values of measured power refer to measurements conducted with the bolometer, since the sensitivity of the power meter was not enough to detect such low power levels emitted by the not annealed devices with low values of bias voltage V_{bias}. Again, the prediction of the model is in very good agreement with the measurement results.

4.7 Measured Spectra of the PCA Prototypes

The spectra of the PCA prototypes have also been measured by using the Electro-Optic (EO) sampling technique [38]. A 2 mm thick ZnTe crystal paired with balanced photodiodes was used. The signal was recorded using a lock-in amplifier, referenced to the emitter bias modulation frequency. The measurements have been carried out in a purged environment with dry air, in order to eliminate any water absorption. According to the EO sampling technique, the radiated THz pulse is measured, by estimating the differential current flowing in the photodiodes. Such current is proportional to the amplitude of the pulsed electric field impinging on the crystal at the sampling instant [106]. Since the current pulse measured by the photodiodes is proportional to the THz electric field illuminating the crystal, it is possible to compare the Fourier Transform (FT) of the squared amplitude of the measured current pulse against the energy spectrum E_r captured by the last reflector of the reflectors system evaluated by using the electromagnetic model proposed in this paper, i.e.,

$$E_r(\omega) = \eta_l(\omega)\,\eta_{rs}(\omega)\,E_s(\omega) \tag{4.10}$$

The normalized amplitude spectra of the measured pulse of the different PCA prototypes and the relevant estimated real part of the energy spectra E_r are shown in Fig. 4.11.

It is worth noting that the measured spectra are also affected by the response of the EO crystal excited by the THz pulse, which is not known both in amplitude and in phase. Hence, the comparison is only qualitative. On the contrary, the estimated spectra E_r do not take into account such response. One can note a fair agreement between the simulated and measured spectra, especially for the Auston-switch (Fig. 4.11(a)) and the bow-tie antenna (Fig. 4.11(b)). For the logarithmic spiral antenna the behaviour of the curves is slightly different (Fig. 4.11(c)). A further investigation showed that the EO crystal presents an anisotropic behaviour. This significantly affects the measurement of the field radiated by the logarithmic spiral antenna, whose radiated field is elliptically polarized. Such anisotropic behaviour can be appreciated in Fig. 4.12, which shows the ratio between two spectrum measurements obtained by two orthogonal orientations of the EO crystal.

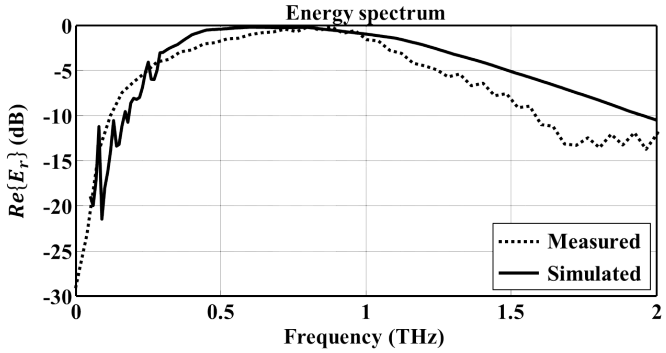

(a)

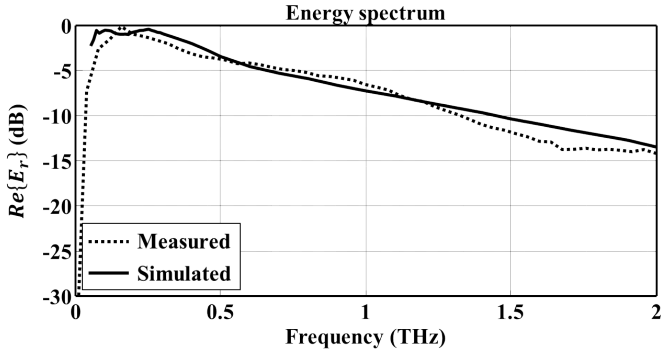

(b)

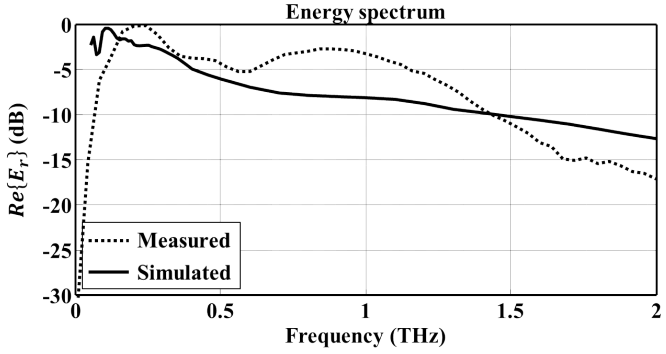

(c)

Figure 4.11: Comparison between the energy spectra, obtained by the measured pulses radiated by the PCA protoypes, and the simulated energy spectra radiated by the reflectors system evaluated by using the equivalent circuit: a) Auston-switch, b) bow-tie, and c) logarithmic spiral.

4.8 Conclusions

In this chapter, an electromagnetic model for the measurement of THz power radiated on a large bandwidth is proposed. The measurement system setup and the relevant coupling to the PCA radiated field is described in terms of its efficiency over the operative bandwidth.

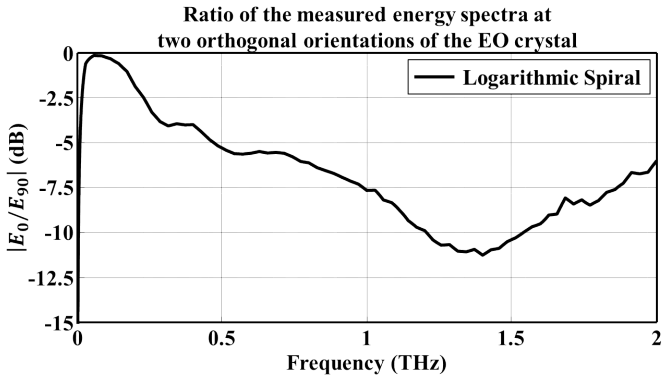

Figure 4.12: Ratio of two measured energy spectra amplitudes obtained by two orthogonal orientations of the EO crystal.

The measurements of the power radiated by three different PCA prototypes have been discussed. Such measurements have been compared against the power evaluated by using the proposed electromagnetic model. The results of the analysis have also been used to validate the equivalent circuit model introduced in Chapter 2.

The analysis shows clearly the different behaviours of the energy spectra radiated by the PCAs and coupled to the measurement system setup, thus giving a clear picture about the reasons of different values of power measured by the detector for different antenna geometries.

The values of power, evaluated by using the proposed electromagnetic model, find a good agreement with the values of the measured power. Furthermore, the comparison between the measured spectra and the estimated spectra are in fair agreement. Such results also provide a solid validation of the equivalent circuit model proposed in Chapter 2, which can be effectively used to design PCAs.

Acknowledgment

The author would like to thank SRON (Netherlands Institute for Space Research) for having provided its technical support for the assembly of the prototypes components.

Chapter 5

Logarithmic Spiral Antennas as Feed for Dense Dielectric Lenses

This chapter presents the performance of logarithmic spiral antennas as feeds of dense dielectric lens are investigated in detail. The performances are evaluated in terms of clean symmetric radiation patterns, high polarization purity, antenna efficiency and radiation dispersivity. A logarithmic spiral antenna placed in the dielectric-air interface can provide high aperture efficiencies over large bandwidths if coupled to a synthesized elliptical lens. The use of an air gap increases the directivity of the spiral radiation inside the dielectric allowing for lens directive patterns without sidelobes and reducing the dispersivity of the radiated pulse. The directivity enhancement of the fields inside the dielectric is validated by the measurement of a prototype. The highest frequency at which these antennas can be fed by a planar microstrip line is limited by the thickness of the microstrip substrate.

5.1 Introduction

Dielectric lenses fed by planar antennas have been proposed for many applications in the mm-, submm- wave systems [76, 95, 107–115]. In particular, planar frequency independent antennas are used as lens feeds to achieve wide band operation [76, 110–115], since they operating bandwidth is mainly limited by their size [116]. More specifically it has been pointed out that the self-complementary structures in free space ensure a constant impedance behavior [117].

In the presence of a dielectric lens, self-complementary antennas preserve their constant impedance behavior, but their radiation is different from the one in free space. Indeed they not longer act as self-complementary structures [118]. The difference is the additional leaky wave mechanism that characterizes the radiation of a planar antenna at the interfaces between air and dielectric [97, 98]. Therefore the geometries optimized for free-space radiation [119–124] cannot be directly scaled in order to be used as lens feeds. In this contribution, we focus on analyzing the radiation properties of logarithmic spiral in the presence of dielectric lenses. The designs are tuned to achieve an operative bandwidth

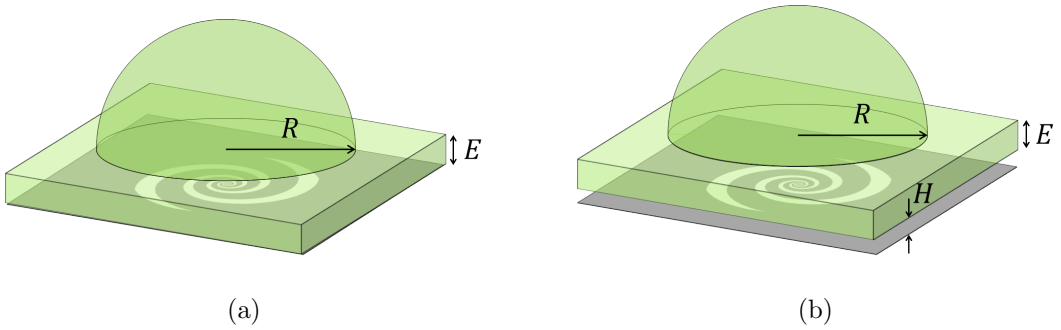

(a) (b)

Figure 5.1: Lens antennas: (a) spiral antenna with an elliptical lens for incoherent imaging system, and (b) the enhanced spiral antenna with an hyper-hemispherical lens for coherent imaging system.

(BW) of a decade when fed by an integrated feed. We also show the sharp degradation of the performances that effects such kind of antennas, when an embedded planar transmission line is used as feeding system, e.g. microstrip or coplanar waveguide.

There have been several works optimizing the dispersivity of spiral geometries in free space [123,124]. When a spiral antenna is used as a dense dielectric lens feed, its dispersivity will be affected. In this contribution, we show that by introducing a small gap between the spiral and the dielectric in the presence of an hyper-hemispherical lens, see Fig.5.1(b), the frequency dispersion of the spiral is not altered by the lens anymore. Indeed the dispersivity generated by the lens antenna is practically the same as the one introduced by the spiral geometry. The use of a small gap has been previously proposed in the presence of slot antennas leading to broadband non-dispersive operation [125, 126].

This Chapter is organized as follows. In Section 5.2, the analysis of the spiral antenna when radiating between two half-infinite dielectric media is discussed. In this case, the self-complementary structure does not provide the best performances because of the presence of the leaky wave phenomena. We also shown that the introduction of a small gap enhances the directivity of the fields radiated into the dense medium. In Section 5.3, the impact of planar feeding system on the performances of the antenna is discussed. Measurements from a prototype demonstrator of the enhanced spiral antenna feed are shown in Section 5.4, in order to prove the enhancement effect due to the presence of the air cavity between the bottom dielectricair interface of the lens and the antenna. In Section 5.5, the two proposed spirals are then coupled to a dielectric lens, the radiation performance and the dispersion of the pulse radiated by the lens fed by the two spiral feeds are shown and compared. Finally, Section 5.6 discusses some concluding remarks.

5.2 Logarithmic Spiral Antenna in Between Infinite Dielectrics

Spiral antennas radiating intro free space can achieve high quality omnidirectional patterns over large bandwidths [119–124]. However the radiated power is divided equally into the

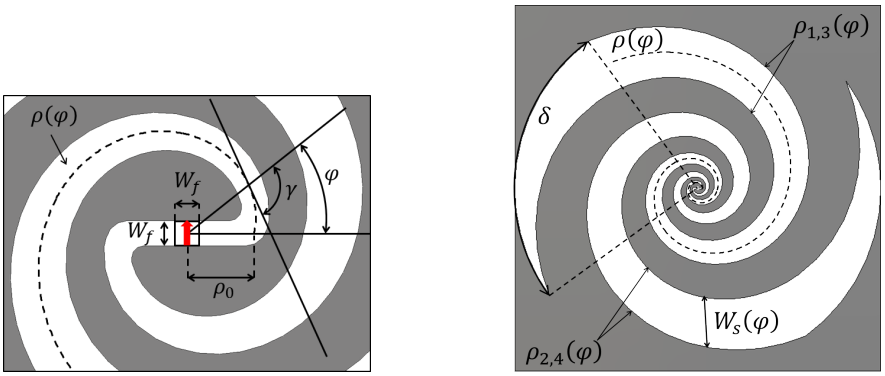

(a) (b)

Figure 5.2: Logarithmic spiral antenna: a) antenna geometry and b) design parameters.

upper and lower spaces. In order to improve the directionality of these antennas, one can resort to the use of a ground plane that limits the operational BW, or alternatively a dense dielectric that renders the system almost unidirectional. When a spiral antenna is placed at the air-dielectric interface, the structure is not more self-complementary [118]. The standard free space geometries cannot be simply scaled to match two different dielectric constants.

In order to design a two arms spiral antenna, each of the arms of the spiral has to be defined by means of two curves which represent the edges of each arm [119] as in Fig. 5.2(b). Three parameters are needed: the starting radius ρ_0, the curvature angle γ and the winding number N:

$$\text{Arm 1:} \qquad \rho_{1,3}(\varphi) = \rho_0 e^{a\left(\varphi_1 \pm \frac{\delta}{2}\right)} \tag{5.1a}$$

$$\text{Arm 2:} \qquad \rho_{2,4}(\varphi) = \rho_0 e^{a\left(\varphi_2 \pm \frac{\delta}{2} + \pi\right)} \tag{5.1b}$$

where $\varphi_1 \in [0, 2\pi N]$ and $\varphi_2 \in [-\pi, 2\pi\left(N - \frac{1}{2}\right)]$ and $a = 1/\gamma$; the two arms are identical and rotated of π one respect to each other; the parameter δ is the rotational angle between the two edges of each arm and it determines the tapering factor of the spiral arms. The length of the spiral arms in function of the rotational angle can be easily evaluated integrating the differential path along the spiral curve derived by equation of the locus of the spiral [119].

This section is dedicated to the analysis of the spiral placed at the interface between free space and an infinite dielectric half space. The dielectric half space simulates, to the first order, the effect of a dielectric lens on the planar antenna. The spiral geometry is aimed at achieving rotationally symmetric patterns with high circular polarization purity over a decade BW from 5 GHz to 50 GHz. Different logarithmic spirals have been simulated using CST simulations [94], radiating in an infinite dielectric medium with absorbing boundaries at the edge of the dielectric.

5.2.1 Spiral Radiation Between Two Homogenous Media

Initially the antenna is assumed to be printed at the interface between air and silicon, $\epsilon_{r1} = 1$ and $\epsilon_{r2} = 11.9$, respectively.

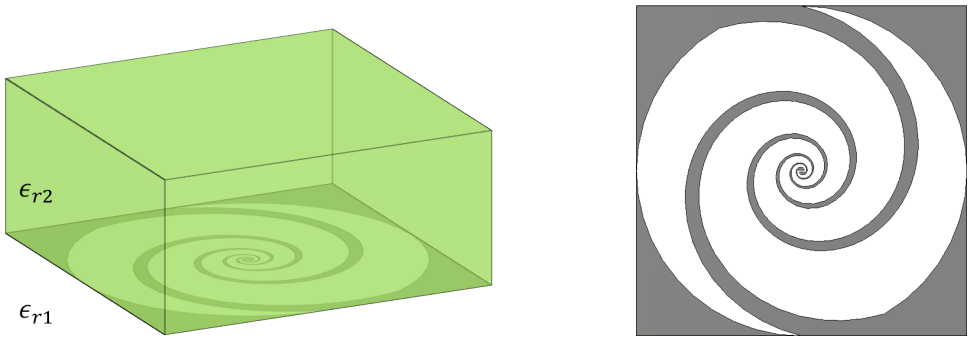

(a) (b)

Figure 5.3: Logarithmic spiral antenna between two homogeneous medium: a) regular structure and b) geometry of the spiral for the regular structure ($\rho_0 = 0.177\,\text{mm}$, $\delta = 150°$, $\gamma = 76.5°$ and $N = 2.6$ and $W_f = 0.059\,\text{mm}$).

When the spiral antenna is fed at its center as in Fig. 5.2(a), the characterizing (magnetic) current propagates along the arms at the interface between the two dielectric with a phase constant which is the roughly the average of the phase constants of the two medium:

$$\beta \approx \sqrt{\frac{\epsilon_{r1} + \epsilon_{r2}}{2}} k_0 = \epsilon_{eff} k_0 \tag{5.2}$$

where k_0 is the propagation constant in free space. Typically in the literature [112,113], ϵ_{eff} is used as scaling factor in order to scale the antenna geometries from the free space design to the half space design. While this approach is adequate for the basic dimensioning of the spiral (i.e. the maximum and minimum operating frequencies), the quality of the patterns obtained resorting only to this scaling is not optimal. In fact the effective propagation constant β results in a fast wave for the denser medium and a slow wave for the free space. Thus the radiation mechanism, occurring to the currents flowing at the interface between two different media, is heavily affected by the distributed leaky-wave radiation [97, 98]. In order to account for this effect, the tapering angle δ had to be varied to achieve the best possible quality of the radiation patterns inside the dielectric. The geometry of the best structure, we could come up with ($\gamma = 76.5°$, $\delta = 150°$), is shown in Fig. 5.3(b), which is significantly different that the self-complementary ($\delta = 90°$) in Fig. 5.2(b). Because of the increasing of the tapering angle of the slot arms, the ground plane between the arms is significantly reduced. In this case, the structure can be referred to as dipole spiral rather than as slotted spiral. In Fig. 5.4 are shown the widths of the beam at $-10\,\text{dB}$ for $\delta = 90°$ and for the geometry $\delta = 150°$. The self-complementary inspired geometry ($\delta = 90°$) does not provide the best symmetric pattern for spirals printed between two dielectrics. Because of the curvature angle is the same for both the structures, they present the same

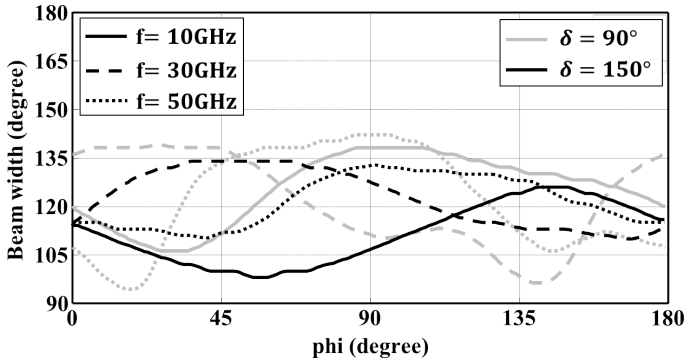

Figure 5.4: Width of the beams at −10 dB inside the dielectric of the regular structure for the self-complementary ($\delta = 90°$) and optimized structure ($\delta = 150°$).

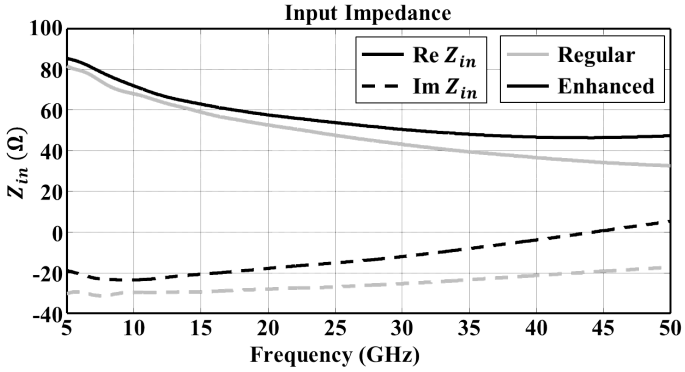

Figure 5.5: Input impedances of the regular spiral antenna discussed in Section 5.2.1 and the enhanced spiral antenna discussed in Section 5.2.2.

average width of the beams; but increasing the tapering of the arms the spiral radiates less elliptical patterns with an average variation of the width of 40° for $\delta = 90°$ to 24° for $\delta = 150°$. For the $\delta = 150°$ geometry, the Wobble of Wave (ratio between the maximum and the minimum of the field magnitude at costant elevation angle θ_0 [127]) at $\theta = 30°$ is 1.71 dB, 2.14 dB and 1.8 dB, respectively for 10 GHz, 30 GHz and 50 GHz. The input impedance of the antenna is shown in Fig. 5.5, such impedance provides a reflection coefficient below −10 dB for a reference impedance of 50 Ω. The normalized radiation patterns inside the dielectric are shown in Fig. 5.6. The radiated patterns are plotted as a Right-Handed Circular Polarization (RHCP) and Left-Handed Circular Polarization (LHCP). The circular polarization is calculated combining two linear polarization according to Ludwig's third definition [96]. The beams of the RHCP component show constant widths around 122° and the LHCP component is below −13 dB over the entire BW. The antenna provides a constant directivity over the entire decade BW as shown in Fig.5.7.

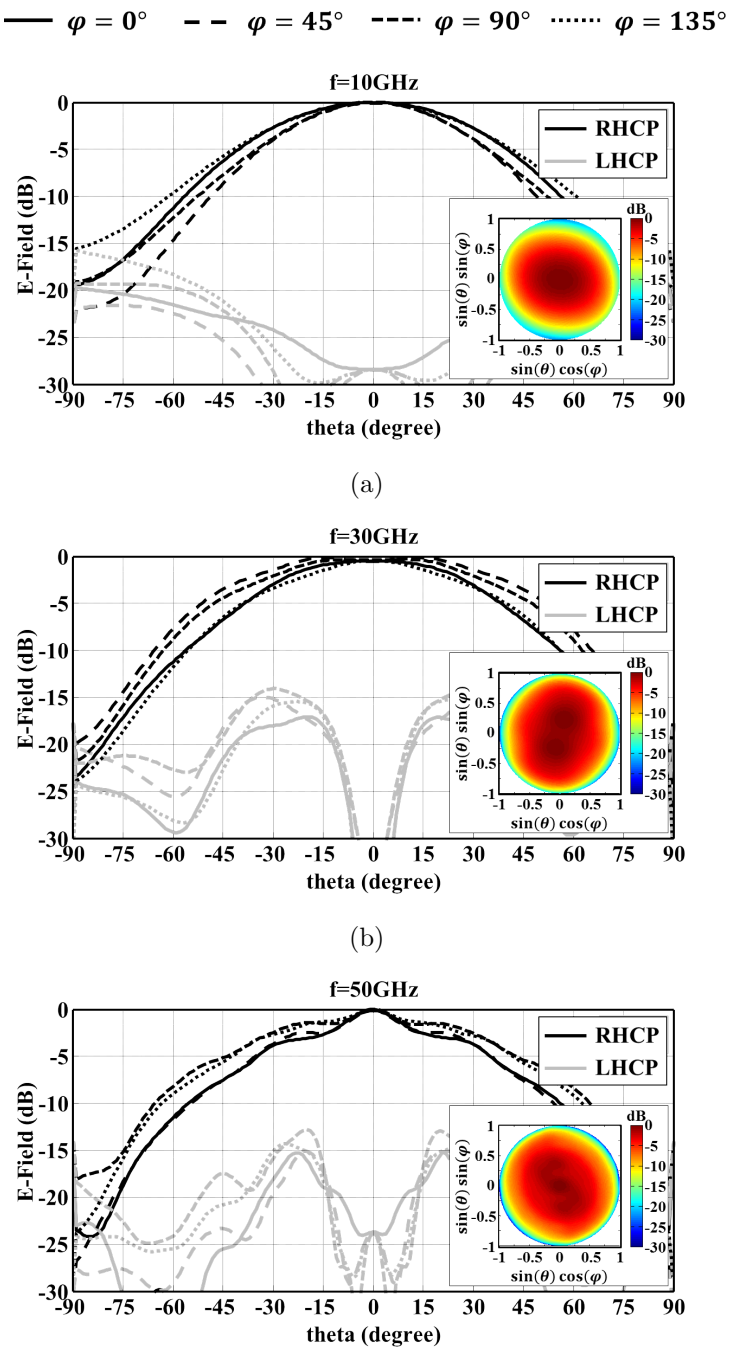

Figure 5.6: Simulated radiation patterns (primary fields) of the logarithmic spiral antenna ($\delta = 150°$) inside the dielectric on different φ planes at the frequencies a) 10 GHz, b) 30 GHz and c) 50 GHz. The insets show the 2D radiation patterns of the RHCP component.

For sake of comparison the proposed logarithmic spiral ($\gamma = 76.5°$, $\delta = 150°$) is compared with other frequency independent antennas available in the literature [112, 113].

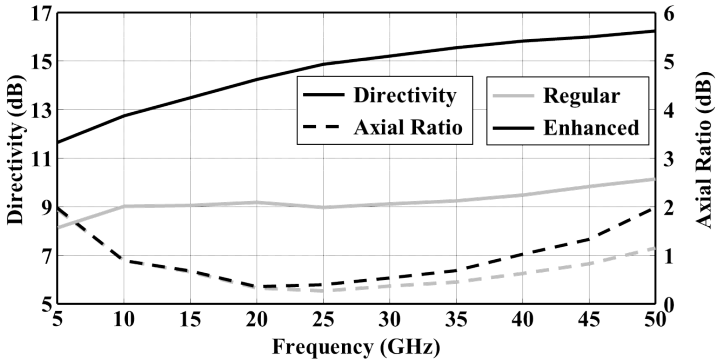

Figure 5.7: Simulated broadside directivity and axial ratio inside the dielectric of the regular and the enhanced structures.

Even if they are operating at different frequencies, the three structures have been designed for exciting a dense dielectric lens. It is worth noting that all the proposed frequency independent antennas have roughly the same directivity. However the proposed spiral presents the most symmetric patterns. Table 5.1 presents a detailed comparison of the simulated beamwidths at widely spaced frequency points.

Table 5.1: Proposed Antennas vs. State of the Art

	Beam width			
	5 GHz	20 GHz	35 GHz	50 GHz
Proposed Regular spiral	146°	122°	124°	121°
Enhanced spiral	96°	70°	57°	48°
	Beam width			
	6 GHz	12 GHz	18 GHz	24 GHz
Sinuous antenna in [112]	129°	130°	133°	125°
	Beam width			
	2.5 THz		4.3 THz	
Spiral antenna in [113]	125°		120°	

5.2.2 Enhanced Radiation

It is possible to increase the directivity of the patterns radiated by an antenna into a dense dielectric by introducing an electrically small air gap [125]. This implies that the spiral antenna should be printed on a small membrane at distance H from the lens itself. This structure will be indicated as the "enhanced" structure and it is shown in Fig. 5.8(a). The introduction of an air cavity between the dielectric interface and the antenna feed has been already proposed as solution to improve the illumination efficiency of linear polarized lens antenna feeds [54,125,126]. The presence of the small air gap, typically $H \leq \lambda_0/10$ with λ_0 at the highest frequency of operation, modifies the behavior of the leaky wave propagation which tends to the value in free space $\beta \approx k_0$. Moreover the enhanced structure supports an additional leaky mode localized in the cavity, which propagates orthogonally to the

radiating slot enhancing the rotational symmetry of the patterns [54]. Since the current

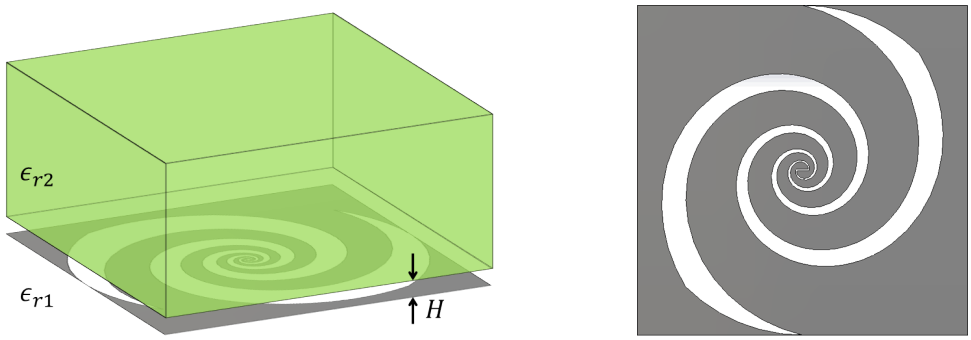

(a) (b)

Figure 5.8: Logarithmic spiral antenna between two homogeneous medium: a) enhanced structure with the introduction of an air gap and b) geometry of the spiral for the enhanced structure ($\rho_0 = 0.6\,\text{mm}$, $\delta = 45^\circ$, $\gamma = 76.5^\circ$ and $N = 2.6$ and $W_f = 0.15\,\text{mm}$). The height of the air cavity is $H = 0.4\,\text{mm}$.

propagates with the free space velocity, the dimensioning of the spiral is the same as that one in free space for the highest and lowest frequencies. The leaky wave distributed radiation can be controlled by appropriately tapering the spiral arms, setting the angles γ and δ, and the height H of the air cavity. This latter was set at $H = 0.4\,\text{mm}$ corresponding to $\lambda_0/15$ at the highest frequency. This ensures that the maximum loss due to front-to-back ratio over the entire BW from 5 GHz to 50 GHz is lower than 1 dB.

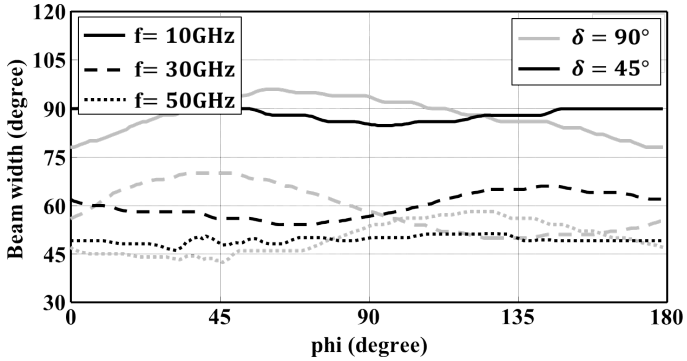

Figure 5.9: Width of the beams at $-10\,\text{dB}$ inside the dielectric of the enhanced structure for the self-complementary ($\delta = 90^\circ$) and optimized structure ($\delta = 45^\circ$).

The design includes a starting radius $\rho_0 = 0.6\,\text{mm}$ and the geometry of the optimum enhanced spiral is shown in Fig. 5.8(b). Even the designed enhanced structure ($\gamma = 76.5^\circ$, $\delta = 45^\circ$) is significantly different from the self-complementary structure. The behavior of the beam width in function of the frequency is also controlled by the height of the air cavity which dictates the increase of the directivity as function of the frequency.

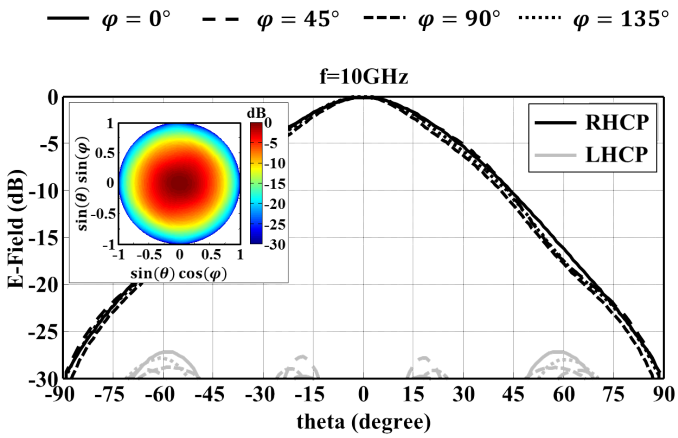

(a)

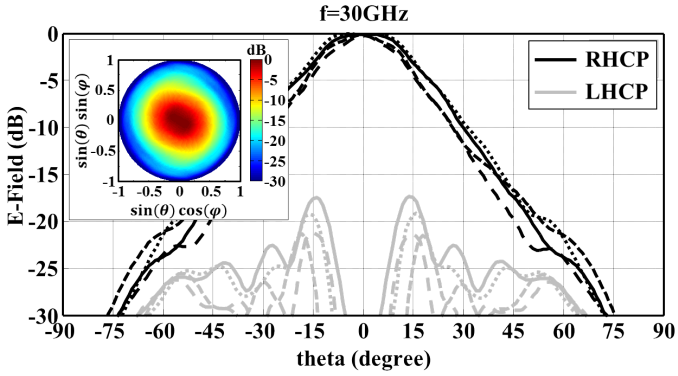

(b)

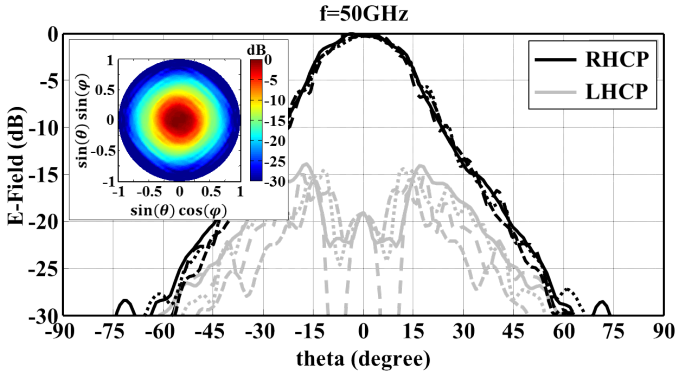

(c)

Figure 5.10: Simulated radiation patterns (primary fields) of the enhanced logarithmic spiral antenna ($\delta = 45^{\circ}$) inside the dielectric on different φ planes at the frequencies a) 10 GHz, b) 30 GHz and c) 50 GHz. The insets show the 2D radiation patterns of the RHCP component.

The symmetry of the radiation patterns is controlled by both the tapering angle δ and the cavity height H; reducing the tapering of the arms the ellipticity of the beams

decreases. Fig. 5.9 shows the beam widths at $-10\,\mathrm{dB}$ of the enhanced structure with the tapering angle $\delta = 90°$ and the tapering angle $\delta = 45°$.

The input impedance of the antenna is shown in Fig. 5.5, such impedance provides a reflection coefficient below $-14\,\mathrm{dB}$ for a reference impedance of $65\,\Omega$. The beams of the RHCP component are symmetric with a range of the variation, as a function of the azimuth angle, of the beam at $-10\,\mathrm{dB}$ from 12°, for the lowest frequency, to 1° for the highest. The beam width decreases in a range from 96° to 48° as the frequency increase. The normalized radiation patterns into the dielectric radiate by the proposed enhanced spiral antenna are shown in Fig. 5.10. The actual width of the beam also decreases as the frequency increases resulting in higher directivity as it shown in Fig.5.7. The LHCP component of the field is below $-13\,\mathrm{dB}$ over the entire frequency range.

5.3 Planar Feeding System

The performances of the spiral antennas, shown in sections 5.2.1 and 5.2.2, can be obtained only when the antenna transmitter/receiver is integrated at the center of the spiral. In order to send out/read a high frequency signal, the solutions proposed in the past were a coaxial cable embedded on the ground plane of the spiral [119], a differential feed using two coaxial cables orthogonally connected to the center of the antenna [114] or a microstrip [128, 129]. Only this last option is suited for mm-wave [130, 131], submm wave [132, 133] integrated systems. However also microstrip feedings present challenges, in [128, 129] it is indicated that the ratio between the width of the ground plane and the microstrip has to be at least 10 in order to avoid the influence of the transmission line on the performances of the spiral. According to such rule, for the enhanced spiral presented in the previous section, the height of the substrate should be smaller than $\lambda_0/210$, at the highest frequency. For the case of the regular spiral printed on a dense dielectric, Sec. 5.2.1, it is needed a substrate of $\lambda_0/2100$, since the smallest ground plane dimension in between the spiral arms is 10 times smaller than the enhanced spiral. This dimension is comparable to the one used in [130, 131]. Moreover the regular spiral presents a lower input impedance than the enhanced one, which involves to use a substrate even smaller in order to obtain the desired matching at the feeding point.

Despite the fact that these problems cannot be solved with current Printed Circuit Board (PCB) technology. A microstrip feed has been designed with the purpose to build a prototype. Only the enhanced spiral of section 5.2.2 is considered due to the lower requirements on the microstrip substrate.The microstrip with a spiral profile is placed on a substrate attached at the bottom interface of the metallic plane where the slot spiral is etched as it shown in Fig. 5.11. The end of the microstrip is connected to the ground plane by a short-circuit pin. The smallest available thickness of the substrate (Rogers RT/Duroid 6002, $\epsilon_r = 2.94$) has been used $H_m = 0.127\,\mathrm{mm}$, in order to design a matched microstrip with the smallest width possible $W_m = 0.2\,\mathrm{mm}$. Note that the height of the substrate and the microstrip width should have been smaller than $H_m = 0.028\,\mathrm{mm}$ and $W_m = 0.044\,\mathrm{mm}$ respectively to avoid the deterioration of the performance.

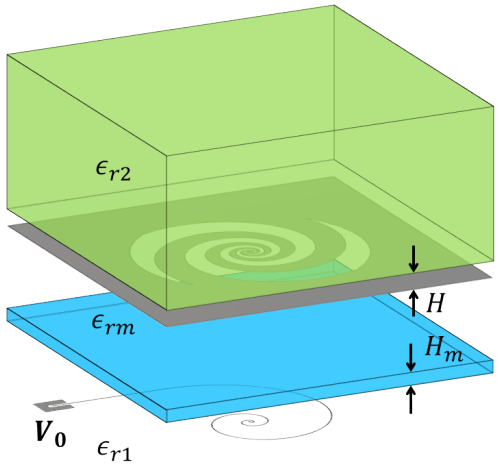

Figure 5.11: Microstrip planar feeding system of the spiral antenna.

Since the ratio between the ground plane, in the inner part of the spiral, and the width of such microstrip is smaller than the one indicates in [128, 129], the microstrip feed introduces an imbalance in the structure. The micrsotrip itself radiates, resulting in tilted beams and asymmetric radiation patterns as is shown in Fig. 5.12. This effect is more relevant as the frequency increases because the radiation at higher frequencies occur in the inner part of the spiral where the ground plane is smaller, due to the tapered profile of the structure. Those effects are quantified in Fig. 5.13, the directivity at broadside is reduced and it starts decaying at the higher frequencies. Moreover the axial ratio is increased, affecting the circular polarization purity, resulting in a substantial reduction of the effective antenna bandwidth.

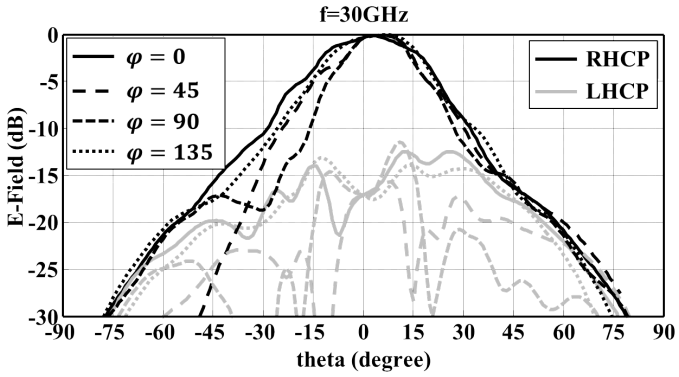

Figure 5.12: Simulated radiation patterns of the enhanced logarithmic spiral antenna ($\delta = 45°$) fed by microstrip on different φ planes at the frequency 30 GHz.

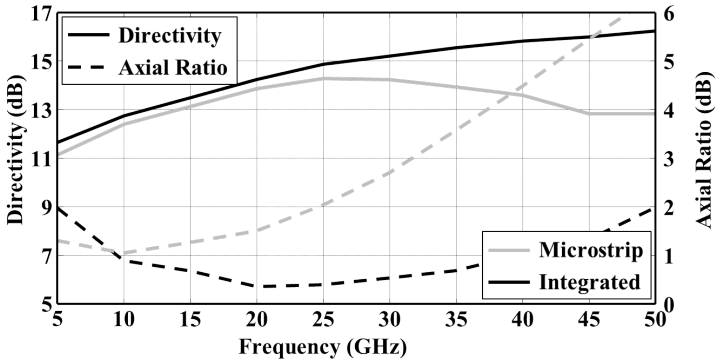

Figure 5.13: Comparison of the simulated directivity and axial ratio at broadside direction between the enhanced spiral fed by the intgrated feed and microstrip.

5.4 Prototype Measurements

Despite the expectation of poor radiation performance due to the microstrip feeding, which can be improved when the antenna is realized with Integrated Circuit technology, typically used for high frequency applications [130, 131], a prototype demonstrator of the enhanced spiral has been manufactured in PCB technology. The main purpose of the prototype is to demonstrate the increase of the directivity, that can be achieved by introducing an air gap. The prototype combines the enhanced spiral antenna, a micro-strip based feeding and the use of an already available dielectric lens.

The prototype of the spiral is shown in Fig. 5.14(a)–5.14(b) and the entire layered structure is shown in Fig. 5.14(c). The slot spiral is etched on the ground plane of a dielectric slab (Rogers RT/Duroid 6002, $\epsilon_r = 2.94$) of height $H_m = 0.127\,\text{mm}$. The same dielectric slab is used as substrate for the microstrip line as is depicted in Fig. 5.14(c). The feeding line includes a transformer to match the line coupled with the spiral ($Z_0 = 70\,\Omega$) with the one that arrives to the connector ($Z_0 = 50\,\Omega$). The air gap is realized by a grid structure of height $H_{gap} = 0.4\,\text{mm}$ composed by a ceramic material (Rogers RT/Duroid 4003, $\epsilon_{rm} = 3.55$). The grid structure is designed to emulate the air cavity ($\epsilon_{gap} = 1$) and to ensure the mechanical stability of the structure. Lastly, to make the structure more stiff, the grid is attached to a thick slab of dielectric of height $H_{slab} = 3.2\,\text{mm}$, which will be part of the extension length for the hemispherical lens. The material of the stiffening slab is the same which composes the lens (ECCOSTOCK HIK 500F, $\epsilon_{r2} = 11.9$). The realization of the air gap does not present any particular problem for microwaves and mm wave applications and it can be easily realized using the procedure shown above. Difficulties arise at submm wave applications. Guaranteeing the designed thickness of the gap is critical and different dedicated process depending on the technological boundaries have to be adopted [134].

The spiral geometry of the prototype is slightly different respect to the structure presented in section 5.2.2. The starting radius has been enlarged in order to accommodate the

microstrip, $\rho_0 = 0.75\,\text{mm}$. The tapering angle has been increased from $\delta = 45^\circ$ to $\delta = 58^\circ$. The curvature angle is $\gamma = 76.5^\circ$ and the number of windings is $N = 2.75$.

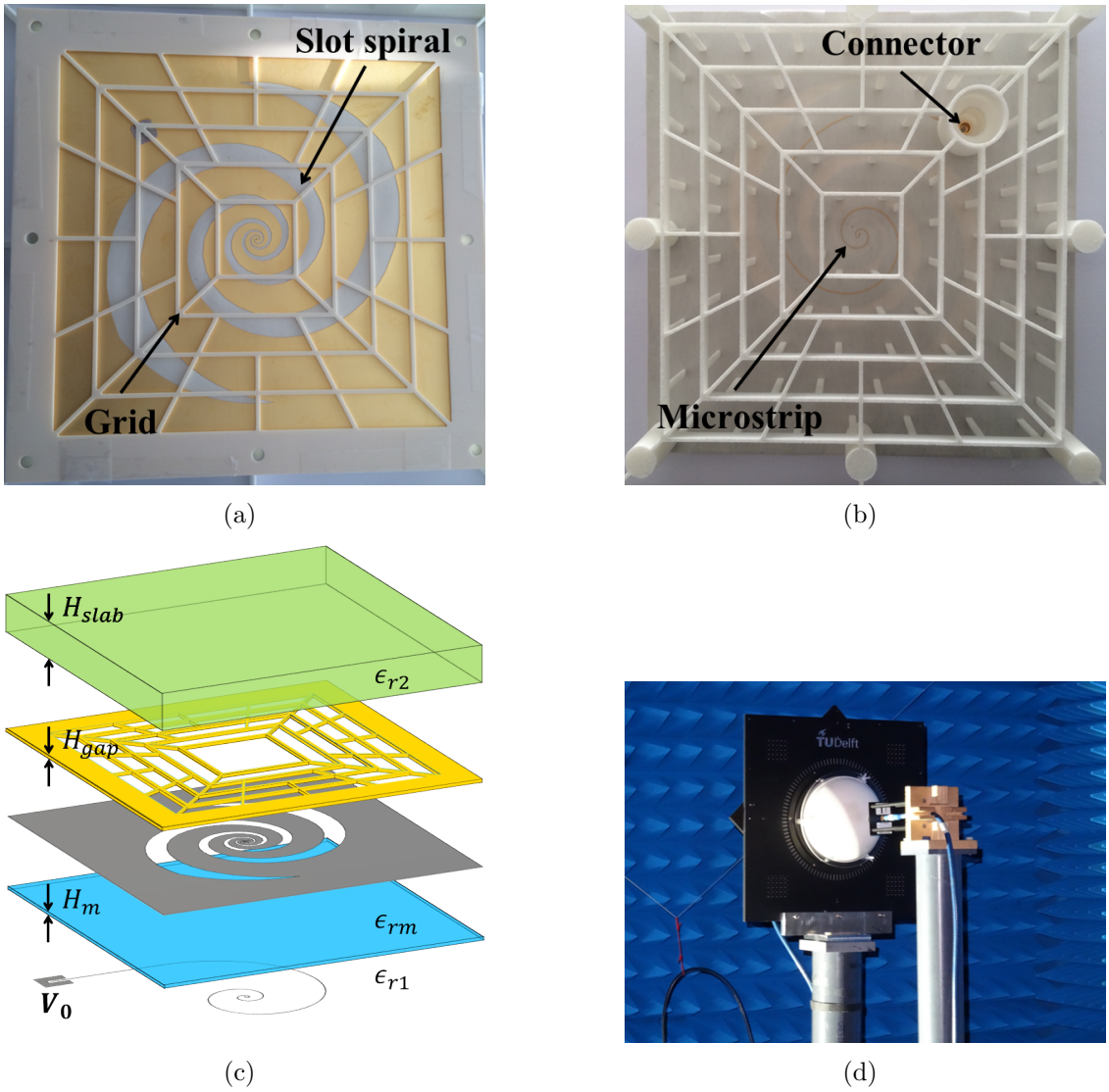

Figure 5.14: Prototype of the enhanced spiral antenna and Measurement setup: a) top view without the dielectric slab, b) bottom view and c) layered structure and d) Measurement setup.

The measurements setup is shown in Fig. 5.14(d). In order to measure the patterns inside the lens, the spiral lens feed is placed at the bottom interface of the lens without the extension length and the probe is scanned along the lens surface. Eliminating the multiple reflections of the dielectric-air interface by means of time gating has been possible to evaluate the radiation patterns inside the lens as if the antenna is placed in a half semi-infinite dielectric. The broadband probe used for the measurements has a bandwidth from 7 GHz to 26 GHz.

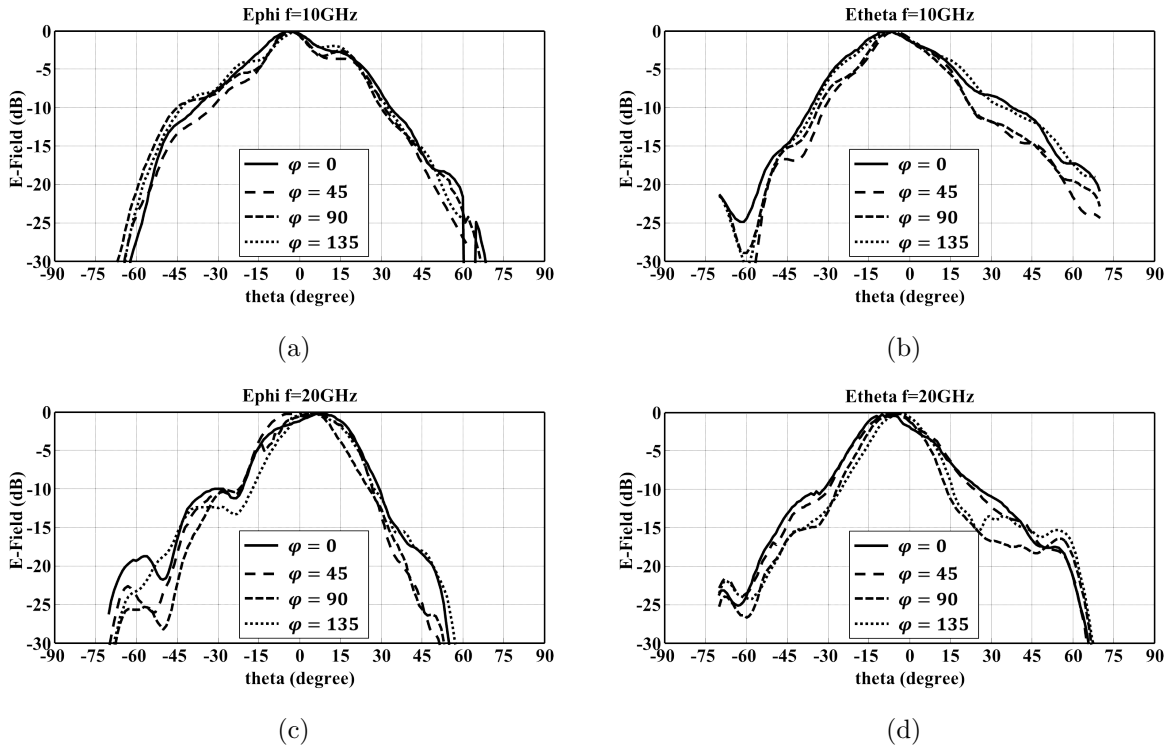

Figure 5.15: Measured radiation patterns of the two spherical components inside the lens of the enhanced spiral prototype on different φ planes at the frequencies a), b) 10 GHz and c) d) 20 GHz; a) c) show the φ component, while b), d) show the θ component.

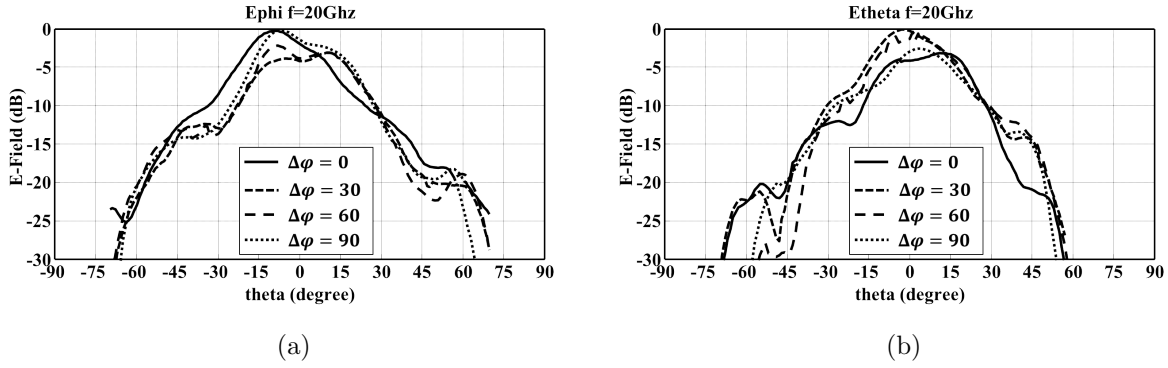

Figure 5.16: Measured radiation patterns inside the lens of the enhanced spiral prototype on the plane $\varphi = 0^\circ$ at the frequency 20 GHz and at different rotation angles of the lens respect to the antenna feed; a) shows the φ component, while b) shows the θ component.

The measured radiation patterns of the two linear polarizations are shown in Fig. 5.15 for different planes. The patterns are far less symmetric than one could have anticipated looking at the simulations from section 5.3. The reason is in the anisotropic behavior of the material of the dielectric lens [135]. To show the anisotropy, the radiation patterns

in the $\varphi = 0^\circ$ plane of the the antenna has been measured for different rotation angles of the lens. The lens has been rotated four times with an angle step $\Delta\varphi = 30^\circ$ and the measurements show significant changes with each rotation of the lens as it is shown in Fig. 5.16. Because of this anisotropy, it is not possible to combine the linear polarizations in order to obtain the field in circular polarization inside the lens. Such undesired behavior of the dielectric lens can be avoided using silicon lenses [112], which have an isotropic behavior, and typically used in millimeter and submillimeter wave applications [76, 110, 111], [113] and [130, 131]. Despite these problems, the patterns are still enlightening as they show beamwidths measured (taken as the value at $-10\,\mathrm{dB}$). The measured beamwidths vary from 75° to 55° against an expected beamwidths varying from 90° to 60°. The expected beamwidths of the regular spiral were in the order of 120°. This proves the dominance of the enhanced leaky wave mechanism, which is the main contribution of this paper.

5.5 Lens Radiation Performance

In this section, a comparison between the simulated performance of the regular and the enhanced spiral as feed of dense dielectric lenses are shown. The approach used for the characterization of the antenna is the same used in [54]. The simulated radiation patterns in an infinite dielectric, shown in Sec. 5.2, are used to compute the fields radiated by the lens via a Physical Optics (PO) approach, [30, 136], without using any kind of correction of the PO currents by means of a transition function as proposed in [137], contributions associated with creeping waves [138] and the diffraction mechanisms induced by the lens truncation at the ground plane. In this approach the reflections at the lens interface is only included as a loss term in the gain and not in the evaluation of the shape of the lens radiation patterns. A silicon lens of diameter $D = 120\,\mathrm{mm}$, which corresponds to $20\lambda_0$ at $50\,\mathrm{GHz}$, is chosen as a reference.

5.5.1 Radiation Patterns

The performance of a dense dielectric lens fed by the spiral antennas proposed in Sec. 5.2 are summarized in Fig. 5.17. The low frequency variation of the patterns of the regular spiral, Fig. 5.7, implies the possibility to achieve high aperture efficiency over a large bandwidth by using a synthesized elliptical lens ($E = 0.39R$). The simulated gain for this case increases nearly quadratically with the frequency as expected. The aperture efficiency is between 45%–55% on the entire bandwidth, only limited by the reflection losses, since no matching layers are assumed. Instead the gain of the synthesized elliptical lens fed by the enhanced spiral presents a lower frequency variation since a smaller portion of the lens is illuminated by the feed at high frequencies, but the patterns present nearly no sidelobes as shown in Fig. 5.18. The use of a regular spiral for low extension heights involves a significant decrease of the directivity at higher frequencies, due to the phase error on the currents at the lateral part of the lens [54]. Indeed Fig. 5.17 shows such variation when the regular spiral is used with an extended hemispherical lens with $E = 0.3R$. Instead when the

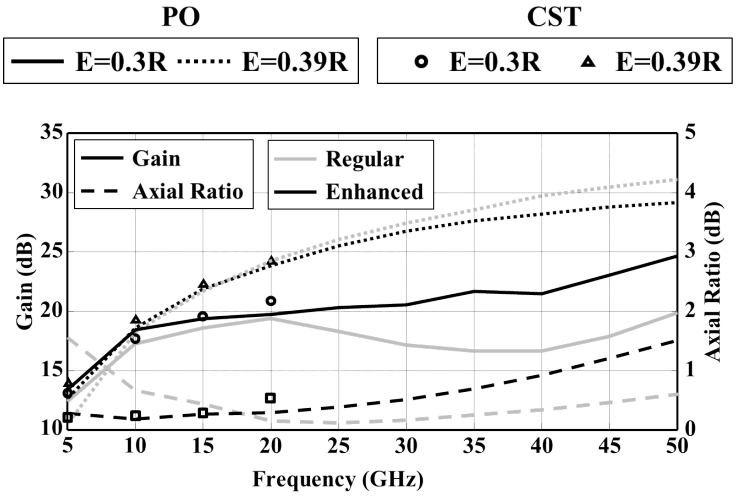

Figure 5.17: Simulated broadside gain and axial ratio of the secondary fields for the regular and the enhanced structures using the hyper-hyperhemispherical and the elliptical extension. The gain takes into account of losses due to matching, reflection, polarization and front-to-back ratio.

enhanced spiral is used as feed of such lens, Fig. 5.17 shows that the directivity increases linearly with the frequency. The use of an air gap allows to achieve clean radiated patterns for such low extension heights over the entire bandwidth, as shown Fig. 5.19, thanks to the enhanced directivity in the fields inside the dielectric.
In order to provide a further validation of the results shown in this section, a comparison of the performance of the enhanced spiral lens antenna evaluated by the PO approach and by CST simulations is provided. Both the hyper-hemispherical and the elliptical extensions have been simulated using the Time-Domain solver of CST, without taking into account the effect of multiple reflections inside the lens. The simulations have been feasible only at the lower frequencies of the frequency band of interest, because of the heavy computational burden. A good agreement of the results between the PO method and the CST simulations has been observed as shown in Fig. 5.17. For sake of space only the comparison of the radiation patterns at 10 GHz is shown for the elliptical and the hyper-hemispherical extensions, respectively in Fig. 5.18(a) and Fig. 5.19(a). A general fair agreement of the radiation patterns has been observed for both cases and for all the frequencies investigated. A discrepancy of the radiation patterns is more relevant only at the lowest frequency because of low accuracy of the PO approximation when the lens is small in terms of the wavelength.

5.5.2 Pulse Distortion

The dispersion behavior of the proposed spiral antennas can also be of interest. One of the authors in the past has already shown the absence of dispersion of the radiated pulse by the linear leaky slot antenna in combination with a dense dielectric lens with low extension height [125]. Indeed lower extension heights lenses lead to lower directivity variation versus

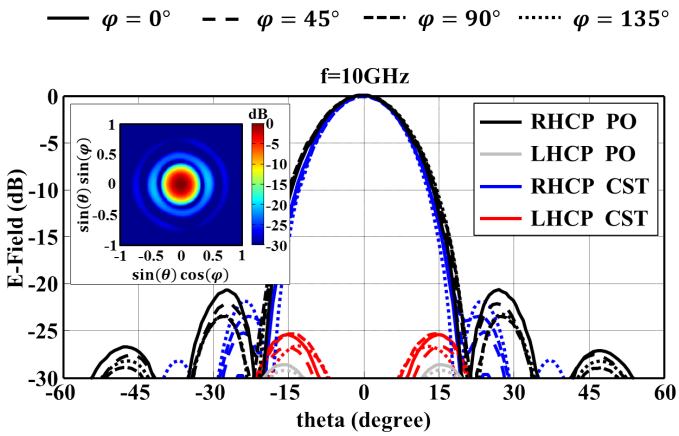

(a)

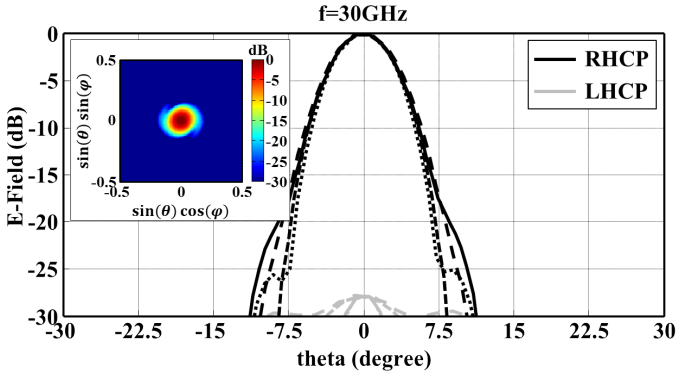

(b)

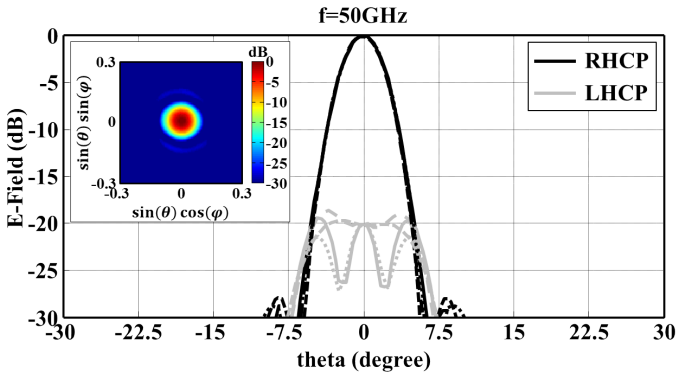

(c)

Figure 5.18: Simulated radiation patterns outside the lens (secondary fields) illuminated by the enhanced spiral antenna feed at the elliptical point on different φ planes at the frequencies a) 10 GHz, b) 30 GHz and c) 50 GHz. The insets show the 2D radiation patterns of the RHCP component evaluated with the PO approach.

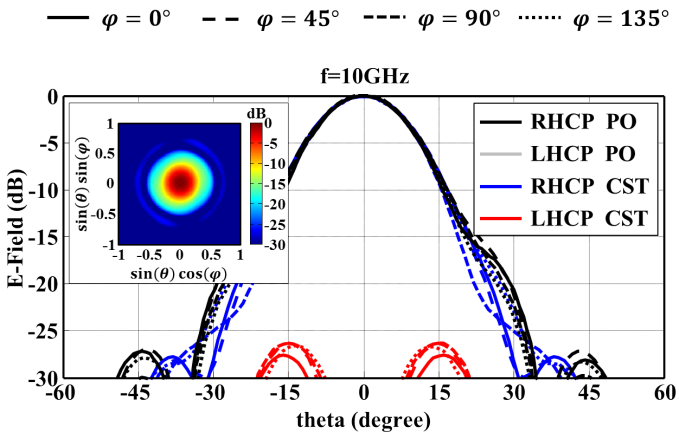

(a)

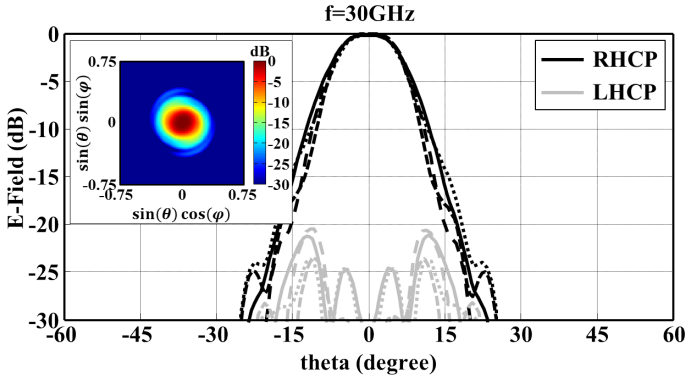

(b)

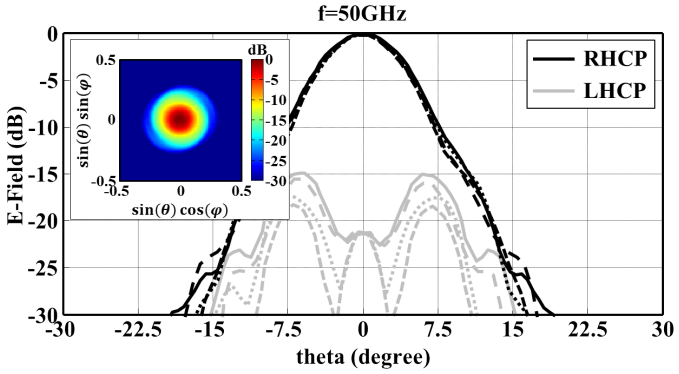

(c)

Figure 5.19: Simulated radiation patterns outside the lens (secondary fields) illuminated by the enhanced spiral antenna feed at the hyperhemispherical point on different φ planes at the frequencies a) 10 GHz, b) 30 GHz and c) 50 GHz. The insets show the 2D radiation patterns of the RHCP component evaluated with the PO approach.

frequency.

Fig. 5.20(a) and 5.20(b) show the input pulse and the pulse of the electric field (RHCP component) radiated at broadside in the infinite dielectric and outside the $0.3R$ lens by the regular spiral and the enhanced spiral. In general spiral antennas are known to be dispersive in frequency, due to the fact that the radiation is emitted from different sections of the spiral at different frequencies. There have been authors showing that this dispersion can be reduced by a proper modification of the spiral geometry [114, 123]. A different phenomena drives the dispersion in lenses. For the regular spiral case, the pulse radiated inside the dielectric is already significant distorted compared with the input signal. Even more dispersed is the pulse radiated outside the lens. In comparison the enhanced spiral preserves more the input pulse shape, both for the patterns inside and outside the lens. Indeed the lens does not introduce any additional dispersion. This can be attributed to the fact that the direction of the leaky wave is closer to broadside when an air gap is introduced [125].

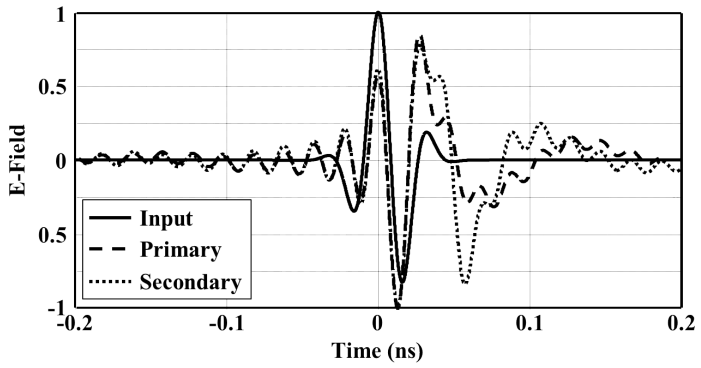

(a)

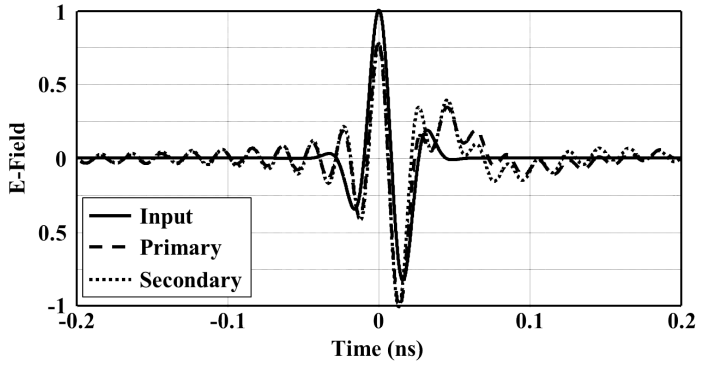

(b)

Figure 5.20: Input pulse and primary and secondary simulated electric fields (RHCP component) in time domain at broadside radiated by a dense lens with an extension length $E = 0.3R$, fed by a) the regular spiral and b) the enhanced spiral.

5.6 Conclusions

In this chapter the radiation properties of spiral antennas in the presence of dielectric lenses has been investigated. It has been found that one cannot simply scale the optimal self-complementary geometry typically used for free space. More specifically the design of a spiral printed between the dielectric and air interface and coupled to a synthesized elliptical lens has been proposed to achieve high aperture efficiency over broad bandwidths. However the use of a planar feeding line for this design is only possible if extremely thin substrates are used ($\lambda/2000$) without limiting the bandwidth. Introducing a small air gap between the spiral antenna and the bottom part of the lens allows for decreasing this limitation to $\lambda/200$ and achieving directive patterns without sidelobes for a broadband.

The use of a low extension height hemispherical lens with a spiral kept at small distance from the dielectric is suggested when the main goal of the design is the low frequency dispersivity. A pulse radiated by such antenna presents significantly lower dispersivity than the one radiated by the same lens when fed with a spiral printed directly on the dielectric interface. That is because the leaky wave radiation associated slots or dipoles printed at the dielectric air interface points towards large angles, while a spiral antenna points towards broadside. Instead when the gap is introduced the leaky wave radiation points at direction closer to broadside. This directivity enhancement achieved inside the dielectric has been validated by measurements of a prototype.

Chapter 6

Novel Photoconductive Antenna Array

A novel design of a optically pumped THz photoconductive source in array configuration is presented in this chapter. The proposed solution is based on the exploitation of the ultrawide band properties of connected antenna arrays. The photoconductive elements of the array are excited by an array of microlenses which splits and focuses the laser beam onto the active areas of the connected array. An ad-hoc bias network is introduced in order to properly bias the active portion of the array elements. If needed the array can be used to illuminate an extended hemispherical dielectric lens, which collimates the radiated THz electromagnetic field in the boresight direction. The proposed solution allows to achieve a high radiated power on a large bandwidth up to the terahertz frequencies when the photoconductive material is illuminated by a laser operating in the pulsed mode. The proposed solution is therefore suitable and effective to be employed in terahertz time-domain systems. Moreover, it is suited to support a wide frequency reconfigurability, in the laser continuous wave mode.

6.1 Introduction

In order to increase the available THz power and, at the same time, to avoid the thermal failure, various PCA array structures, based on different technical solutions, have been proposed and developed in the recent years [52, 62, 64, 66, 68–70, 74, 139–142]. In an efficient photoconductive array structure, each element should be operated at the maximum bias field and the maximum optical laser intensity allowed before thermal breakdown. Moreover a large number of elements could be used to obtain high THz power by means of coherent superposition of the different photoconductive sources. Finally, a desired far-field beam pattern can be obtained and steered by changing the phase distribution of the photocurrents in the array elements.

Unfortunately, to date all photoconductive array solutions present in literature are intrinsically narrow band or extremely inefficient. Therefore, they are not suitable to

couple and radiate the wideband signal generated in each of the photoconductive gaps, when these are illuminated by laser beams in the PW mode. Nor they are suited to support a wide frequency reconfigurability, typically desired for the optical pumping in the CW mode.

A novel array solution based on the connected array concept [24–30], which is intrinsically wideband, is presented in this chapter. It is therefore suitable to efficiently radiate the signal generated in the photoconductive gaps and to efficiently receive wideband THz signals.

This chapter is structured as follows: Section 6.2 is devoted to summarize different solutions present in the literature; Section 6.3 discusses why the existing solutions are not suitable for radiating a signal on a large bandwidth; Section 6.4 two biasing network for feeding the connected array of slots and dipoles are introduced, and the various geometrical, electrical, and optical aspects involved in the proposed solution are discussed. Section 6.5 presents a numerical result, based on a theoretical model presented in Chapter 2. Finally, Section 6.6 concludes with some expectations of the proposed design of the photoconductive connected array.

6.2 Photoconductive Array: State of the Art

In this section, different photoconductive antenna array solutions present in the literature highlighting their relevant aspects that characterize them are briefly discussed.

As anticipated, a photoconductive antenna is an optoelectronic device which is used to radiate and receive electromagnetic power in the THz frequency bandwidth. It is typically obtained by placing thin metallizations on a slab of photoconducting material which is illuminated by a laser beam. The most frequently used PCA solutions are the Auston switch, the bow-tie antenna, and the spiral antenna, [1,2,4,31], shown in Fig. 6.1(a)-6.1(b)-6.1(c). In order to increase the coupling between the antenna and the photoconductive material, interdigited electrodes at the antenna terminals had also been used [76], see Fig. 6.2(a). In Fig. 6.2(b) it is shown an enlargement of the antenna terminals and the relevant interdigitated structure. The yellow arrows represent the photo-induced dipoles, whereas the cyan lines and arrows represent the currents flowing on the antenna electrodes. An array of photoconductive antennas is obtained by arranging together a certain number of PCAs, properly biased by a voltage source.

A first possible array solution is that proposed in [62,64] shown in Fig. 6.3. Essentially, the authors used an interdigited electrode structure over a large photoconductive area. Such solution was conceptually important since, distributing the interdigited electrodes on a large area, the structure effectively realized an array of dipoles (oriented along the yellow arrows in Fig. 6.3(b). However, when the interdigited fingers of the electrodes are biased, the electric field direction between successive fingers is opposite. When the laser spot illuminates the area, the biasing-induced dipoles between two consecutive fingers have opposite orientations, see Fig. 6.2(b). Consequently, the fields radiated by opposite dipoles cancel each other in the array antenna far-field region. In order to avoid such a

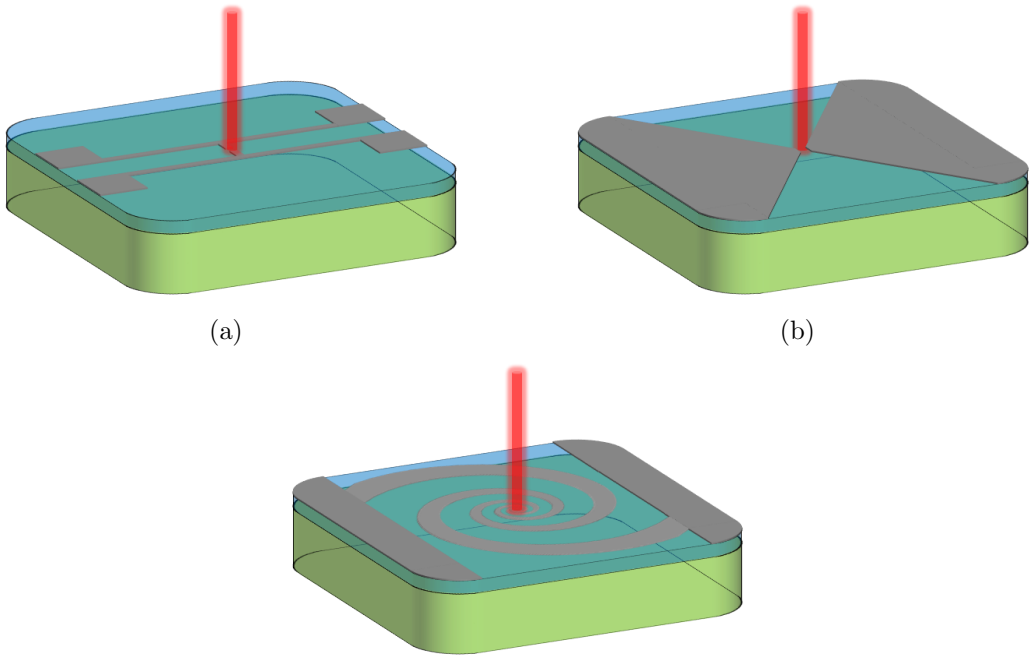

(a) (b) (c)

Figure 6.1: Antenna geometries for photoconductive antennas: a) Auston-switch antenna, b) bow-tie antenna, c) logarithmic spiral antenna.

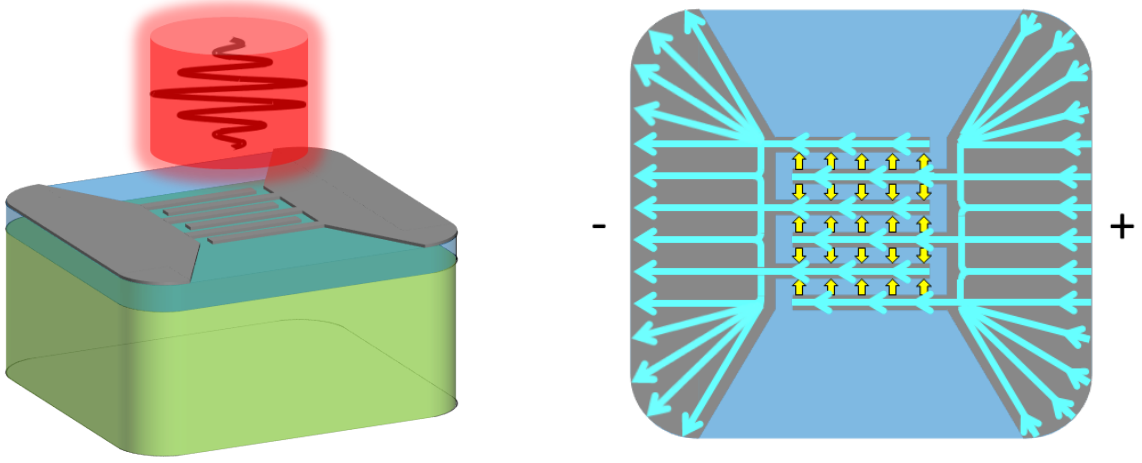

(a) (b)

Figure 6.2: PCA terminal interdigited electrodes. a) interdigitated photoconductive gap. b) The current flowing through the interdigitated photoconductive gap. The yellow arrows represent the photo-induced dipoles, whereas the cyan lines and arrows represent the currents flowing on the antenna electrodes.

destructive interference, a second metallization (mask), which is electrically insulated from that of the electrodes, is used as it shown in Fig. 6.3. This prevents the excitation of the

photoconductive material between two consecutive fingers and leads to a distribution of dipoles which are oriented in the same direction on all the array surface.

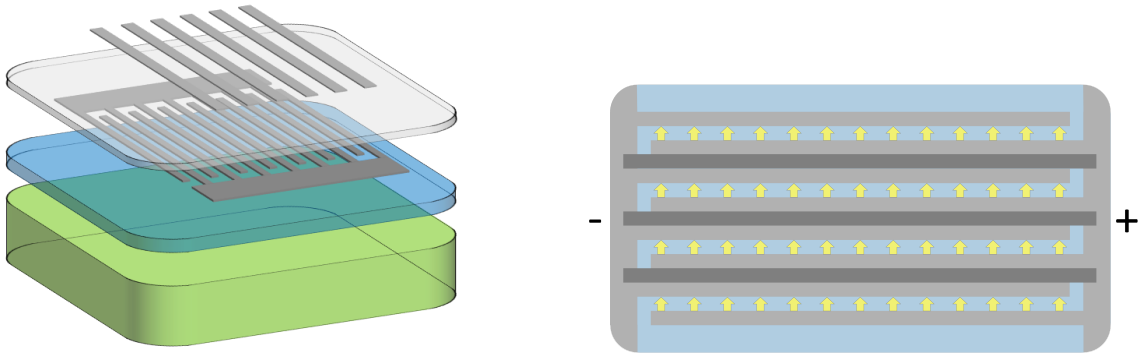

(a) (b)

Figure 6.3: PCA interdigitated array in [62, 64]. a) 3D layers structure exploded view drawing; b) 2D top view of the structure. The yellow arrows represent the orientation of the excited dipoles inside the photoconductor material.

With the aim of obtaining all the excited dipoles in the photoconductor oriented in the same direction, in [66,69,70] the authors suggested another technological solution. Instead of masking the area between two consecutive biasing metallizations, they proposed to etch away the photoconductive material in such regions, see Fig. 6.4.

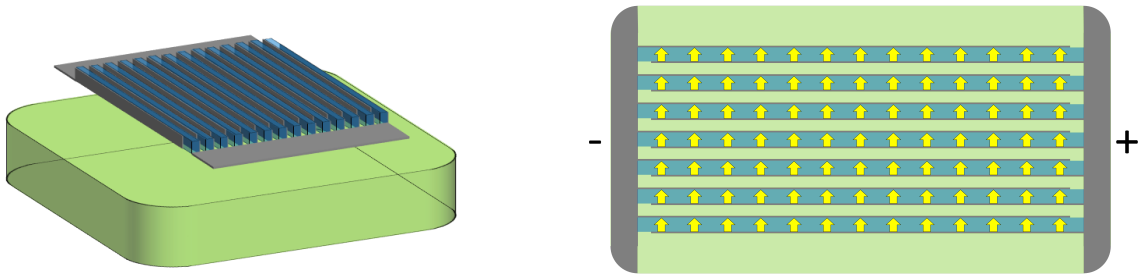

(a) (b)

Figure 6.4: PCA etched array in [66,69,70]. a) 3D layers structure exploded view drawing; b) 2D top view of the structure. The yellow arrows represent the orientation of the excited dipoles inside the photoconductor material.

Both the solutions described before have the drawback that not all the optical power is used in exciting the photoconductive array. Indeed, part is reflected by the masking metallizations or it does not excite free charges in the regions where the photoconductor is removed. To overcome such a problem, in [68] the authors proposed an alternative approach. In detail, they used a large interdigited structure, which is coupled to the laser optical power through an array of microlenses as in Fig. 6.5. The lenses are positioned in such a way that only alternate gaps between the biasing fingers are illuminated by the incident optical beam. As a consequence, all the laser power is used for exciting

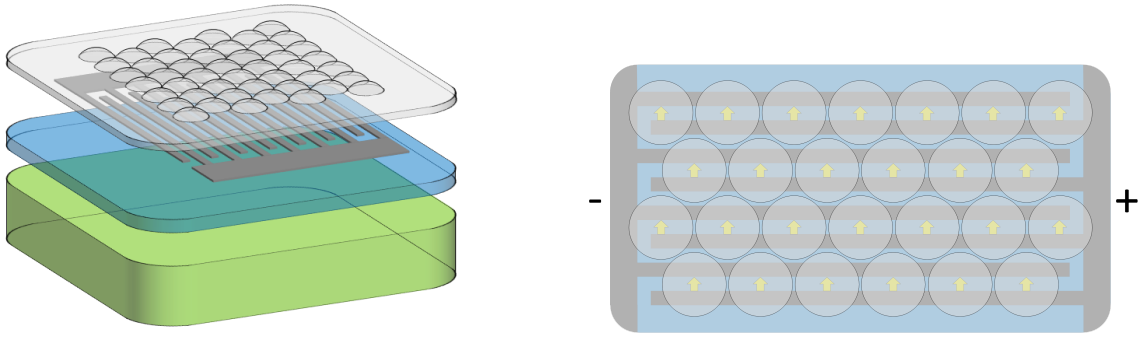

(a) (b)

Figure 6.5: array in [68]. Interdigited array structure and array of microlenses. a) 3D layers structure exploded view drawing; b) 2D top view of the structure. The yellow arrows represent the orientation of the excited dipoles inside the photoconductor material.

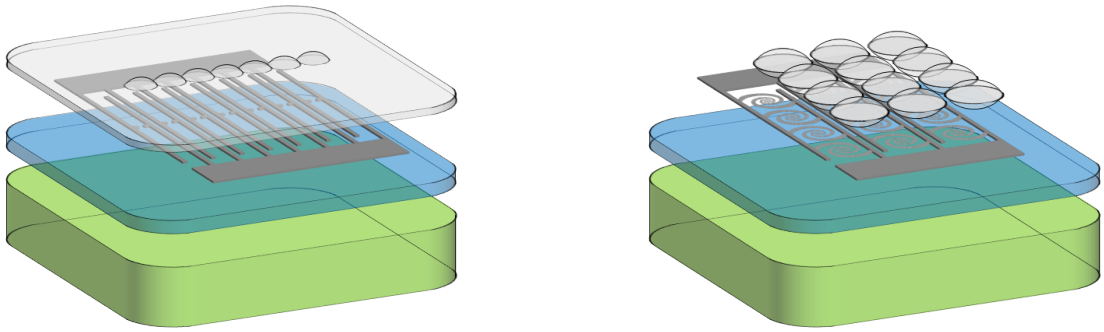

(a) (b)

Figure 6.6: PCA arrays in [139] and [52]. 3D layers structure exploded view drawing: a) linear array of Auston switches in [139], b) Array of spirals in [52]. The array of microlenses is also depicted.

the photoconductor material and a unidirectional dipoles excitation is induced without the necessity of any additional masking layer or photoconductor removal. In [139] a linear array of Auston-switches is presented, whereas in [52] a surface array of logarithmic spirals is discussed. In both the solutions array of microlenses are again used to efficiently distribute the laser power on each photoconductive element of the array, see Fig. 6.6(a), Fig. 6.6(b), respectively.

More recently in [74] the authors proposed an array solution similar to the large interdigited array in [64] with the masking metallizations. However, in order to have a higher transmitted electric field in the photoconductive material, they suitably shaped one of each couple of electrodes as shown in Fig. 6.7. By such shaping, a higher absorption of the optical power is obtained due to the excitation of plasmonic waves.

For the sake of completeness, we report another PCA array solution present in the literature, which was theoretically analyzed in [141], but whose realization and measurement is not available at the best of my knowledge. The authors presented a surface array of

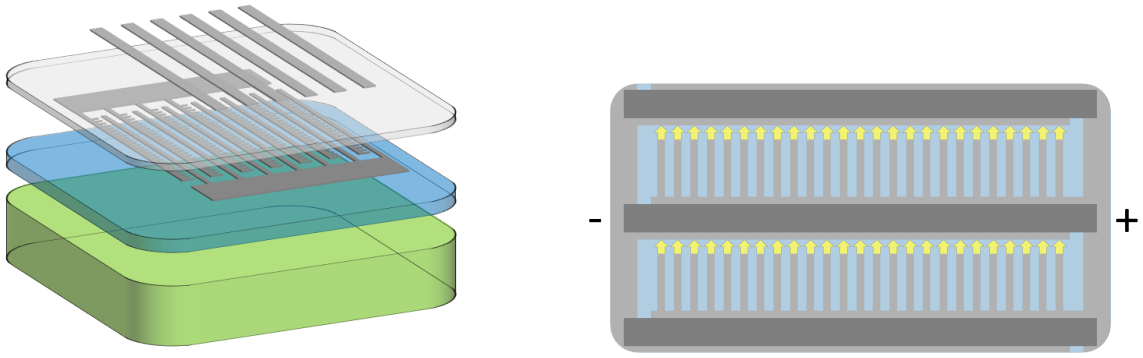

(a) (b)

Figure 6.7: PCA array in [74]. a) 3D layers structure exploded view drawing; b) 2D top view of the structure. The yellow arrows represent the orientation of the excited dipoles inside the photoconductor material.

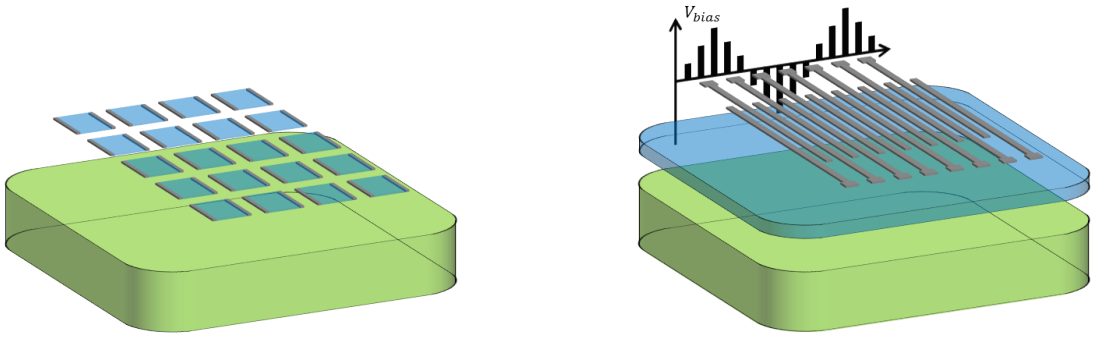

(a) (b)

Figure 6.8: PCA array in [142] and [141]. 3D layers structure exploded view drawing: a) at each photoconductive element the same bias voltage is applied at the relevant electrodes, b) the sinusoidal modulation of the bias voltage, relevant to each electrode, is shown.

PCA in which, on a dielectric substrate, photoconductive elements are deposited, each one connected to biasing voltage electrodes as shown in Fig. 6.8(a). In the paper the authors analyzed the structure theoretically giving an estimation of the radiated power. However, they do not discuss how such theoretical prototype can be realized and, consequently, how the theoretical model can be validated.

Finally, with the aim of obtaining a steerable radiated beam, a photoconductive array solution was discussed in [142]. It consisted in an array of parallel metallic strips, connected to electrodes which were independently biased and placed on a semi-insulating GaAs substrate. The authors suggested that the structure can be biased by using a periodic sinusoidal voltage as illustrated in Fig. 6.8(b). In this way they realized a structure in which the amplitude of the photocurrent between every two adjacent electrodes can be controlled. They also show that by changing the periodicity of the biasing voltage, it is possible to steer the radiated far field pattern. However, such property is intrinsically narrowband

since related to the periodicity of the electrodes and the biasing voltage. Therefore it not suitable to be used for radiating power on a large bandwidth in an efficient way.

6.3 Problems with the State of the Art

In the following, the main limitations with the solutions present in the state of the art will be addressed. Even though this analysis is necessarily qualitative, due to space reasons, the contained considerations are valid and indicative of the design trends that characterize the state of the art.

All the solutions presented above are not suitable to radiate energy on a large bandwidth. Consequently they cannot efficiently radiates the wideband signal excited in the photoconductive gap, when it is illuminated by a laser operating in the PW mode. Nor they are suited to support a wide frequency reconfigurability in the CW mode. There are different reasons for the unsuitability of each solution, but all these antennas suffer from essentially the same problem. A photoconductive source, generating active power and defined at electrode terminals, can have an equivalent Thévenin (or Norton) circuit representation, that is characterized by a voltage (or current) generator and real internal impedance.

It is well known in RF circuits that in order to radiate the power from an antenna connected to a source terminal there must be a match between the equivalent generator impedance and the antenna impedance. Unfortunately this cannot happen effectively for the antennas in the solutions in [2, 62, 64, 66, 68–70, 74, 139, 140]. This is because all these antennas and arrays are evolutions of dipole structures in which the current distribution (shaded surfaces in Fig. 6.9(a)) vanishes at the element end-points. Thus depending on the THz radiated frequency, these antennas are either short or comparable to the wavelength. This means that their antenna impedances are either strongly reactive with only a minimal real part (when the dipoles are short) or varying importantly as a function of the frequency (when the dipoles are resonant). In both these situations it essentially impossible to match, on a large frequency bandwidth, the antenna impedance to the equivalent impedance generator (whatever its value).

The solution in [52] is the only one that is not suitable for a different reason. Since it consists in an array of spiral antennas feeding an extended-hemispherical silicon lens, it is not suitable because of the spacing between the different radiating elements. This spacing ($500\,\mu$m) is so large that the grating lobes in the pattern appear at 150 GHz. So, even if spiral antennas theoretically exhibit wide impedance bandwidth (0.1 THz − 1.5 THz), the radiation efficiency of the entire structure (array + lens) is expected to be extremely poor.

As far as the structure presented in [142] shown in Fig. 6.8(b), the adopted periodic biasing voltage, aimed at focusing the coherent THz radiation from the different antennas in specific directions also dictates very narrow bandwidths of operation.

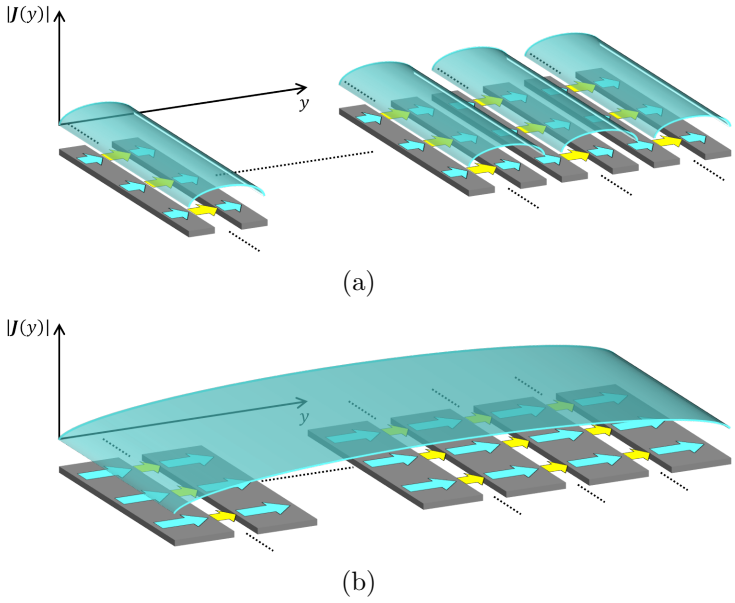

Figure 6.9: a) Currents distribution on a standard array of dipoles/slots. b) Currents distribution on a connected array of dipoles/slots. The yellow arrows represent the array exciting current dipoles, whereas the cyan arrows represent the currents flowing on the array. The shaded surfaces are representative of the amplitude of the electric currents.

6.4 Photoconductive Connected Array

In this section, two novel solutions based on the connected array concept [24–30] are presented. The connected array concept has emerged in the antenna community in the last ten years and has been pioneered mostly by the group to which the author of this thesis belongs. A connected array is an array of radiating elements that are fed by impressed currents at multiple periodic locations, see Fig. 6.9(b). The feeding terminals, which are strongly coupled, can then be viewed as generating a unique total current distribution over the entire array as it is shown in Fig. 6.9(b). Such current does not vanish at the end points of each element of the array as in standard array technology shown in Fig. 6.9(a). It is smooth and continuous on the entire structure. The radiation impedance does not show resonances that would otherwise be observed over a large bandwidth for conventional resonant slot or dipole arrays. Theoretically, the realistic limiting factor of a connected array are the edge and vertex truncation effects of the finite array. Moreover, it was also shown that they can be used to efficiently illuminate the surface of dielectric lens antennas on a large bandwidth [28–30]. The proposed system is therefore very promising for obtaining a high power terahertz radiation.

6.4.1 Impressed THz Currents and Relevant Biasing Network Design

The first structure is the one shown in Fig. 6.10. It consists in a series of parallel metallic strips forming an array of slots distributed on a thin slab of photoconductive material. Whereas, for the second structure ,shown in Fig. 6.11, a series of parallel metallic strips forming an array of dipoles distributed on a thin slab of photoconductive material is considered. When the structures are illuminated by a laser, a current is impressed over feeding gaps and the total current is different from zero over the entire array structures. The key difference with respect to existing solution that have been previously proposed, and mentioned in Section 6.2, is the biasing scheme that is adopted in order to actually achieve the smooth uniform current distribution inside the array structure, see Fig. 6.9(b). It is necessary to properly polarize the strips, as in Fig. 6.10(a) and in Fig. 6.11(a), so that the total current does not vanish at the end points of two consecutive strips, as it does in all solutions of Section 6.2. With reference to Fig. 6.10(a) and Fig. 6.11(a), a biasing voltage is applied between the first and the last strip. The voltage is equally divided among all the strips since they behave as capacitors connected in series in absence of laser illumination on the photoconductive gaps. In this way, each couple of consecutive strips, between the applied voltage difference, presents the same voltage difference giving rise to biasing electric fields all oriented in the same direction across the strips. When the laser illuminates the structure, the currents impressed in the photoconductor flow congruently with a unique biasing direction. As a consequence the total current on the structure is continuous across all the feeding elements and effectively realizes a connected array, as in Fig. 6.10(b), Fig. 6.11(b), with each feeding gap characterized by the desired virtually frequency independent antenna impedance.

By suitably tuning the optical, electrical, and geometrical parameters of the array, a specific value for the equivalent generator impedance can be obtained, which can be reasonably expected to be almost frequency independent in the desired bandwidth of interest as it is has been shown in Chapter 2.

With respect to similar existing solutions, with the present connected array solution it is actually possible to match this generator impedance associated to each feeding gap to the antenna impedance of each terminal composing the connected array. This is the most important break-through of the presented structure.

Furthermore, with respect to existing solutions the entire array structure is used effectively. Indeed the proposed biasing network allows to efficiently distribute the photoconductive elements on the array surface without recurring to any mask on the photoconducting material and on the electrodes, as in Fig. 6.10 and Fig. 6.11. It is worth noting that the structure proposed in [142] could have easily been biased to realize an effective connected array structure. However, in 1991, connected arrays had not emerged as a concept for broad band radiation and accordingly the authors never proposed such a feeding/biasing solution.

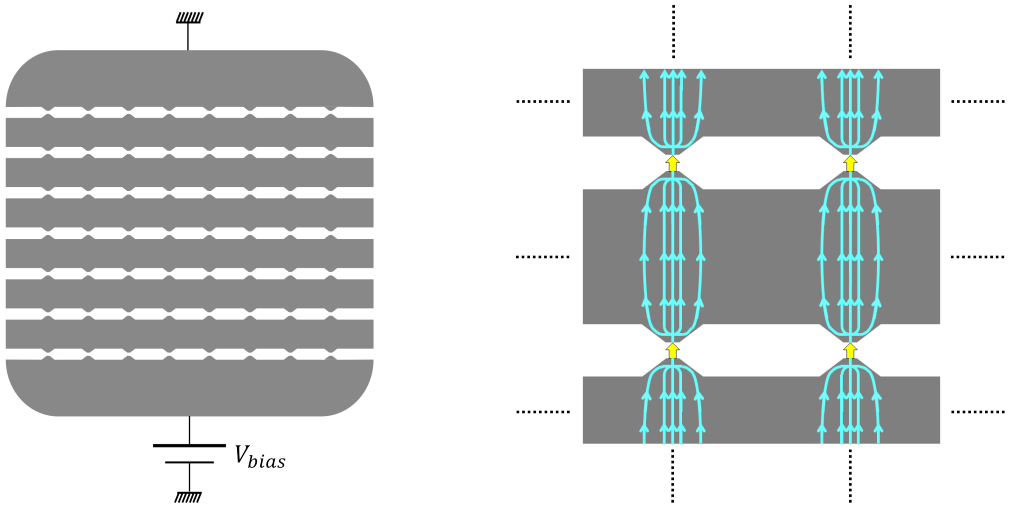

Figure 6.10: a) PCA slot connected array biasing network. b) Enlargement of four elementary cells of the PCA connected array. The yellow arrows represent the photo-induced dipoles, whereas the cyan lines and arrows represent the currents flowing on the array.

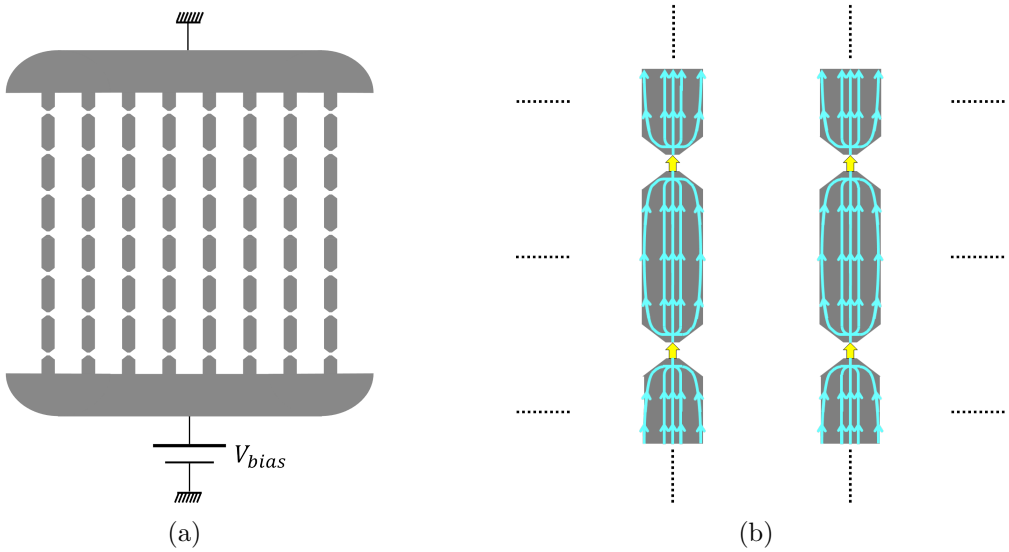

Figure 6.11: a) PCA dipole connected array biasing network. b) Enlargement of four elementary cells of the PCA connected array. The yellow arrows represent the photo-induced dipoles, whereas the cyan lines and arrows represent the currents flowing on the array.

6.4.2 Array System Design

The proposed entire system for obtaining a high power terahertz radiation is shown in Fig. 6.12(a). $N_y + 1$ strips are placed on a photoconductive material slab and are oriented

along the x axis. They are biased according to the biasing network proposed in the previous section. Each couple of strips forms a slot of width W_s. The total number of slots is N_y. Each slot presents N_x exciting gaps, obtained by a periodical tapering, whose smallest dimensions are W_x and W_y along the x and y axes, respectively as it is shown in Fig. 6.12(b). The distance along y between the centers of consecutive strips is d_y, whereas the distance between the centers of consecutive gaps along each slot is d_x. Therefore, the $N_x \times N_y$ elementary cell of the connected array have dimensions $d_x \times d_y$, see Fig. 6.12(b). Such strips arrangement realizes an array of connected slots. By changing the arrangement of the strips as in Fig. 6.11(a), an array of connected dipoles can be obtained.

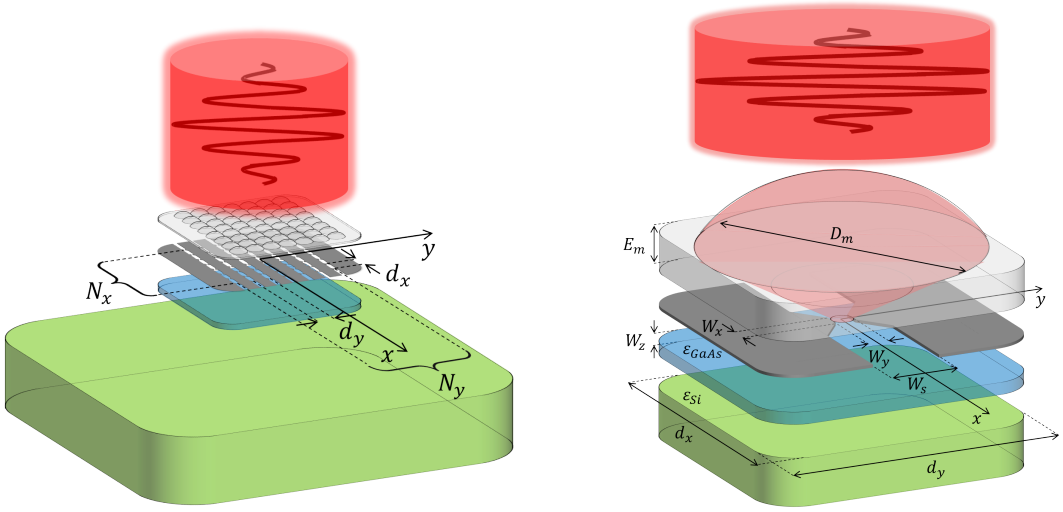

(a) (b)

Figure 6.12: a) Entire THz system: PCA connected array, microlenses array, and silicon focusing lens. The optical laser beam illuminating the structure is also depicted. b) exploded view of an elementary cell and single micro-lens detail.

The gaps of the slots and the periods along x and y of the connected array are properly designed in order to obtain a desired input impedance for each array element. Furthermore, they are suitably designed in order to have a high biasing electric field on each gap for obtaining high current intensities when the photoconductor is excited. With the aim of feeding the array only in correspondence of the gaps and to efficiently use the optical power supplied by the laser, a microlenses array is used as in [52, 68, 139]. The structure of the entire array system and the elementary cell are shown in Fig. 6.12(a) and Fig. 6.12(b), respectively. Note that the fine tuning of the feeding gaps geometry, and optical design, in order to obtain a real equivalent impedance generator of value comparable to the antenna impedance is of absolute essence to maximize the THz power radiation.

On the side of the semiconductor chip, which is not loaded by the strip metallizations, a silicon lens can be placed for obtaining a desired focusing of the power radiated by the connected array as in Fig. 6.12(a).

The proposed solution has all the necessary features that allow an efficient radiation

on a large bandwidth. It is therefore an optimal candidate for obtaining a high power radiation at THz regimes.

Moreover the photoconductive connected array proposed are suitable solutions also as receiver of ultra-wide bandwidth THz radiation, increasing considerably the receiving signal-to-noise ratio. Such receivers can be obtained simply using the same structures proposed without the bias scheme and connect them directly to a lock-in amplifier for the read out of the output current.

6.5 Prototype Design

A prototype design of a photoconductive connected array is presented in this section. In particular, the same electric parameters for the LTG-GaAs slab described in Chapter 2 are considered: a relative electric permittivity $\varepsilon_r = 13$; an absorption coefficient $\alpha = 10^6\,\mathrm{m}^{-1}$, carriers mobility $\mu = 240\,\mathrm{cm}^2/\mathrm{Vs}$, and carriers life-time $\tau = 0.3\,\mathrm{ps}$. The thickness of the photoconductive LTG-GaAs slab $W_z = 2\,\mu\mathrm{m}$ has been considered. The connected array has been designed in such a way to be suitable to radiate energy efficiently in a bandwidth from 0.1 THz up to 0.4 THz. The array is formed by $N_y = 5$ slots of width $W_s = 81\,\mathrm{mum}$. The slots are excited at $N_x = 5$ gaps, whose dimensions are $W_x = W_y = 4\,\mu\mathrm{m}$. The unit cell has dimensions $d_x = d_y = 150\,\mu\mathrm{m}$. Therefore, the entire array dimensions are $750\,\mu\mathrm{m} \times 750\,\mu\mathrm{m}$. The array is used to illuminate a silicon lens of radius $\varepsilon_{Si} = 11.9$. We used a pulsed laser beam at an operating wavelength of 800 nm, with a repetition rate of 80 MHz, a pulse width of 100 fs, and an average laser power of $P_{laser} = 1\,\mathrm{W}$. Each slot was biased by a voltage of 16 V by using a biasing network as that shown in Fig. 6.10(a), guaranteeing an electric field $E_{bias} = 4\,\mathrm{V}/\mu\mathrm{m}$ on each gaps of the array. The total voltage applied to the PCA connected array is therefore 80 V. The optical power has been considered a gaussian spatial distribution with a diameter at $-3\,\mathrm{dB}$ equal to the diagonal size of the array $D_{-3\mathrm{dB}} = 1\,\mathrm{mm}$. Considering the spillover loss of the laser beam, due to the spatial distribution of the laser beam, only half of the average laser power is used to excite the array $P_{laser}^{array} = 500\,\mu\mathrm{m}$. Such $-3\,\mathrm{dB}$ laser beam is split by an 5×5 array of microlenses of diameter equal to cell size of the array $D_m = 150\,\mu\mathrm{m}$, in order to focus each portion of the laser power on each photoconductive gap and excite the array.

The central element of the array is therefore excited with $P_{laser}^{cell} = 20\,\mathrm{mW}$. By using the equivalent circuit model described in Chapter 2, the equivalent generator resistance of the photoconductive gap of the cell is $Z_g^{cell} = 65\,\Omega$, providing an available power $P_{available} = 120\,\mu\mathrm{m}$ over the operative bandwidth of the array $0.1\,\mathrm{THz} - 0.4\,\mathrm{THz}$. Because of the small number of elements, in order to take into accounts for any edge effects on the array elements, the array has been simulated with a commercial software [94]. The simulation has been carried out considering the all the element excited simultaneously with a tapering of the excitation of the gaps according to the gaussian spatial profile of the laser beam. The active impedances of the elements in one quadrant of the array configuration (Fig. 6.13(a)) have been calculated, and resorting the equivalent circuit of Chapter 2, the radiated energy spectrum of each element has been calculated and they are shown in Fig. 6.13. Summing

all the energy contributions of each elements of the array, the total average power radiated by the array is $\bar{P}_{source} = 2.35\,\mathrm{mW}$.

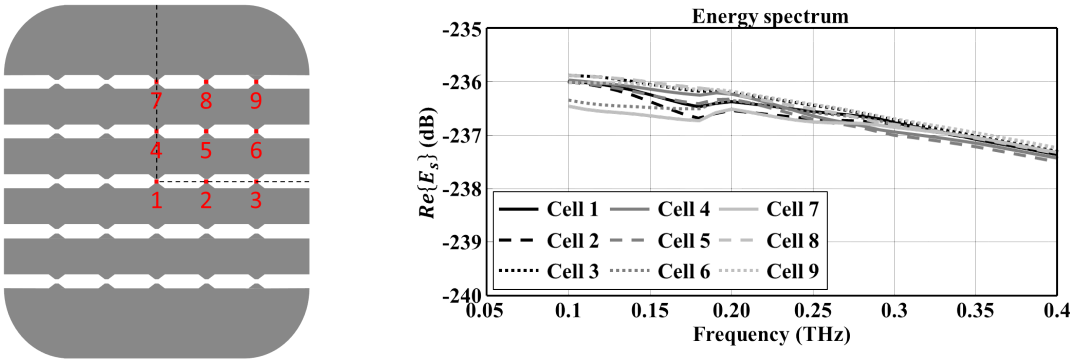

(a) (b)

Figure 6.13: a) Displacement of the array cells used for the simulation, and b) energy spectra radiated by array elements.

6.6 Conclusions

In this chapter, the state of the art of photoconductive large area emitters, and its relevant problems have been been discussed. All the actual solutions, presented in the literature until nowadays, are based on small dipole array configurations, making them not suitable to radiate efficiently the energy generated over a large bandwidth by the optically pumped semiconductor material.

In order to overcome the common problem of the state of the art for large area emitters and to increase effectively the radiated power by PCA, a solution based on the well established concept of connected array has been proposed in this chapter. The use of such concepts has been possible thanks to the development of the equivalent circuit for photoconductor generator proposed in this thesis. The photoconductive connected array solution promises to be effective for radiating efficiently energy up to the THz frequencies. The proposed solution has all the necessary features that allow an efficient radiation on a large bandwidth, increasing (around one order of magnitude) the radiated power by PCA.

Moreover the proposed photoconductive connected array is a suitable solution also to be used as receivers of ultra-wide bandwidth THz radiation, by removing the bias generator and connecting the array to a lock-in amplifier for the readout of the induced output currents. The use of such solution as a receiver will increase also the sensitivity of the receiver of the same orders of magnitude provided by the emitter (around one order of magnitude). As result the combined used of the photoconductive connected array as emitter and receiver will allowed finally to spread such technology to applications (e.g. radar system), from which the PCA were kept away, because of the power bottleneck provided by the state of the art until nowadays.

Chapter 7

Conclusions and Outlooks

This thesis describes the research work carried out over a period of four and a half years (from October 2012 till March 2017) in the Terahertz Sensing Group of the microelectronics department of Delft University of Technology, Delft, Netherlands.

The topic treated in this work is of particular interest in the field of THz technology. Up to now, PCAs have been confined to niche scientific applications because of the low values of detected power. This research work has been focused on the estimation of the radiated power by modelling both the photoconductive source and the QO channel. It has been found that the actual systems are very inefficient. Therefore, there is a significant margin to enhance the level of detected power and therefore the dynamic range in future time-domain sensing systems.

The scope of this thesis was to model, analyze and design PCAs, dealing with theoretical and practical aspects involved in such devices. The results of this research work allow to extend to PCA antenna design the vast heritage of wide band microwave engineering tools that have been developed mostly for analyzing detectors in radiometric domains. This research work can open the way for more standard engineering optimization of wide band coherent THz sources.

In this chapter, the conclusions and the most significant results of the research are summarized, and moreover some future outlook of this research will be discussed.

7.1 Equivalent Circuit Representation for Photoconductive Generators

A Norton equivalent circuit for PCAs has been derived. The circuit describes clearly the coupling between the photoconductor generator and the antenna in the frequency domain. The circuit has been derived starting by the classical electrodynamic model for semiconductors that are optically pumped, and it takes into account for the properties of the semiconductor material, the geometrical parameters of the source, and the laser features involved. Dynamic phenomena such as carriers overshoot and saturation, which occur when high bias field and high laser fluences are applied to the semiconductor, are not

considered in the model. The equivalent circuit allows to evaluate the impedance and the current generated by the photoconductor source in frequency domain under fixed working conditions.

The equivalent circuit represents a powerful tool for analyzing and designing PCAs, since the energy spectrum and the power radiated by the photoconductive antenna can be easily evaluated by resorting to such circuital representation. The possibility to compute the energy spectrum associated to the photoconductive antenna allows to have a clear picture of the coupling between the photoconductor generator and the antenna in terms of generator-antenna matching and dispersion over the operative bandwidth. Moreover, this representation permits to analyze the radiation performances of PCAs through a quasi-optical channel, by resorting to an electromagnetic model of the channel.

7.2 Analysis of Photoconductive Antennas

The analysis of PCAs radiation performance as a function of the frequency has been extensively discussed in this thesis. The analysis has been made possible thanks to the modelling of the photoconductor generator with the proposed Norton equivalent generator, allowing to use the classical electromagnetic tools for the analysis of the radiation performances of PCAs. Indeed, an electromagnetic model of the QO channel, typically involved for the experimental characterization of PCAs, has been proposed and used for the analysis. The most common antenna geometries used as PCAs have been characterize in terms of radiation performances, and coupling to the QO channel (source-to-detector). The entire model (equivalent circuit and channel) allows to predict accurately the performances of the PCAs, evaluating the dispersion of the energy spectrum through the entire system, and computing the average power radiated by the PCAs and detected by the detector of the measurement system.

7.2.1 Electromagnetic Model for QO Channel

An electromagnetic model of the measurement system for characterizing PCAs has been also developed in this work. The analysis of the entire QO channel (source-to-detector) has been described in terms of efficiency at each frequency of the operative bandwidth. In order to compute such cumulative efficiency, the separate radiation efficiencies of the PCAs, the reflectors chain, and the detector have been accurately evaluated and cascaded. The radiation efficiency of the photoconductive lens antenna has been evaluated by taking into account for the front-to-back losses, the dielectric losses inside the lens, and reflection losses at the lens interface. The efficiency of the reflectors chain has been characterized evaluating the spillover efficiency of the chain when it is fed by the PCAs. Finally, the coupling between the reflectors chain fed by the PCAs and the detector has been characterized by means of the coupling efficiency taking into account for the spillover losses between the reflectors chain and the antenna of the detector, and the losses due to the coupling with the modes excited inside the waveguide, which connected the antenna with the sensor of

the detector.

Thanks the characterization of the QO channel by means of the electromagnetic model, jointly with the proposed equivalent circuit representation, the PCAs performances can be easily evaluated by means of the analysis of the energy spectrum propagating through the QO channel. Such analysis allows to have a clear picture of the dispersion and efficiency through the entire system, moreover it allows to predict accurately the power budget of the entire system (source-to-detector).

The comparative analysis of the performances of the different PCAs shows clearly that the major impact on the power budget of the PCAs is due to the radiation properties of the antenna sources.

7.3 Experimental Validation of the PCA and QO Models

Four different prototypes of PCAs have been realized in order to demonstrate the validity of the equivalent circuit of the photoconductor generator and the electromagnetic model of the QO channel. The same photoconductive lens antennas used in the numerical analysis have been manufactured. The planar antenna geometries have been realized on a LTG-GaAs material placed on a SI-GaAs chip, the biasing circuit of the PCAs has been realized in printed circuit technology. To finalize the prototypes, the antenna chip and the biasing printed circuit board and the silicon lens have been assembled.

Both power and spectrum measurements have been performed. The power measurement of the prototypes have been carried out by using two different detectors, in order to ensure the accuracy of the measurements. Both the detectors have been coupled to the PCA prototypes by using the same reflectors chain. The entire measurement system have been realized in such a way to reconstruct exactly the entire QO channel used for the numerical analysis. Both the detector have been calibrated by using a commercial CW tunable photoconductive source with known output power. The spectra measurements have been carried out by coupling an electro-optic crystal to the PCA prototypes by means of the same reflectors chain used for the power measurements.

The excellent agreement obtained by the comparison between the numerical results and the measurements, certainly within the limited uncertainties of the measurements setup and material properties, provides a solid validation of the theoretical model proposed in this thesis.

7.4 Analysis of Logarithmic Spiral Lens Antennas Radiation

Part of this research work has been devoted to the investigation of the performances of the radiation of spiral antennas in the presence of dielectric lenses. The results of the investiga-

tion have demonstrated the presence of the leaky wave radiation, when the spiral antenna are printed at the air dielectric interface. For designing logarithmic spiral antennas coupled to a synthesized elliptical lens, in order to achieve high aperture efficiency over a broad bandwidth, it has be found not sufficient to simply scale the optimal self-complementary geometry typically used for free space, because of the leaky wave radiation associated to planar antenna at the interface air dielectric. The results of the investigation has led to a design of a logarithmic spiral antenna lens antenna, which provides an high aperture efficiency over a decade frequency bandwidth. However, only using extremely thin substrates ($\lambda/2000$) allows to feed this design with a planar feeding system without limiting the bandwidth. In order to reduce the limitation due to the planar feeding system, a new design with the introduction of a small air gap between the spiral antenna and the bottom lens interface has been proposed, which allows to relax the constraint of the thickness of the substrate ($\lambda/20$). Coupling the new design with a synthesized elliptical lens, directive patterns without sidelobes over a decade frequency bandwidth can be achieved. Moreover, the new spiral design coupled with a hemispherical lens with low extension height reduces the frequency dispersion of the radiated pulses. That is due to the enhancement of the leaky radiation when the air gap is introduced between the antenna and the lens, which provides more directive patterns inside the dielectric.

7.5 Design of a Photoconductive Connected Array

A novel design for photoconductive sources has been also presented, based on the concept of connected array which is now well established in the microwave community. The proposed solution defines a new breakthrough with respect to the existing state of the art of large area emitters. Indeed, thanks to the intrinsic wideband behavior of connected array, the proposed design is suitable to radiate the energy spread on the wideband spectrum generated by the photoconductor source, when it is excited by optical power. The array has been designed proposing an ad-hoc biasing network, in order to properly bias all the array cells, preserving the connected structure of the elements. Moreover, a design of an optical system has been proposed, in order to optically excite all the elements of the photoconductive array coherently.

By using the equivalent circuit of the photoconductor generator proposed and validated in this work, the proposed design is expected to increase the amount of radiated power of two orders of magnitude with respect to the state of the art solutions. Moreover, such design is suitable to be employed also as receiver of ultra-wide bandwidth radiation, increasing also the sensitivity of the detector by two orders of magnitude provided by the source.

A demonstrator of the proposed novel photoconductive source design is now being realized, and a complete characterization of the prototype will be performed by means of power and spectrum measurements, proving the validity of the concept.

7.6 Future Outlooks

The novel equivalent circuit developed for describing the generation of energy over a wide band by means of optically pumped semiconductor extends the vast heritage of wide band microwave engineering tools to PCA design. This opens the way for more standard engineering optimization of wide band THz sources.

The future prospects opened by this research work are highlighted below:

- The introduction of dynamic effects in the electrodynamic model of the optically pumped semiconductor material (i.e. carriers overshoot and saturation) can be investigated in order to improve such model, and a new and more complete Thévenin/Norton equivalent circuit could be derived, by using the procedure developed in this research work.

- The possibility of improve the dynamic range of the present THz TDS can be investigated. Thanks to the modelling for PCAs presented in this thesis, more efficient PCAs for the THz TDS can be designed. High level of power radiated by PCAs is crucial to increase the dynamic range of the system and as consequence to increase the quality of the spectroscopic measurements.

- The potential advantages of using in transmission and in reception more efficient PCAs can be exploited in THz imaging systems. Improving the signal-to-noise ratio the system imaging speed will increase dramatically, since shorter integration times will be needed for recovering the detected signals.

- The availability of high power level radiated and high sensitivity provided by the photoconductive connected array opens the possibility to develop new wideband radar systems. The increase of the signal-to-noise ratio, and the wide bandwidth of the signal generates by the source can be exploited to realize radar system with higher spatial resolution.

- In all these scenarios, a further research effort will be required in order to make an integrated solution of the photconductive array, where the microlenses array will be embedded directly on the antenna array chip.

Appendix A

Modelling of the Photoconductor Generator

In this appendix an expression for the conductivity of the volume of photoconductive material, depicted in Fig. 2.1, is derived, when a laser beam, with the appropriate carrier frequency, impinges on it. As discussed in Section 2.2, the conductivity of a photoconductor can be expressed in terms of the charge carrier density (electrons and holes) generated by an impinging electromagnetic wave. In order to explicitly derive an expression for the conductivity, one needs to calculate the charge concentration $n(\mathbf{r};t)$. Such concentration can be estimated by resorting to the semiconductor continuity equation [143, 144]:

$$\frac{\partial}{\partial t} n(\mathbf{r};t) = g_c(\mathbf{r};t) - r(\mathbf{r};t) \tag{A.1}$$

In (A.1), the term $g_c(\mathbf{r};t)$ is the carriers generation rate, whereas $r(\mathbf{r};t)$ is the carrier recombination rate, which can be expressed as:

$$r(\mathbf{r};t) = \frac{n(\mathbf{r};t)}{\tau} \tag{A.2}$$

where τ is the charge carrier lifetime. Here, the time τ is assumed to be the average value of the lifetimes for all the different kind of recombination phenomena in the photoconductor, according to the Matthiessen's rule [144]. In the semiconductor continuity equation (A.1) the carrier density at the thermal equilibrium is neglected, since it is typically negligible in presence of the pumping. Moreover, in (A.1) the diffusion term is also neglected, since the biasing is considered far dominant in inducing electric current across the investigated gap. Finally, we also neglect any spatial variation of the drift current, assuming negligible the spatial variation of the charges because of the almost uniform illumination of the gap, and assuming an approximately constant bias electric field across the gap. Therefore, in relation to the THz current generation, the dominant terms in the continuity equation (A.1) are the carriers generation $g_c(\mathbf{r};t)$ and recombination $r(\mathbf{r};t)$ terms.

The generation rate $g_c(\mathbf{r};t)$ is a function of the modulated laser signal impinging on the surface (W_x, W_y) of the photoconductor volume and it is proportional to the variation

of the transmitted Poynting vector in the volume of the semi-conductor material through the relation:

$$g_c(\mathbf{r};t) = -\frac{1}{hf_g}\frac{\mathrm{d}}{\mathrm{d}z}\left[\left(1-|\Gamma|^2\right)\tilde{\mathbf{s}}(\boldsymbol{\rho},z=0;t)\,e^{-\alpha|z|}\right]\cdot\hat{\boldsymbol{z}} \tag{A.3}$$

where, $\tilde{\mathbf{s}}(\boldsymbol{\rho},z=0;t)$ is the time-varying envelope of the Poynting vector distribution impressed by the laser source (Appendix C) evaluated at the interface between the air and the semiconductor and it only depends from the z-transverse vector $\boldsymbol{\rho}$. α, Γ, h, and f_g are the same parameters defined in Section 2.2. By using (C.9), the average generation rate along z can then be obtained as:

$$\bar{g}_c(\mathbf{r};t) = \frac{1}{W_z}\int_{-W_z}^{0} g(\mathbf{r};t)\,\mathrm{d}z = \left(1-|\Gamma|^2\right)\frac{1-e^{-\alpha W_z}}{W_z}\frac{1}{hf_g}\left|\tilde{\mathbf{s}}_n(\boldsymbol{\rho},z=0)\right|\tilde{s}(t) \tag{A.4}$$

with $-W_z \le z \le 0$. Using (A.2) and (A.4) in (A.1) and transforming (A.1) in the spectral domain with respect to the time, one gets:

$$j\omega N(\mathbf{r};\omega) + \frac{N(\mathbf{r};\omega)}{\tau} = \left(1-|\Gamma|^2\right)\frac{1-e^{-\alpha W_z}}{W_z}\frac{1}{hf_g}\left|\tilde{\mathbf{s}}_n(\boldsymbol{\rho},z=0)\right|\tilde{S}(\omega) \tag{A.5}$$

this algebric equation can be solved as:

$$N(\mathbf{r};\omega) = \left(1-|\Gamma|^2\right)\frac{1-e^{-\alpha W_z}}{W_z}\frac{1}{hf_g}\frac{\tau}{1+j\tau\omega}\left|\tilde{\mathbf{s}}_n(\boldsymbol{\rho},z=0)\right|\tilde{S}(\omega) \tag{A.6}$$

with $-W_z \le z \le 0$. From (A.6), one can define the frequency response to the laser excitation of the photoconductor material as:

$$H(\omega) = \frac{1}{hf_g}\frac{\tau}{1+j\tau\omega} \tag{A.7}$$

In order to evaluate the carriers density in the volume of the material, one needs to apply the inverse Fourier transform of (A.6):

$$n(\mathbf{r};t) = \frac{1}{2\pi}\int_{-\infty}^{+\infty} N(\mathbf{r};\omega)\,e^{j\omega t}\,\mathrm{d}\omega \tag{A.8}$$

From (A.8) one can evaluate the time-varying conductivity in each point of the volume (W_x, W_y, W_z) due to the free carriers generated by the impinging laser power as:

$$\sigma(\mathbf{r};t) = e\,\mu\,n(\mathbf{r};t) \tag{A.9}$$

The bulk conductivity of the photoconductor volume can be obtained by the spatial averaging of (A.9) on the volume (W_x, W_y, W_z).

Appendix B

Time-Varying Conductance of Laser Pumped Photoconductor Source

In this appendix, the expression of the conductance of the photoconductor gap, depicted in Fig. 1.2(b), is derived, when a laser beam excites it with the appropriate carrier frequency. As mentioned in Section 2.3.1, the time-varying conductance of a volume of photoconductor, pumped by a laser beam, can be derived from the spatial average current over the photoconductor, obtained by applying the Ohm's law on the photoconductor volume, as is shown in (2.4)–(2.10):

$$g\left(t\right)=\frac{1}{W_y^2}\int_{-\frac{W_y}{2}}^{\frac{W_y}{2}}\int_{-\frac{W_x}{2}}^{\frac{W_x}{2}}\int_{-\frac{W_z}{2}}^{0}\sigma\left(\mathbf{r};t\right)\mathrm{d}z\,\mathrm{d}x\,\mathrm{d}y \tag{B.1}$$

For the sake of simplicity, let us consider the spectrum of the time-varying conductivity calculated by its FT:

$$\begin{aligned}G\left(\omega\right)=FT\left[g\left(t\right)\right]=\\ =\frac{1}{W_y^2}\int_{-\frac{W_y}{2}}^{\frac{W_y}{2}}\int_{-\frac{W_x}{2}}^{\frac{W_x}{2}}\int_{-\frac{W_z}{2}}^{0}FT\left[\sigma\left(\mathbf{r};t\right)\right]\mathrm{d}z\,\mathrm{d}x\,\mathrm{d}y=\\ =\frac{1}{W_y^2}\int_{-\frac{W_y}{2}}^{\frac{W_y}{2}}\int_{-\frac{W_x}{2}}^{\frac{W_x}{2}}\int_{-\frac{W_z}{2}}^{0}\Sigma\left(\mathbf{r};\omega\right)\mathrm{d}z\,\mathrm{d}x\,\mathrm{d}y\end{aligned} \tag{B.2}$$

where $\Sigma\left(\mathbf{r};\omega\right)$ is the spectrum of the conductivity $\sigma\left(\mathbf{r};t\right)$ of the photoconductor gap. Resorting to (A.6)–(A.7) and (A.9), the spectrum of the conductivity can be expressed as:

$$\Sigma\left(\mathbf{r};\omega\right)=e\,\mu\,\left(1-\left|\Gamma\right|^2\right)\frac{1-e^{-\alpha W_z}}{W_z}H\left(\omega\right)\left|\tilde{\mathbf{s}}_n\left(\boldsymbol{\rho},z=0\right)\right|\tilde{S}\left(\omega\right) \tag{B.3}$$

The spectrum of the conductance (B.2) can be rewritten as:

$$G(\omega) = \frac{1}{W_y^2} \int_{-\frac{W_y}{2}}^{\frac{W_y}{2}} \int_{-\frac{W_x}{2}}^{\frac{W_x}{2}} \int_{-\frac{W_z}{2}}^{0} e\,\mu\,\left(1 - |\Gamma|^2\right) \cdot \\ \cdot H(\omega)\,\frac{1 - e^{-\alpha W_z}}{W_z}\,|\tilde{\mathbf{s}}_n(\boldsymbol{\rho}, z=0)|\,\tilde{S}(\omega)\,\mathrm{d}z\,\mathrm{d}x\,\mathrm{d}y \quad \text{(B.4)}$$

Multiplying and dividing (B.4) for the area of the spatial distribution of the laser beam Poynting vector at the photoconductor interface $A_{laser} = \int_{-\infty}^{+\infty}\int_{-\infty}^{+\infty} \tilde{\mathbf{s}}_n(\boldsymbol{\rho}, z=0)\cdot\hat{\mathbf{z}}\,\mathrm{d}x\,\mathrm{d}y$, according to (C.8), the spectrum of the conductance can be rearranged as product of two terms:

$$G(\omega) = \left[\left(1 - |\Gamma|^2\right)\frac{1 - e^{-\alpha W_z}}{W_z}\frac{1}{A_{laser}}\int_{-\frac{W_y}{2}}^{\frac{W_y}{2}}\int_{-\frac{W_x}{2}}^{\frac{W_x}{2}}\int_{-\frac{W_z}{2}}^{0}|\tilde{\mathbf{s}}_n(\boldsymbol{\rho}, z=0)|\,\mathrm{d}z\,\mathrm{d}x\,\mathrm{d}y\right]\cdot \\ \cdot\left[\frac{A_{laser}}{W_y^2}e\,\mu\,H(\omega)\,\tilde{S}(\omega)\right] \quad \text{(B.5)}$$

It is possible to easily demonstrate that the term within first couple of brackets in (B.5) is a quantity that ranging $[0, 1]$, indeed:

$$0 \le 1 - |\Gamma|^2 \le 1$$

considering that $W_z \in [0, +\infty]$

$$0 \le 1 - e^{-\alpha W_z} \le 1$$

and according to (C.8):

$$0 \le \frac{1}{A_{laser}W_z}\int_{-\frac{W_y}{2}}^{\frac{W_y}{2}}\int_{-\frac{W_x}{2}}^{\frac{W_x}{2}}\int_{-\frac{W_z}{2}}^{0}|\tilde{\mathbf{s}}_n(\boldsymbol{\rho}, z=0)|\,\mathrm{d}z\,\mathrm{d}x\,\mathrm{d}y \le \\ \le \frac{1}{A_{laser}W_z}\int_{-\infty}^{+\infty}\int_{-\infty}^{+\infty}\int_{-\frac{W_z}{2}}^{0}|\tilde{\mathbf{s}}_n(\boldsymbol{\rho}, z=0)|\,\mathrm{d}z\,\mathrm{d}x\,\mathrm{d}y = 1$$

The term within the first couple of brackets in (B.5) into account for the laser power reflection at the interface between the air and the photoconductor, the laser power absorption by the photoconductor, and the spillover of the laser beam on the photoconductor area. It represents the absorption efficiency of the laser power by the photoconductor volume:

$$\eta(W_x, W_y, W_z, A_{laser}) = \left(1 - |\Gamma|^2\right)\frac{1 - e^{-\alpha W_z}}{W_z}\cdot \\ \cdot\frac{1}{A_{laser}}\int_{-\frac{W_y}{2}}^{\frac{W_y}{2}}\int_{-\frac{W_x}{2}}^{\frac{W_x}{2}}\int_{-\frac{W_z}{2}}^{0}|\tilde{\mathbf{s}}_n(\boldsymbol{\rho}, z=0)|\,\mathrm{d}z\,\mathrm{d}x\,\mathrm{d}y \quad \text{(B.6)}$$

The term within the second couple of brackets in (B.5) contains the spectral behavior of the conductance of the gap:

$$\tilde{G}(\omega) = \frac{A_{laser}}{W_y^2} e\,\mu\,H(\omega)\,\tilde{S}(\omega) \tag{B.7}$$

Hence the spectrum of the conductance of the photoconductor gap can be expressed in a compact form as:

$$G(\omega) = \eta(W_x, W_y, W_z, A_{laser})\,\tilde{G}(\omega) \tag{B.8}$$

and the time-varying conductance of the photoconductor gap can be evaluated simply by the IFT of (B.8):

$$\begin{aligned} g(t) = \frac{1}{2\pi}\int_{-\infty}^{+\infty} G(\omega)\,e^{j\omega t}\,\mathrm{d}\omega = \\ = \eta(W_x, W_y, W_z, A_{laser})\,\frac{1}{2\pi}\int_{-\infty}^{+\infty} \tilde{G}(\omega)\,e^{j\omega t}\,\mathrm{d}\omega = \\ = \eta(W_x, W_y, W_z, A_{laser})\,\tilde{g}(t) \end{aligned} \tag{B.9}$$

Appendix C

Modelling of the Pulsed Laser Source

A typical laser source used to generate electron-hole pairs in photoconductor is characterized by a spectral band (large for pulsed systems and small for continuous wave systems) centered around a laser carrier (e.g. $f_{laser} = 375\text{THz}$ for LTG-GaAs).

Considering the pulsed laser as a paraxial wave modulated by slowing-varying pulses, which means that the envelope of the pulse is relatively constant within a laser cycle, because of the narrow bandwidth, $B_{laser} \ll f_{laser}$, the spatial behavior is approximately the same as that of a monochromatic wave at frequency f_{laser} (CW laser) and it can be regarded as quasi-CW pulse wave. Referring to the coordinate system in Fig. 2.1, the laser electric field can be expressed as [145]:

$$\mathbf{e}(\mathbf{r};t) = \mathbf{e}_0(\boldsymbol{\rho},z)\, f\left(t-\frac{z}{c}\right)\cos\left(\omega_{laser}t - k_{laser}z + \varphi_{laser}\right) \tag{C.1}$$

where $f(t)$ is the periodic laser modulating signal, which can be expressed as:

$$f(t) = \sum_{i=-\infty}^{+\infty} \tilde{f}\left(t-\frac{z}{c}-iT_p\right) \tag{C.2}$$

where $\tilde{f}$ is the base band function defined on one period T_p of the laser pulse repetition rate. Moreover, in (C.1) $\mathbf{e}_0(\boldsymbol{\rho},z) = E_0\mathbf{e}_n(\boldsymbol{\rho},z)$ is the transverse spatial distribution of the beam electric field, E_0 is the peak amplitude of the electric field, and $\mathbf{e}_n(\boldsymbol{\rho},z)$ is the spatial distribution of the electric field with unitary amplitude, which is also function of z due to the diffraction effect of the laser beam. By considering only a single pulse of the laser, the EM power per unit area transported by such a wave is represented as a function of the electric and magnetic fields by using the Poynting vector:

$$\begin{aligned}\mathbf{s}(\mathbf{r};t) &= \mathbf{e}(\mathbf{r};t)\times\mathbf{h}(\mathbf{r};t) = \\ &= \frac{1}{\zeta}\left|\mathbf{e}_0(\boldsymbol{\rho},z)\right|^2\left|f\left(t-\frac{z}{c}\right)\right|^2\cos^2\left(\omega_{laser}t - k_{laser}z + \varphi_{laser}\right)(-\hat{\mathbf{z}})\end{aligned} \tag{C.3}$$

Defining the pulse time envelope of the Poynting vector as:

$$\tilde{s}_n\left(t-\frac{z}{c}\right) = \left|f\left(t-\frac{z}{c}\right)\right|^2 \tag{C.4}$$

The expression (C.3) can be written as:

$$\mathbf{s}\left(\mathbf{r};t\right)=\frac{1}{\zeta}\left|\mathbf{e}_0\left(\boldsymbol{\rho},z\right)\right|^2\tilde{s}_n\left(t-\frac{z}{c}\right)\cos^2\left(\omega_{laser}t-k_{laser}z+\varphi_{laser}\right)\left(-\hat{\mathbf{z}}\right) \tag{C.5}$$

Considering that the envelope of the electromagnetic pulse is realatively constant within a laser perios, one can calculate the average on the laser period ($T_{laser}=1/f_{laser}$) of the density power carried each second by the pulse can be calculated as:

$$\begin{aligned}\tilde{\mathbf{s}}\left(\mathbf{r};t\right)=&\frac{1}{\zeta}\left|\mathbf{e}_0\left(\boldsymbol{\rho},z\right)\right|^2\tilde{s}_n\left(t-\frac{z}{c}\right)\cdot\\&\cdot\frac{1}{T_{laser}}\int_{nT_{laser}}^{(n+1)T_{laser}}\cos^2\left(\omega_{laser}\tau-k_{laser}z+\varphi_{laser}\right)\mathrm{d}\tau\left(-\hat{\mathbf{z}}\right)=\\&=\frac{1}{2\zeta}\left|\mathbf{e}_0\left(\boldsymbol{\rho},z\right)\right|^2\tilde{s}_n\left(t-\frac{z}{c}\right)\left(-\hat{\mathbf{z}}\right)\end{aligned} \tag{C.6}$$

Defining the spatial distribution of the Poynting vector as:

$$\tilde{\mathbf{s}}\left(\boldsymbol{\rho},z\right)=\frac{1}{2\zeta}\left|\mathbf{e}_0\left(\boldsymbol{\rho},z\right)\right|^2=S_0\left(z\right)\tilde{\mathbf{s}}_n\left(\boldsymbol{\rho},z\right) \tag{C.7}$$

where $S_0\left(z\right)=P_0/A_{laser}\left(z\right)$ is the peak amplitude of the pulse envelope of the Poynting vector in z, which is related to the peak power of the pulse P_0, $\tilde{\mathbf{s}}_n\left(\boldsymbol{\rho},z\right)$ is the spatial distribution of the Poynting vector with unitary amplitude, and

$$A_{laser}\left(z\right)=\int_{-\infty}^{+\infty}\int_{-\infty}^{+\infty}\tilde{\mathbf{s}}_n\left(\boldsymbol{\rho},z\right)\cdot\hat{\mathbf{z}}\,\mathrm{d}x\,\mathrm{d}y \tag{C.8}$$

is the area of the spatial distribution of the laser beam Poynting vector in z. The average power density carried by a laser pulse can be expressed as:

$$\tilde{\mathbf{s}}\left(\mathbf{r};t\right)=S_0\left(z\right)\tilde{\mathbf{s}}_n\left(\boldsymbol{\rho},z\right)\tilde{s}_n\left(t-\frac{z}{c}\right) \tag{C.9}$$

The remaining temporal dependence is associated with the modulating signal, $\tilde{s}_n\left(t\right)$. Assuming that the EM pulse travels along the negative z-direction, the average power carried each second by the EM pulse over a plane orthogonal to z is defined as:

$$\begin{aligned}p\left(z;t\right)=&\int_{-\infty}^{+\infty}\int_{-\infty}^{+\infty}\tilde{\mathbf{s}}\left(\boldsymbol{\rho},z;t\right)\cdot\left(-\hat{\mathbf{z}}\right)\mathrm{d}x\,\mathrm{d}y=\\&=S_0\left(z\right)\int_{-\infty}^{+\infty}\int_{-\infty}^{+\infty}\tilde{\mathbf{s}}_n\left(\boldsymbol{\rho},z\right)\cdot\left(-\hat{\mathbf{z}}\right)\mathrm{d}x\,\mathrm{d}y\,\tilde{s}_n\left(t-\frac{z}{c}\right)=\\&=P_0\tilde{s}_n\left(t-\frac{z}{c}\right)\end{aligned} \tag{C.10}$$

where P_0 is the peak power of the time-varying envelope of the pulsed signal with unitary amplitude $\tilde{s}_n\left(t\right)$.

By neglecting phase delay terms and assuming that $\tilde{s}_n(t)$ has the Gaussian shape:

$$\tilde{s}_n(t) = e^{-4\ln 2 \frac{t^2}{\tau_p^2}} \tag{C.11}$$

where τ_p is the full width at half maximum (FWHM) duration of the pulse, with $\tau_p \ll T_p$, one can relate the peak power of the pulse P_0 with the laser average power P_{ave} by the relation:

$$E_p = \sqrt{\frac{\pi}{4\ln 2}} P_0 \tau_p = P_{ave} T_p \tag{C.12}$$

where E_p is the energy of a single laser pulse. Assuming a given spatial transverse distribution (e.g., uniform, Gaussian, Airy pattern, etc.) for the laser electric field in z, and given a laser mean power P_{ave}, from (C.9)–(C.12) one can derive the amplitude $S_0(z)$ of the Poynting vector $\tilde{\mathbf{s}}(\mathbf{r};t)$ and the amplitude of the laser electric field $\mathbf{e}(\mathbf{r};t)$. As a numerical example, we can consider a laser beam with an average power $P_{ave} = 15\text{mW}$, a beam diameter at -3dB $D_{laser}(z) = 5\mu\text{m}$, a pulse duration $\tau_p = 100\text{fs}$, and a pulse repetition rate $f_p = 80\text{MHz}$. Each pulse of such laser carries an energy $E_p = 187.5\text{pJ}$, and the power peak of each pulse is $P_0 = 1.76\text{kW}$, according to (C.12). Resorting (C.10), the peak amplitude of the power density distribution is $S_0(z) = 62.18\text{W}/\mu\text{m}^2$, which corresponds to a peak amplitude of the electric field $E_0(z) = 216.38\text{V}/\mu\text{m}$, considering the laser beam propagates in the air.

Appendix D

Photoconductive Antennas Radiation Patterns

D.1 Primary Fields

The simulated radiation patterns inside the dielectric of the antenna geometries under analysis in Chapter 3 are shown in the following subsections.

D.1.1 Auston-Switch

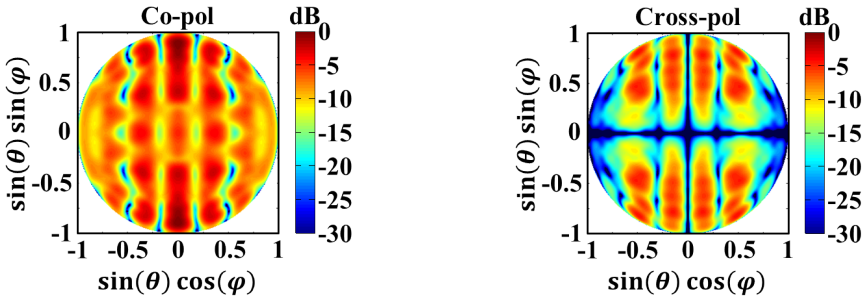

(a) $f = 0.1$THz

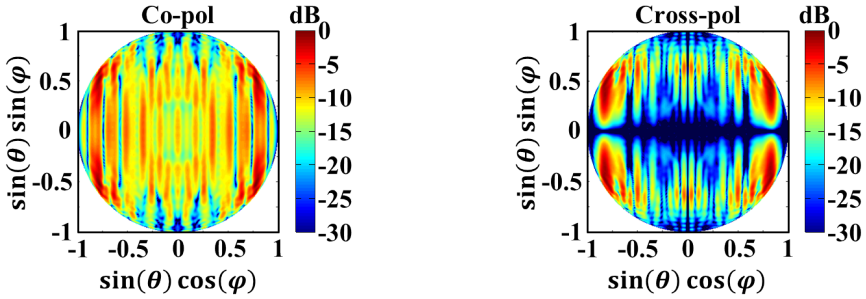

(b) $f = 0.5$THz

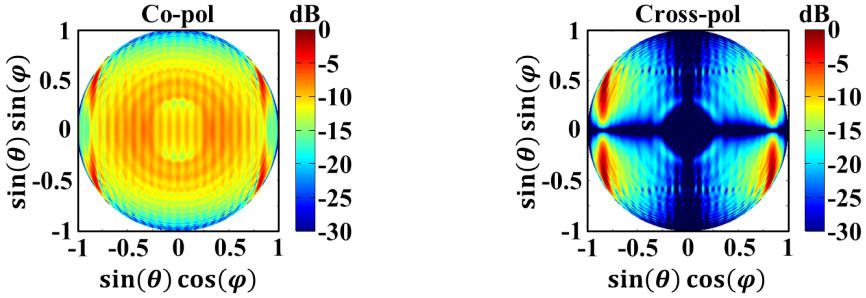

(c) $f = 1.0$THz

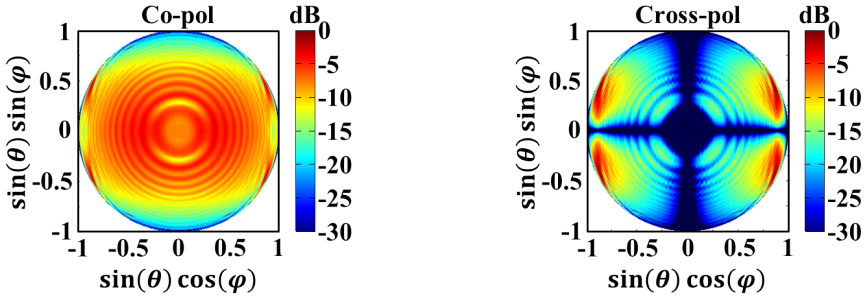

(d) $f = 1.5$THz

Figure D.1: 2D radiation patterns inside the dielectric radiated by the Auston-switch.

D.1.2 Bow-Tie

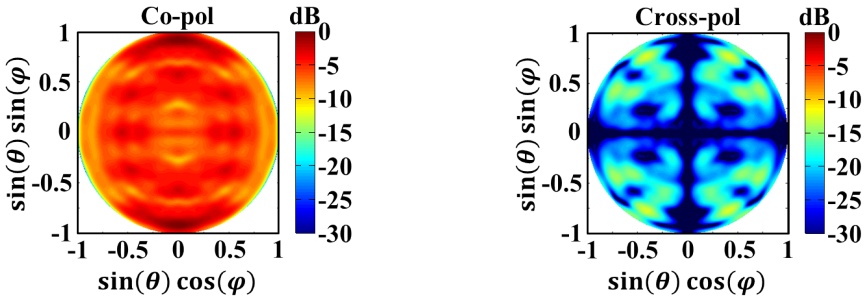

(a) $f = 0.1$THz

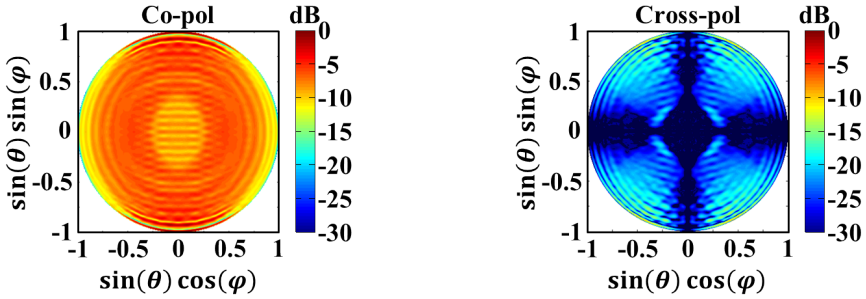

(b) $f = 0.5$THz

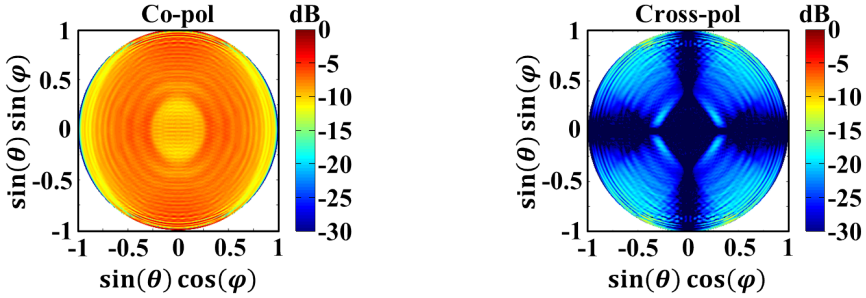

(c) $f = 1.0$THz

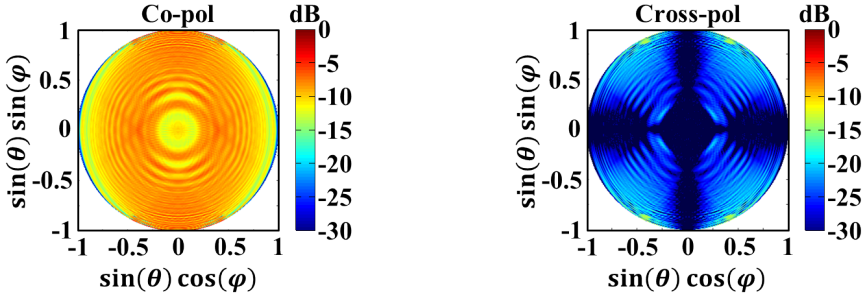

(d) $f = 1.5$THz

Figure D.2: 2D radiation patterns inside the dielectric radiated by the bow-tie antenna.

D.1.3 Logarithmic Spiral

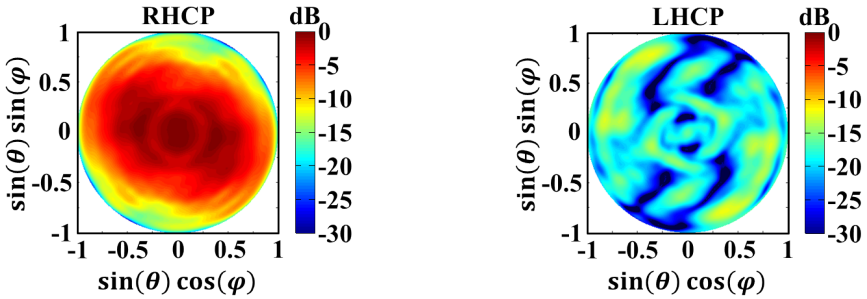

(a) $f = 0.1$THz

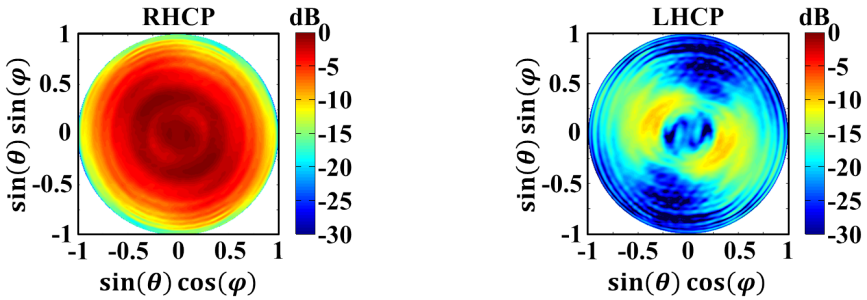

(b) $f = 0.5$THz

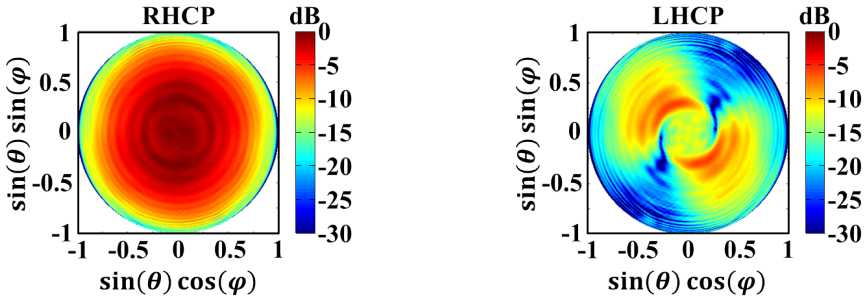

(c) $f = 1.0$THz

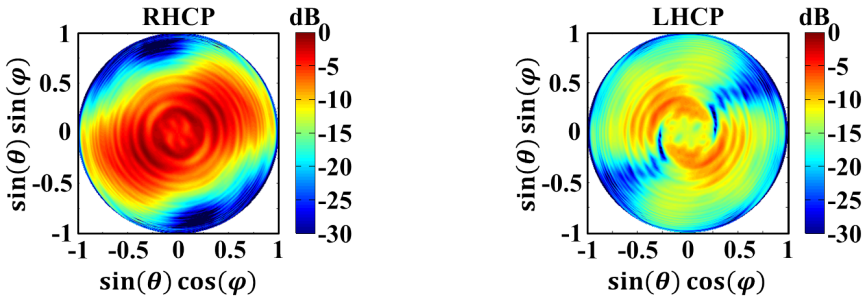

(d) $f = 1.5$THz

Figure D.3: 2D radiation patterns inside the dielectric radiated by the logarithmic spiral antenna.

D.2 Secondary Fields

The simulated radiation patterns radiated by the dielectric lens fed by the antenna geometries under analysis in Chapter 3 are shown in the following subsections.

D.2.1 Auston-Switch

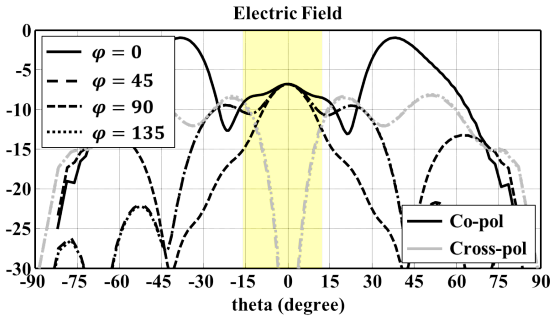

(a) $f = 0.1$THz

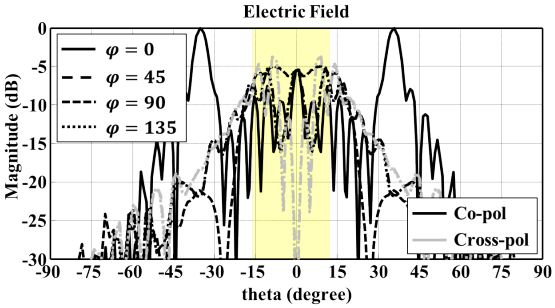

(b) $f = 0.5$THz

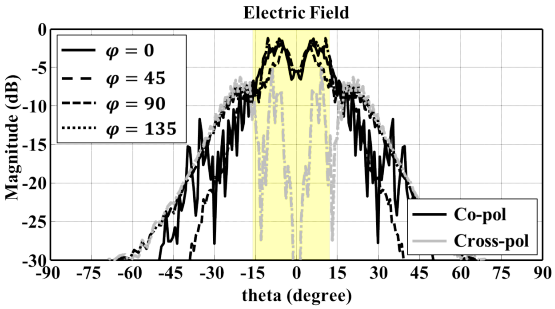

(c) $f = 1.0$THz

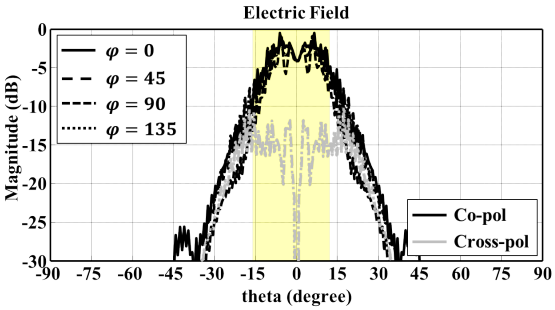

(d) $f = 1.5$THz

Figure D.4: Radiation patterns radiated by the dielectric lens fed by the Auston-switch. The yellow shaded region represents the angular region subtented by the area of the first reflector of the reflectors chain in the measurement setup described in Section 3.3.

D.2.2 Bow-Tie

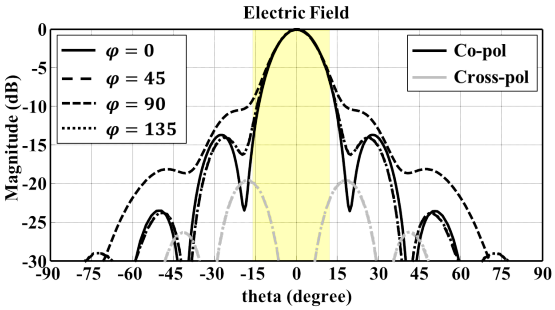

(a) $f = 0.1$THz

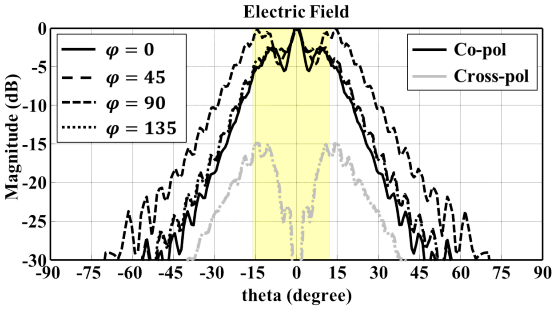

(b) $f = 0.5$THz

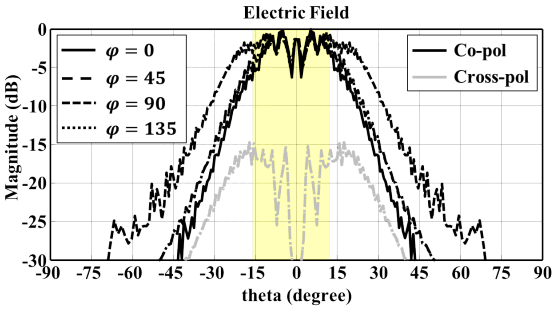

(c) $f = 1.0$THz

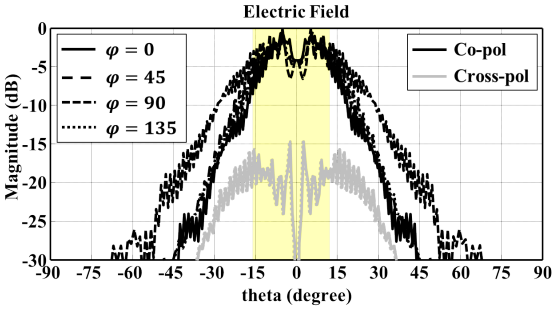

(d) $f = 1.5$THz

Figure D.5: Radiation patterns radiated by the dielectric lens fed by the bow-tie antenna. The yellow shaded region represents the angular region subtented by the area of the first reflector of the reflectors chain in the measurement setup described in Section 3.3.

D.2.3 Logarithmic Spiral

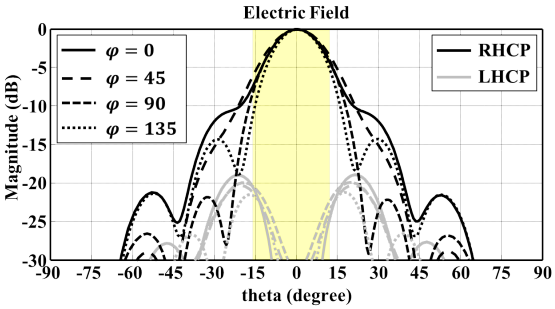

(a) $f = 0.1$THz

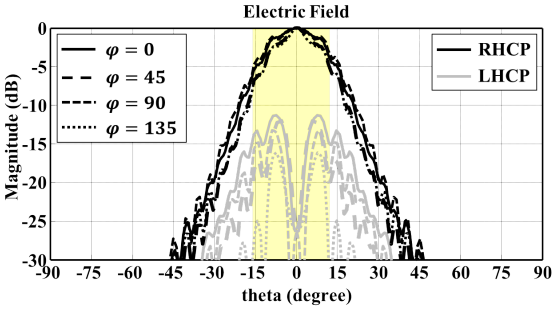

(b) $f = 0.5$THz

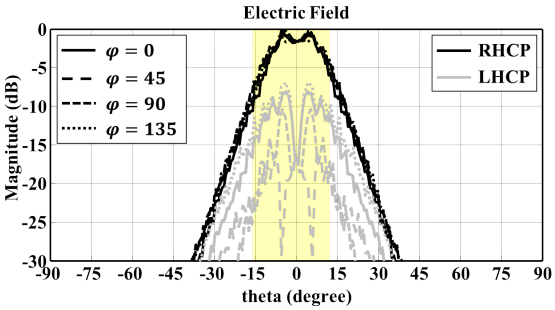

(c) $f = 1.0$THz

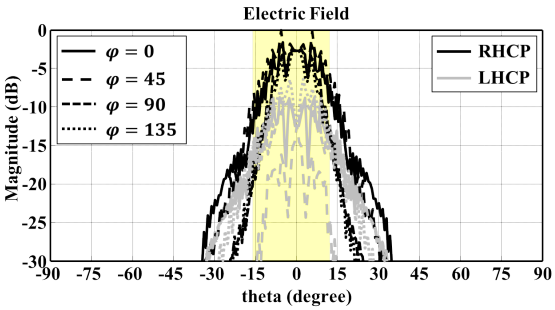

(d) $f = 1.5$THz

Figure D.6: Radiation patterns radiated by the dielectric lens fed by the logarithmic spiral antenna. The yellow shaded region represents the angular region subtented by the area of the first reflector of the reflectors chain in the measurement setup described in Section 3.3.

D.3 Tertiary Fields

The simulated radiation patterns outgoing from the reflectors chain fed by the dielectric lens antennas under analysis in Chapter 3 are shown in the following subsections.

D.3.1 Auston-Switch

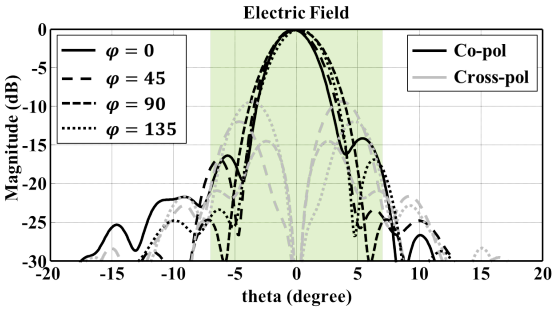

(a) $f = 0.1$THz

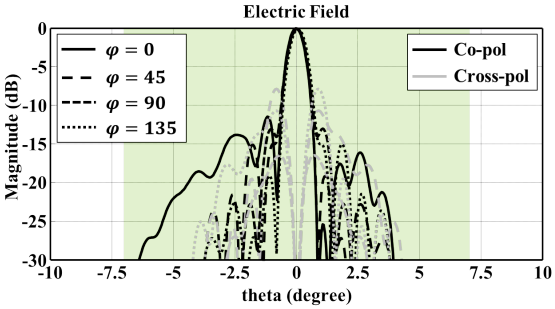

(b) $f = 0.5$THz

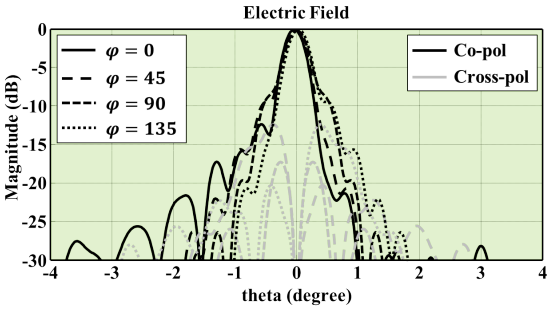

(c) $f = 1.0$THz

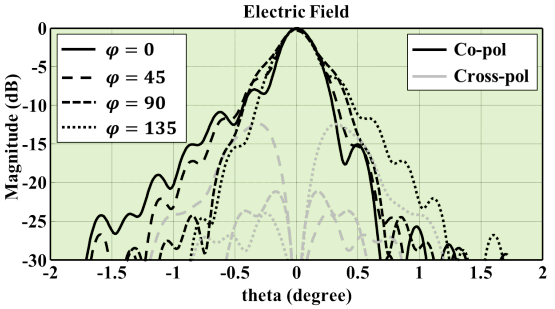

(d) $f = 1.5$THz

Figure D.7: Radiation patterns outgoing from the reflectors chain fed by Auston-switch lens antenna evaluated at the horn aperture. The green shaded region represents the angular region subtented by the horn aperture of the detector used in the measurement setup described in Section 4.3.

D.3.2 Bow-Tie

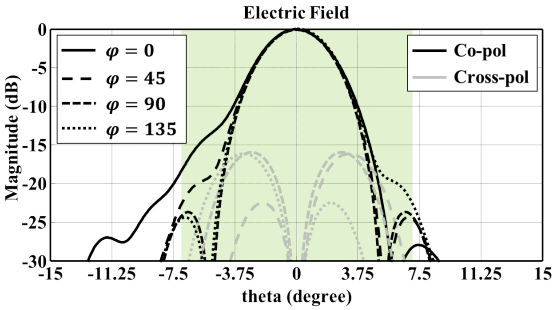

(a) $f = 0.1$THz

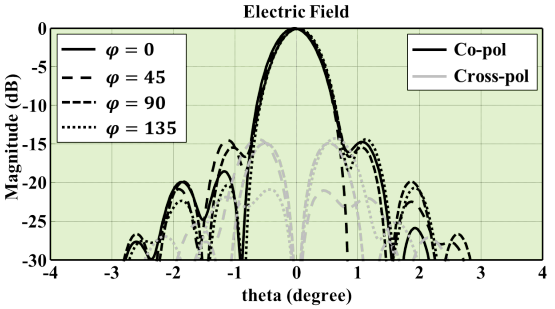

(b) $f = 0.5$THz

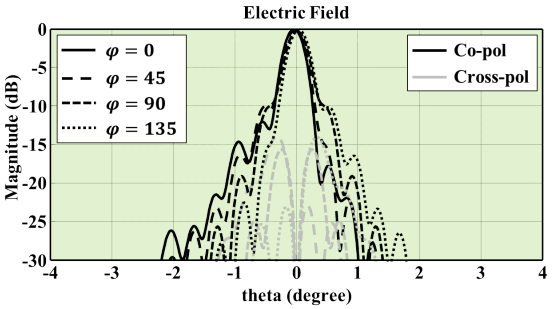

(c) $f = 1.0$THz

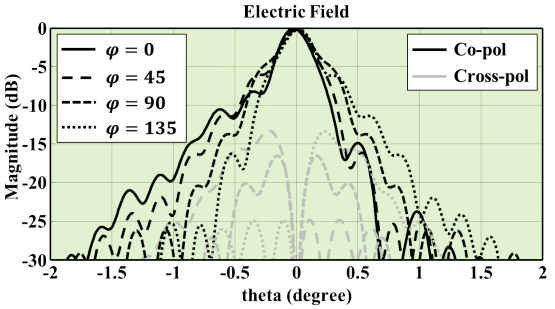

(d) $f = 1.5$THz

Figure D.8: Radiation patterns outgoing from the reflectors chain fed by bow-tie lens antenna evaluated at the horn aperture. The green shaded region represents the angular region subtented by horn aperture of the detector used in the measurement setup described in Section 4.3.

D.3.3 Logarithmic Spiral

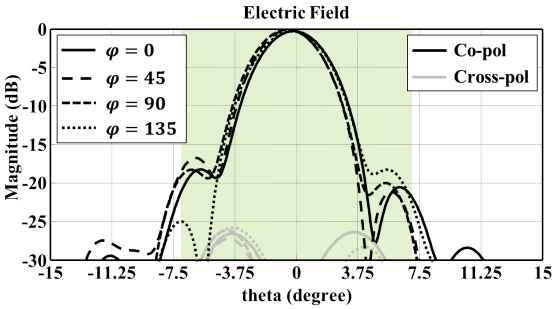

(a) $f = 0.1$THz

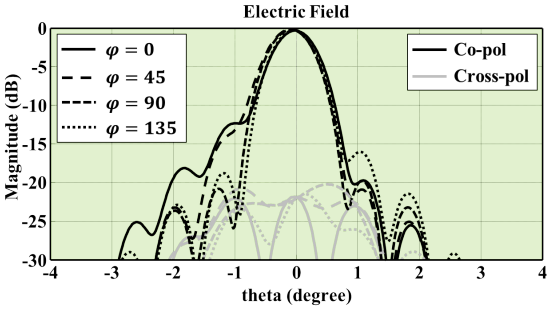

(b) $f = 0.5$THz

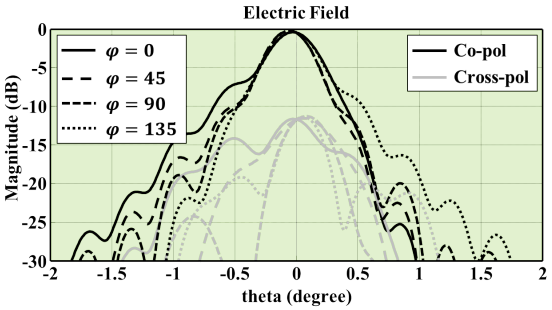

(c) $f = 1.0$THz

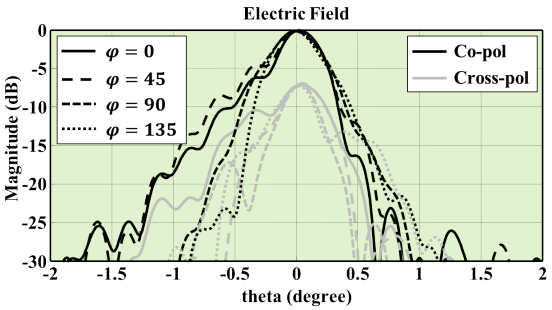

(d) $f = 1.5$THz

Figure D.9: Radiation patterns outgoing from the reflectors chain fed by logarithmic spiral lens antenna evaluated at the horn aperture. The green shaded region represents the angular region subtented by the horn aperture of the detector used in the measurement setup described in Section 4.3.

Appendix E

Characterization of the Power Meter used for the Measurements

The room temperature calorimetric power meter (VDI Erickson PM5 [100]) has been characterized before using it for the measurements. The characterization has been performed comparing the emitted power of a commercial photomixer (Toptica Terascan 1550 [42]) measured with the power detector [100] and the reference power provided by the manufacturer [146]. The measurements have been performed by coupling the photomixer to the detector with a reflectors chain (the same as used to characterize it by the manufacturer [146, 147]) and scanning the frequency of the source over its bandwidth (i.e. $0.1\text{THz} - 1\text{THz}$). The setup used for the characterization of the detector is depicted in Fig. E.1, a 5mm thick filter screen of Polytetrafluoroethylene (PTFE) was placed between the second reflector and the detector, in order to screen possible InfraRed (IR) power coming from the source (this screen is not depicted in Fig. E.1). Because of the low level of power at the higher frequency, the measurements have been acquired by the off-on-off measurement procedure suggested by the manufacturer of the detector [100, 105].

The comparison between the average of the measured power at each frequency by the power meter and the reference power curve provided by the manufacturer is shown in Fig. E.2. The plot shows also the error bar at six standard deviations centered at the average of the measurements at each frequency. Since the reference power was measured with a different detector [147], in order to have a fair comparison, the measurements have been corrected for the coupling efficiency η_d of the detector [100]. The QO channel [146–148] has been analyzed as discussed in Chapter 4 and the efficiency η_d has been evaluated. Multiple measurements at each frequency have been acquired, an average of the measurements and its standard deviation at each frequency have been calculated. Fig. E.2 shows a good agreement between the curves, thus providing a solid characterization of the power meter and, moreover, a further validation of the electromagnetic model of the channel proposed in this work.

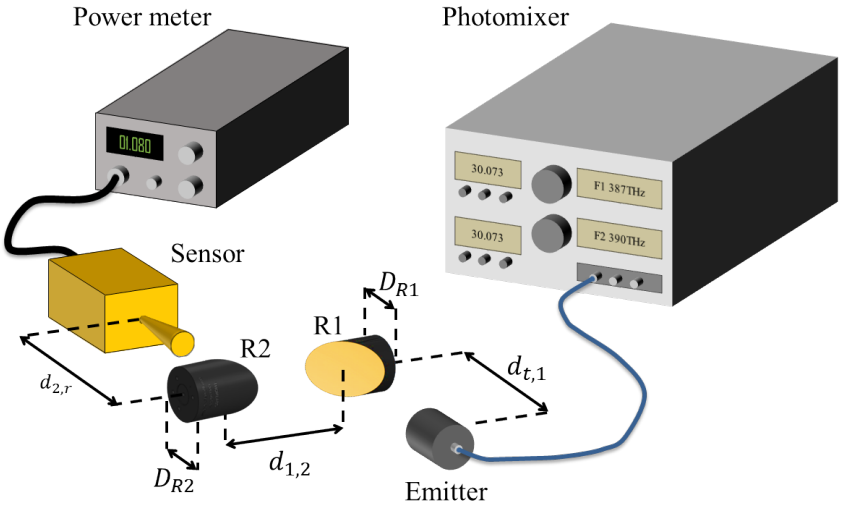

Figure E.1: Setup for the characterization of the power meter used for the measurements of the power radiated by the PCA prototypes discussed in Chapter 4.

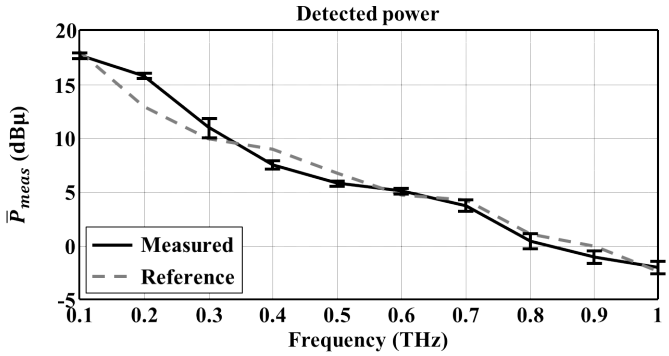

Figure E.2: Comparison between the power measured by the detector [100] and the reference curve of the detected power provided by the manufacturer [42, 146].

Bibliography

[1] P.U. Jepsen, D.G. Cooke, and M. Koch, "Terahertz spectroscopy and imaging modern techniques and applications," *Laser & Photonics Reviews*, vol. 5, no. 1, pp. 124–166, Jan. 2011.

[2] D. Saeedkia, Ed., *Handbook of Terahertz Technology for Imaging, Sensing and Communications*, Woodhead Publishing Series in Electronic and Optical Materials. Elsevier Science, 2013.

[3] M. Tonouchi, "Cutting-edge terahertz technology," *Nature Photonics*, vol. 1, no. 2, pp. 97–105, Feb. 2007.

[4] M. Hangyo, M. Tani, T. Nagashima, H. Kitahara, and H. Sumikura, "Spectroscopy and imaging by laser excited terahertz waves," *Plasma and Fusion Research*, vol. 2, pp. S1020:1–7, Nov. 2007.

[5] P. F. Taday, "Applications of terahertz spectroscopy to pharmaceutical sciences," *Philosophical Transactions of the Royal Society of London A: Mathematical, Physical and Engineering Sciences*, vol. 362, no. 1815, pp. 351–364, Feb. 2004.

[6] T. Globus, D. Woolard, M. Bykhovskaia, B. Gelmont, L. Werbos, and A. Samuels, "THz-frequency spectroscopic sensing of DNA and related biological materials," *International Journal of High Speed Electronics and Systems*, vol. 13, no. 04, pp. 903–936, Dec. 2003.

[7] J. F Federici, B. Schulkin, F. Huang, D. Gary, R. Barat, F. Oliveira, and D. Zimdars, "THz imaging and sensing for security applications, explosives, weapons and drugs," *Semiconductor Science and Technology*, vol. 20, no. 7, pp. S266–S280, Jul. 2005.

[8] M. K. Choi, A. Bettermann, and D. W. van der Weide, "Potential for detection of explosive and biological hazards with electronic terahertz systems," *Philosophical Transactions of the Royal Society of London A: Mathematical, Physical and Engineering Sciences*, vol. 362, no. 1815, pp. 337–349, Feb. 2004.

[9] M. C. Kemp, P. F. Taday, B. E. Cole, J. A. Cluff, A. J. Fitzgerald, and W. R. Tribe, "Security applications of terahertz technology," in *Terahertz for Military and Security Applications*, Apr. 2003, vol. 5070 of *Proceedings SPIE*, pp. 44–52.

[10] P. H. Siegel, "Terahertz technology in biology and medicine," *IEEE Transactions on Microwave Theory and Techniques*, vol. 52, no. 10, pp. 2438–2447, Oct. 2004.

[11] D. Mittleman, Ed., *Sensing with Terahertz Radiation*, vol. 85 of *Springer Series in Optical Sciences*, Springer-Verlag Berlin Heidelberg, 2003.

[12] K. Baaske, M. Salhi, F. Rutz, T. Hasek, R. Wilk, H. Richter, and M. Koch, "Mail inspection using THz imaging: a comparison of three different systems," in *Terahertz for Military and Security Applications*, May 2006, vol. 6212 of *Proceedings SPIE*, pp. 62120U:1–11.

[13] H. Hoshina, Y. Sasaki, A. Hayashi, C. Otani, and K. Kawase, "Noninvasive mail inspection system with terahertz radiation," *Applied Spectroscopy*, vol. 63, no. 1, pp. 81–86, Jan. 2009.

[14] N. Krumbholz, T. Hochrein, N. Vieweg, T. Hasek, K. Kretschmer, M. Bastian, M. Mikulics, and M. Koch, "Monitoring polymeric compounding processes inline with THz time-domain spectroscopy," *Polymer Testing*, vol. 28, no. 1, pp. 30–35, Feb. 2009.

[15] F. Rutz, M. Koch, S. Khare, M. Moneke, H. Richter, and U. Ewert, "Terahertz quality control of polymeric products," *International Journal of Infrared and Millimeter Waves*, vol. 27, no. 4, pp. 547–556, Apr. 2006.

[16] A.Y. Cho and J.R. Arthur, "Molecular beam epitaxy," *Progress in Solid State Chemistry*, vol. 10, pp. 157–191, 1975.

[17] P. R. Smith, D. H. Auston, A. M. Johnson, and W. M. Augustyniak, "Picosecond photoconductivity in radiationdamaged silicononsapphire films," *Applied Physics Letters*, vol. 38, no. 1, pp. 47–50, Jan. 1981.

[18] D. H. Auston, K. P. Cheung, and P. R. Smith, "Picosecond photoconducting hertzian dipoles," *Applied Physics Letters*, vol. 45, no. 3, pp. 284–286, Aug. 1984.

[19] M. C. Nuss, D. H. Auston, and F. Capasso, "Direct subpicosecond measurement of carrier mobility of photoexcited electrons in gallium arsenide," *Physical Review Letters*, vol. 58, pp. 2355–2358, Jun. 1987.

[20] P. R. Smith, D. H. Auston, and M. C. Nuss, "Subpicosecond photoconducting dipole antennas," *IEEE Journal of Quantum Electronics*, vol. 24, no. 2, pp. 255–260, Feb. 1988.

[21] B. B. Hu, X.C. Zhang, and D. H. Auston, "Temperature dependence of femtosecond electromagnetic radiation from semiconductor surfaces," *Applied Physics Letters*, vol. 57, no. 25, pp. 2629–2631, Dec. 1990.

[22] X.C. Zhang and D. H. Auston, "Optoelectronic measurement of semiconductor surfaces and interfaces with femtosecond optics," *Journal of Applied Physics*, vol. 71, no. 1, pp. 326–338, Jan. 1992.

[23] I. S. Gregory, C. Baker, W. R. Tribe, M. J. Evans, H. E. Beere, E. H. Linfield, A. G. Davies, and M. Missous, "High resistivity annealed low-temperature GaAs with 100 fs lifetimes," *Applied Physics Letters*, vol. 83, no. 20, pp. 4199–4201, Nov. 2003.

[24] A. Neto and J. J. Lee, ""infinite bandwidth" long slot array antenna," *IEEE Antennas and Wireless Propagation Letters*, vol. 4, pp. 75–78, Jun. 2005.

[25] A. Neto and J. J. Lee, "Ultrawide-band properties of long slot arrays," *IEEE Transactions on Antennas and Propagation*, vol. 54, no. 2, pp. 534–543, Feb. 2006.

[26] A. Neto, D. Cavallo, G. Gerini, and G. Toso, "Scanning performances of wideband connected arrays in the presence of a backing reflector," *IEEE Transactions on Antennas and Propagation*, vol. 57, no. 10, pp. 3092–3102, Oct 2009.

[27] D. Cavallo, A. Neto, and G. Gerini, "Green's function based equivalent circuits for connected arrays in transmission and in reception," *IEEE Transactions on Antennas and Propagation*, vol. 59, no. 5, pp. 1535–1545, May 2011.

[28] D. Cavallo and A. Neto, "A connected array of slots supporting broadband leaky waves," *IEEE Transactions on Antennas and Propagation*, vol. 61, no. 4, pp. 1986–1994, April 2013.

[29] O. Yurduseven, D. Cavallo, and A. Neto, "Wideband dielectric lens antenna with stable radiation patterns fed by coherent array of connected leaky slots," *IEEE Transactions on Antennas and Propagation*, vol. 62, no. 4, pp. 1895–1902, Apr. 2014.

[30] O. Yurduseven, D. Cavallo, A. Neto, G. Carluccio, and M. Albani, "Parametric analysis of extended hemispherical dielectric lenses fed by a broadband connected array of leaky-wave slots," *IET Microwaves, Antennas Propagation*, vol. 9, no. 7, pp. 611–617, May 2015.

[31] S. Preu, G. H. Dhler, S. Malzer, L. J. Wang, and A. C. Gossard, "Tunable, continuous-wave terahertz photomixer sources and applications," *Journal of Applied Physics*, vol. 109, no. 6, pp. 061301:1–55, Mar. 2011.

[32] A. C. Warren, J. M. Woodall, J. L. Freeouf, D. Grischkowsky, D. T. McInturff, M. R. Melloch, and N. Otsuka, "Arsenic precipitates and the semiinsulating properties of GaAs buffer layers grown by lowtemperature molecular beam epitaxy," *Applied Physics Letters*, vol. 57, no. 13, pp. 1331–1333, Sept. 1990.

[33] S. Gupta, M. Y. Frankel, J. A. Valdmanis, J. F. Whitaker, G. A. Mourou, F. W. Smith, and A. R. Calawa, "Subpicosecond carrier lifetime in GaAs grown by molecular beam epitaxy at low temperatures," *Applied Physics Letters*, vol. 59, no. 25, pp. 3276–3278, Dec. 1991.

[34] C. Baker, I. S. Gregory, W. R. Tribe, I. V. Bradley, M. J. Evans, E. H. Linfield, and M. Missous, "Highly resistive annealed low-temperature-grown InGaAs with sub-500fs carrier lifetimes," *Applied Physics Letters*, vol. 85, no. 21, pp. 4965–4967, Nov. 2004.

[35] J. Sigmund, C. Sydlo, H. L. Hartnagel, N. Benker, H. Fuess, F. Rutz, T. Kleine-Ostmann, and M. Koch, "Structure investigation of low-temperature-grown GaAsSb, a material for photoconductive terahertz antennas," *Applied Physics Letters*, vol. 87, no. 25, pp. 252103:1–3, Dec. 2005.

[36] B. Sartorius, H. Roehle, H. Künzel, J. Böttcher, M. Schlak, D. Stanze, H. Venghaus, and M. Schell, "All-fiber terahertz time-domain spectrometer operating at 1.5μm telecom wavelengths," *Optics Express*, vol. 16, no. 13, pp. 9565–9570, Jun 2008.

[37] H. Roehle, R. J. B. Dietz, H. J. Hensel, J. Böttcher, H. Künzel, D. Stanze, M. Schell, and B. Sartorius, "Next generation 1.5μm terahertz antennas: mesa-structuring of InGaAs/InAlAs photoconductive layers," *Optics Express*, vol. 18, no. 3, pp. 2296–2301, Feb. 2010.

[38] J. Valdmanis and G. Mourou, "Subpicosecond electrooptic sampling: Principles and applications," *IEEE Journal of Quantum Electronics*, vol. 22, no. 1, pp. 69–78, Jan. 1986.

[39] "Picometrix a LUNA company," Ann Arbor, Michigan, United States.

[40] "Teraview Ltd.," Cambridge, United Kingdom.

[41] "Menlo Systems GmbH," Martinsried Germany.

[42] "TOPTICA Photonics AG," Munich, Germany.

[43] M. B. Ketchen, D. Grischkowsky, T. C. Chen, CC. Chi, I. N. Duling III, N. J. Halas, JM. Halbout, J. A. Kash, and G. P. Li, "Generation of subpicosecond electrical pulses on coplanar transmission lines," *Applied Physics Letters*, vol. 48, no. 12, pp. 751–753, Mar. 1986.

[44] M. van Exter and D. R. Grischkowsky, "Characterization of an optoelectronic terahertz beam system," *IEEE Transactions on Microwave Theory and Techniques*, vol. 38, no. 11, pp. 1684–1691, Nov. 1990.

[45] D. R. Dykaar, B. I. Greene, J. F. Federici, A. F. J. Levi, L. N. Pfeiffer, and R. F. Kopf, "Log-periodic antennas for pulsed terahertz radiation," *Applied Physics Letters*, vol. 59, no. 3, pp. 262–264, Jul. 1991.

[46] M. M. Gitin, F. W. Wise, G. Arjavalingam, Y. Pastol, and R. C. Compton, "Broadband characterization of millimeter-wave log-periodic antennas by photoconductive sampling," *IEEE Transactions on Antennas and Propagation*, vol. 42, no. 3, pp. 335–339, Mar 1994.

[47] R. Mendis, C. Sydlo, J. Sigmund, M. Feiginov, P. Meissner, and H. L. Hartnagel, "Tunable CW-THz system with a log-periodic photoconductive emitter," in *International Semiconductor Device Research Symposium, 2003*, Dec 2003, pp. 318–319.

[48] E. R. Brown, A. W. M. Lee, B. S. Navi, and J. E. Bjarnason, "Characterization of a planar self-complementary square-spiral antenna in the THz region," *Microwave and Optical Technology Letters*, vol. 48, no. 3, pp. 524–529, Mar. 2006.

[49] Z. D. Taylor, E. R. Brown, J. E. Bjarnason, M. P. Hanson, and A. C. Gossard, "Resonant-optical-cavity photoconductive switch with 0.5% conversion efficiency and 1.0W peak power," *Optics Letters*, vol. 31, no. 11, pp. 1729–1731, Jun 2006.

[50] J. Y. Suen, W. Li, Z. D. Taylor, and E. R. Brown, "Characterization and modeling of a terahertz photoconductive switch," *Applied Physics Letters*, vol. 96, no. 14, pp. 141103, 2010.

[51] S. H. Yang, M. R. Hashemi, C. W. Berry, and M. Jarrahi, "7.5% optical-to-terahertz conversion efficiency offered by photoconductive emitters with three-dimensional plasmonic contact electrodes," *IEEE Transactions on Terahertz Science and Technology*, vol. 4, no. 5, pp. 575–581, Sept. 2014.

[52] C. W. Berry, M. R. Hashemi, and M. Jarrahi, "Generation of high power pulsed terahertz radiation using a plasmonic photoconductive emitter array with logarithmic spiral antennas," *Applied Physics Letters*, vol. 104, no. 8, pp. 081122, Feb. 2014.

[53] H. Ito, T. Yoshimatsu, H. Yamamoto, and T. Ishibashi, "Broadband photonic terahertz-wave emitter integrating uni-traveling-carrier photodiode and self-complementary planar antenna," *Optical Engineering*, vol. 53, no. 3, pp. 031209, Mar. 2014.

[54] N. Llombart and A. Neto, "THz time-domain sensing: The antenna dispersion problem and a possible solution," *IEEE Transactions on Terahertz Science and Technology*, vol. 2, no. 4, pp. 416–423, Jul. 2012.

[55] J. T. Darrow, X. C. Zhang, and D. H. Auston, "Power scaling of large-aperture photoconducting antennas," *Applied Physics Letters*, vol. 58, no. 1, pp. 25–27, Jan. 1991.

[56] J. T. Darrow, X. C. Zhang, D. H. Auston, and J. D. Morse, "Saturation properties of large-aperture photoconducting antennas," *IEEE Journal of Quantum Electronics*, vol. 28, no. 6, pp. 1607–1616, Jun. 1992.

[57] M. Tani, S. Matsuura, K. Sakai, and S. Nakashima, "Emission characteristics of photoconductive antennas based on low-temperature-grown GaAs and semi-insulating GaAs," *Applied Optics*, vol. 36, no. 30, pp. 7853–7859, Oct. 1997.

[58] P. K. Benicewicz, J. P. Roberts, and A. J. Taylor, "Scaling of terahertz radiation from large-aperture biased photoconductors," *Journal of the Optics Society of America B*, vol. 11, no. 12, pp. 2533–2546, Dec. 1994.

[59] D. S. Kim and D. S. Citrin, "Coulomb and radiation screening in photoconductive terahertz sources," *Applied Physics Letters*, vol. 88, no. 16, pp. 161117, Apr. 2006.

[60] J. T. Darrow, B. B. Hu, X.-C. Zhang, and D. H. Auston, "Subpicosecond electromagnetic pulses from large-aperture photoconducting antennas," *Optics Letters*, vol. 15, no. 6, pp. 323–325, Mar. 1990.

[61] B. B. Hu, J. T. Darrow, X.C. Zhang, D. H. Auston, and P. R. Smith, "Optically steerable photoconducting antennas," *Applied Physics Letters*, vol. 56, no. 10, pp. 886–888, Mar. 1990.

[62] H. Yoneda, K. Tokuyama, K. Ueda, H. Yamamoto, and K. Baba, "High-power terahertz radiation emitter with a diamond photoconductive switch array," *Applied Optics*, vol. 40, no. 36, pp. 6733–6736, Dec. 2001.

[63] N. M. Froberg, Bin Bin Hu, Xi-Cheng Zhang, and D. H. Auston, "Terahertz radiation from a photoconducting antenna array," *IEEE Journal of Quantum Electronics*, vol. 28, no. 10, pp. 2291–2301, Oct. 1992.

[64] A. Dreyhaupt, S. Winnerl, T. Dekorsy, and M. Helm, "High-intensity terahertz radiation from a microstructured large-area photoconductor," *Applied Physics Letters*, vol. 86, no. 12, pp. 121114, Mar. 2005.

[65] T. Hattori, K. Egawa, S. Ookuma, and T. Itatani, "Intense terahertz pulses from large-aperture antenna with interdigitated electrodes," *Japanese Journal of Applied Physics*, vol. 45, no. 15, pp. L422–L424, Apr. 2006.

[66] M. Awad, M. Nagel, H. Kurz, J. Herfort, and K. Ploog, "Characterization of low temperature GaAs antenna array terahertz emitters," *Applied Physics Letters*, vol. 91, no. 18, pp. 181124, Oct. 2007.

[67] S. Winnerl, F. Peter, S. Nitsche, A. Dreyhaupt, B. Zimmermann, M. Wagner, H. Schneider, M. Helm, and K. Kohler, "Generation and detection of THz radiation with scalable antennas based on GaAs substrates with different carrier life-

times," *IEEE Journal of Selected Topics in Quantum Electronics*, vol. 14, no. 2, pp. 449–457, Mar. 2008.

[68] G. Matthäus, S. Nolte, R. Hohmuth, M. Voitsch, W. Richter, B. Pradarutti, S. Riehemann, G. Notni, and A. Tünnermann, "Microlens coupled interdigital photoconductive switch," *Applied Physics Letters*, vol. 93, no. 9, pp. 091110, Sept. 2008.

[69] H. F. Tiedje, D. Saeedkia, M. Nagel, and H. K. Haugen, "Optical scanning techniques for characterization of terahertz photoconductive antenna arrays," *IEEE Transactions on Microwave Theory and Techniques*, vol. 58, no. 7, pp. 2040–2045, Jul. 2010.

[70] S. Preu, M. Mittendorff, H. Lu, H. B. Weber, S. Winnerl, and A. C. Gossard, "1550nm ErAs:In(Al)GaAs large area photoconductive emitters," *Applied Physics Letters*, vol. 101, no. 10, pp. 101105, Sept. 2012.

[71] M. Mittendorff, M. Xu, R. J B Dietz, H. Künzel, B. Sartorius, H. Schneider, M. Helm, and S. Winnerl, "Large area photoconductive terahertz emitter for 1.55μm excitation based on an InGaAs heterostructure," *Nanotechnology*, vol. 24, no. 21, pp. 214007, May 2013.

[72] P. J. Hale, J. Madeo, C. Chin, S. S. Dhillon, J. Mangeney, J. Tignon, and K. M. Dani, "20 THz broadband generation using semi-insulating GaAs interdigitated photoconductive antennas," *Optics Express*, vol. 22, no. 21, pp. 26358–26364, Oct. 2014.

[73] A. Singh and S. S. Prabhu, "Microlensless interdigitated photoconductive terahertz emitters," *Optics Express*, vol. 23, no. 2, pp. 1529–1535, Jan. 2015.

[74] N. T. Yardimci, S. H. Yang, C. W. Berry, and M. Jarrahi, "High-power terahertz generation using large-area plasmonic photoconductive emitters," *IEEE Transactions on Terahertz Science and Technology*, vol. 5, no. 2, pp. 223–229, Mar. 2015.

[75] I. S. Gregory, C. Baker, W. R. Tribe, I. V. Bradley, M. J. Evans, E. H. Linfield, A. G. Davies, and M. Missous, "Optimization of photomixers and antennas for continuous-wave terahertz emission," *IEEE Journal of Quantum Electronics*, vol. 41, no. 5, pp. 717–728, May 2005.

[76] E. R. Brown, "THz generation by photomixing in ultrafast photoconductors," *International Journal of High Speed Electronics and Systems*, vol. 13, no. 2, pp. 497–545, Jun. 2003.

[77] Gabriel C. Loata, Mark D. Thomson, Torsten Löffler, and Hartmut G. Roskos, "Radiation field screening in photoconductive antennae studied via pulsed terahertz emission spectroscopy," *Applied Physics Letters*, vol. 91, no. 23, pp. 232506, Dec. 2007.

[78] N. Khiabani, Y. Huang, Y. C. Shen, and S. Boyes, "Theoretical modeling of a photoconductive antenna in a terahertz pulsed system," *IEEE Transactions on Antennas and Propagation*, vol. 61, no. 4, pp. 1538–1546, Apr. 2013.

[79] S. Ramo, J. R. Whinnery, and T. Van Duzer, *Fields and waves in communication electronics*, Wiley & Sons Inc., 3rd edition, 1994.

[80] D. G Rowe, "Terahertz takes to the stage," *Nature Photonics*, vol. 1, no. 2, pp. 75–77, Feb. 2007.

[81] J. W. Bowen, "Towards terahertz communications - systems requirements," in *Terahertz Sources and Systems*, R. E. Miles, P. Harrison, and D. Lippens, Eds., pp. 269–283. Springer Netherlands, 2001.

[82] D. Grischkowsky, Søren Keiding, Martin van Exter, and Ch. Fattinger, "Far-infrared time-domain spectroscopy with terahertz beams of dielectrics and semiconductors," *Journal of the Optical Society of America B*, vol. 7, no. 10, pp. 2006–2015, Oct. 1990.

[83] P. U. Jepsen, R. H. Jacobsen, and S. R. Keiding, "Generation and detection of terahertz pulses from biased semiconductor antennas," *Journal of the Optical Society of America B*, vol. 13, no. 11, pp. 2424–2436, Nov. 1996.

[84] S. Verghese, K. A. McIntosh, and E. R. Brown, "Highly tunable fiber-coupled photomixers with coherent terahertz output power," *IEEE Transactions on Microwave Theory and Techniques*, vol. 45, no. 8, pp. 1301–1309, Aug. 1997.

[85] L. Duvillaret, F. Garet, J. F. Roux, and J. L. Coutaz, "Analytical modeling and optimization of terahertz time-domain spectroscopy experiments, using photoswitches as antennas," *IEEE Journal of Selected Topics in Quantum Electronics*, vol. 7, no. 4, pp. 615–623, Jul. 2001.

[86] C. W. Berry and M. Jarrahi, "Principles of impedance matching in photoconductive antennas," *Journal of Infrared, Millimeter, and Terahertz Waves*, vol. 33, no. 12, pp. 1182–1189, Dec. 2012.

[87] S. Gupta, J. F. Whitaker, and G. A. Mourou, "Ultrafast carrier dynamics in III-V semiconductors grown by molecular-beam epitaxy at very low substrate temperatures," *IEEE Journal of Quantum Electronics*, vol. 28, no. 10, pp. 2464–2472, Oct. 1992.

[88] D. C. Look, D. C. Walters, G. D. Robinson, J. R. Sizelove, M. G. Mier, and C. E. Stutz, "Annealing dynamics of molecular-beam epitaxial GaAs grown at 200°C," *Journal of Applied Physics*, vol. 74, no. 1, pp. 306–310, Jul. 1993.

[89] V. Ortiz, J. Nagle, J.-F. Lampin, E. Péronne, and A. Alexandrou, "Low-temperature-grown GaAs: Modeling of transient reflectivity experiments," *Journal of Applied Physics*, vol. 102, no. 4, pp. 043515, Aug. 2007.

[90] M. C. Beard, G. M. Turner, and C. A. Schmuttenmaer, "Subpicosecond carrier dynamics in low-temperature grown GaAs as measured by time-resolved terahertz spectroscopy," *Journal of Applied Physics*, vol. 90, no. 12, pp. 5915–5923, Dec. 2001.

[91] S. S. Prabhu, S. E. Ralph, M. R. Melloch, and E. S. Harmon, "Carrier dynamics of low-temperature-grown GaAs observed via THz spectroscopy," *Applied Physics Letters*, vol. 70, no. 18, pp. 2419–2421, May 1997.

[92] J. Shan and T. F. Heinz, "Terahertz radiation from semiconductors," in *Ultrafast Dynamical Processes in Semiconductors*, K.-T. Tsen, Ed., vol. 92 of *Topics in Applied Physics*, pp. 1–56. Springer-Verlag Berlin Heidelberg, 2004.

[93] G. C. Loata, *Investigation of low-temperature-grown GaAs photoconductive antennae for continuous-wave and pulsed terahertz generation*, Ph.D. thesis, Goethe-University, Frankfurt am Main, 2007.

[94] "CST Microwave Studio 2012," Available: http://www.cst.com.

[95] D. F. Filipovic, S. S. Gearhart, and G. M. Rebeiz, "Double-slot antennas on extended hemispherical and elliptical silicon dielectric lenses," *IEEE Transactions on Microwave Theory and Techniques*, vol. 41, no. 10, pp. 1738–1749, Oct. 1993.

[96] A. Ludwig, "The definition of cross polarization," *IEEE Transactions on Antennas and Propagation*, vol. 21, no. 1, pp. 116–119, Jan. 1973.

[97] A. Neto and S. Maci, "Green's function for an infinite slot printed between two homogeneous dielectrics–Part I: Magnetic currents," *IEEE Transactions on Antennas and Propagation*, vol. 51, no. 7, pp. 1572–1581, Jul. 2003.

[98] S. Maci and A. Neto, "Green's function of an infinite slot printed between two homogeneous dielectrics–Part II: uniform asymptotic solution," *IEEE Transactions on Antennas and Propagation*, vol. 52, no. 3, pp. 666–676, Mar. 2004.

[99] P. H. Bolivar, M. Brucherseifer, J. G. Rivas, R. Gonzalo, I. Ederra, A. L. Reynolds, M. Holker, and P. de Maagt, "Measurement of the dielectric constant and loss tangent of high dielectric-constant materials at terahertz frequencies," *IEEE Transactions on Microwave Theory and Techniques*, vol. 51, no. 4, pp. 1062–1066, Apr. 2003.

[100] "Virginia Diodes Inc.," Charlottesville, Virginia, United States.

[101] "CST Microwave Studio 2012," Available: http://www.ticra.com.

[102] "QMC Instruments Ltd.," Cardiff, United Kingdom.

[103] A. Garufo, G. Carluccio, N. Llombart, and A. Neto, "Design of photoconductive connected arrays for pulsed terahertz radiation," in *10th European Conference on Antennas and Propagation (EUCAP 2016)*, Apr. 2016, Davos, Switzerland.

[104] "Thomas Keating Instruments Ltd.," Billingshurst, United Kingdom.

[105] J. Hesler, "Personal communication," June 2016.

[106] Y.-S. Lee, Ed., *Principles of Terahertz Science and Technology*, Springer US, 2009.

[107] D. Rutledge and M. Muha, "Imaging antenna arrays," *IEEE Transactions on Antennas and Propagation*, vol. 30, no. 4, pp. 535–540, Jul. 1982.

[108] R. Compton, R. McPhedran, Z. Popovic, G. Rebeiz, P. Tong, and D. Rutledge, "Bow-tie antennas on a dielectric half-space: Theory and experiment," *IEEE Transactions on Antennas and Propagation*, vol. 35, no. 6, pp. 622–631, Jun. 1987.

[109] X. Wu, G. V. Eleftheriades, and T. E. van Deventer-Perkins, "Design and characterization of single- and multiple-beam mm-wave circularly polarized substrate lens antennas for wireless communications," *IEEE Transactions on Microwave Theory and Techniques*, vol. 49, no. 3, pp. 431–441, Mar. 2001.

[110] T. H. Buttgenbach, R. E. Miller, M. J. Wengler, D. M. Watson, and T. G. Phillips, "A broad-band low-noise sis receiver for submillimeter astronomy," *IEEE Transactions on Microwave Theory and Techniques*, vol. 36, no. 12, pp. 1720–1726, Dec. 1988.

[111] B. K. Kormanyos, P. H. Ostdiek, W. L. Bishop, T. W. Crowe, and G. M. Rebeiz, "A planar wideband 80-200 GHz subharmonic receiver," *IEEE Transactions on Microwave Theory and Techniques*, vol. 41, no. 10, pp. 1730–1737, Oct. 1993.

[112] J. M. Edwards, R. O'Brient, A. T. Lee, and G. M. Rebeiz, "Dual-polarized sinuous antennas on extended hemispherical silicon lenses," *IEEE Transactions on Antennas and Propagation*, vol. 60, no. 9, pp. 4082–4091, Sep. 2012.

[113] A. D. Semenov, H. Richter, H. W. Hubers, B. Gunther, A. Smirnov, K. S. Il'in, M. Siegel, and J. P. Karamarkovic, "Terahertz performance of integrated lens antennas with a hot-electron bolometer," *IEEE Transactions on Microwave Theory and Techniques*, vol. 55, no. 2, pp. 239–247, Feb. 2007.

[114] M. A. Elmansouri and D. S. Filipovic, "Lens loading approach for improving ultra-wideband performance of spiral antennas," *IET Microwaves, Antennas Propagation*, vol. 8, no. 12, pp. 937–942, Sep. 2014.

[115] R. Sammeta and D. S. Filipovic, "Improved efficiency lens-loaded cavity-backed transmit sinuous antenna," *IEEE Transactions on Antennas and Propagation*, vol. 62, no. 12, pp. 6000–6009, Dec. 2014.

[116] V. Rumsey, "Frequency independent antennas," in *1958 IRE International Convention Record*, Mar. 1957, vol. 5, pp. 114–118.

[117] Y. Mushiake, "Self-complementary antennas," *IEEE Antennas and Propagation Magazine*, vol. 34, no. 6, pp. 23–29, Dec. 1992.

[118] D. B. Rutledge, D. P. Neikirk, , and D. P. Kasilingam, "Integrated-circuit antennas," in *Millimeter Components and Techniques Part II*, K.J. Button, Ed., vol. 10 of *Infrared and Millimeter Waves*. Elsevier Science, 1983.

[119] J. Dyson, "The equiangular spiral antenna," *IRE Transactions on Antennas and Propagation*, vol. 7, no. 2, pp. 181–187, Apr. 1959.

[120] J. Dyson, "The unidirectional equiangular spiral antenna," *IRE Transactions on Antennas and Propagation*, vol. 7, no. 4, pp. 329–334, Oct. 1959.

[121] P. E. Mayes, "Frequency-independent antennas and broad-band derivatives thereof," *Proceedings of the IEEE*, vol. 80, no. 1, pp. 103–112, Jan. 1992.

[122] B. Cheo, V. Rumsey, and W. Welch, "A solution to the frequency-independent antenna problem," *IRE Transactions on Antennas and Propagation*, vol. 9, no. 6, pp. 527–534, Nov. 1961.

[123] M. A. Elmansouri and D. S. Filipovic, "Pulse distortion and mitigation thereof in spiral antenna-based UWB communication systems," *IEEE Transactions on Antennas and Propagation*, vol. 59, no. 10, pp. 3863–3871, Oct. 2011.

[124] M. A. Elmansouri and D. S. Filipovic, "Low-dispersion spiral antennas," *IEEE Transactions on Antennas and Propagation*, vol. 60, no. 12, pp. 5522–5530, Dec. 2012.

[125] A. Neto, "UWB, non dispersive radiation from the planarly fed leaky lens antenna–Part I: Theory and design," *IEEE Transactions on Antennas and Propagation*, vol. 58, no. 7, pp. 2238–2247, Jul. 2010.

[126] A. Neto, S. Monni, and F. Nennie, "UWB, non dispersive radiation from the planarly fed leaky lens antenna–Part II: Demonstrators and measurements," *IEEE Transactions on Antennas and Propagation*, vol. 58, no. 7, pp. 2248–2258, Jul. 2010.

[127] D. S. Filipovic, T. P. Cencich, and M. W. Nurnberger, "Frequency independent antennas," in *Encyclopedia of RF and Microwave Engineering*. John Wiley & Sons, Inc., 2005.

[128] M. W. Nurnberger and J. L. Volakis, "A new planar feed for slot spiral antennas," *IEEE Transactions on Antennas and Propagation*, vol. 44, no. 1, pp. 130–131, Jan. 1996.

[129] J. L. Volakis, M. W. Nurnberger, and D. S. Filipovic, "Slot spiral antenna," *IEEE Antennas and Propagation Magazine*, vol. 43, no. 6, pp. 15–26, Dec. 2001.

[130] A. Suzuki, Kam A., J. Edwards, G. Engargiola, A. Ghribi, W. Holzapfel, A. T. Lee, X. F. Meng, M. J. Myers, R. O'Brient, E. Quealy, G. Rebeiz, P. Richards, D. Rosen, and P. Siritanasak, "Multi-chroic dual-polarization bolometric detectors for studies of the cosmic microwave background," *Journal of Low Temperature Physics*, vol. 176, no. 5, pp. 650–656, Sep. 2014.

[131] R. O'Brient, P. Ade, K. Arnold, J. Edwards, G. Engargiola, W. L. Holzapfel, A. T. Lee, M. J. Myers, E. Quealy, G. Rebeiz, P. Richards, and A. Suzuki, "A dual-polarized broadband planar antenna and channelizing filter bank for millimeter wavelengths," *Applied Physics Letters*, vol. 102, no. 6, pp. 063506, Feb. 2013.

[132] S. J. C. Yates, J. J. A. Baselmans, A. Endo, R. M. J. Janssen, L. Ferrari, P. Diener, and A. M. Baryshev, "Photon noise limited radiation detection with lens-antenna coupled microwave kinetic inductance detectors," *Applied Physics Letters*, vol. 99, no. 7, pp. 073505, Aug. 2011.

[133] A. Baryshev, J. J. A. Baselmans, A. Freni, G. Gerini, H. Hoevers, A. Iacono, and A. Neto, "Progress in antenna coupled kinetic inductance detectors," *IEEE Transactions on Terahertz Science and Technology*, vol. 1, no. 1, pp. 112–123, Sep. 2011.

[134] A. Neto, N. Llombart, J. J. A. Baselmans, A. Baryshev, and S. J. C. Yates, "Demonstration of the leaky lens antenna at submillimeter wavelengths," *IEEE Transactions on Terahertz Science and Technology*, vol. 4, no. 1, pp. 26–32, Jan. 2014.

[135] J. R. Costa, "Personal communication," July 2014.

[136] G. Carluccio and M. Albani, "Efficient adaptive numerical integration algorithms for the evaluation of surface radiation integrals in the high-frequency regime," *Radio Science*, vol. 46, no. 05, pp. 1–8, Oct. 2011.

[137] D. Pasqualini and S. Maci, "High-frequency analysis of integrated dielectric lens antennas," *IEEE Transactions on Antennas and Propagation*, vol. 52, no. 3, pp. 840–847, Mar. 2004.

[138] E. Heyman and L. Felsen, "High frequency fields in the presence of a curved dielectric interface," *IEEE Transactions on Antennas and Propagation*, vol. 32, no. 9, pp. 969–978, Sep. 1984.

[139] B. Pradarutti, R. Müller, W. Freese, G. Matthäus, S. Riehemann, G. Notni, S. Nolte, and A. Tünnermann, "Terahertz line detection by a microlens array coupled photoconductive antenna array," *Optics Express*, vol. 16, no. 22, pp. 18443–18450, Oct. 2008.

[140] S. Winnerl, "Scalable microstructured photoconductive terahertz emitters," *Journal of Infrared, Millimeter, and Terahertz Waves*, vol. 33, no. 4, pp. 431–454, Apr. 2012.

[141] D. Saeedkia, R. R. Mansour, and S. Safavi-Naeini, "Analysis and design of a continuous-wave terahertz photoconductive photomixer array source," *IEEE Transactions on Antennas and Propagation*, vol. 53, no. 12, pp. 4044–4050, Dec. 2005.

[142] N. Froberg, M. Mack, B. B. Hu, X.C. Zhang, and D. H. Auston, "500 GHz electrically steerable photoconducting antenna array," *Applied Physics Letters*, vol. 58, no. 5, pp. 446–448, Feb. 1991.

[143] S.M. Sze, *Physics of Semiconductor Devices*, Wiley-Interscience publication. John Wiley & Sons Inc., 2nd edition, 1981.

[144] G. Ghione, *Semiconductor Devices for High-Speed Optoelectronics*, Cambrifdge University Press, 1rt edition, 2009.

[145] B. E. A. Saleh and M. C. Teich, *Fundamentals of photonics*, John Wiley & Sons Inc., 2nd edition, 2007.

[146] A. Deninger, "Personal communication," July 2016.

[147] B. Globisch, R. J. B. Dietz, T. Göbel, M. Schell, W. Bohmeyer, R. Müller, and A. Steiger, "Absolute terahertz power measurement of a time-domain spectroscopy system," *Optics Letters*, vol. 40, no. 15, pp. 3544–3547, Aug 2015.

[148] D. Stanze, A. Deninger, A. Roggenbuck, S. Schindler, M. Schlak, and B. Sartorius, "Compact CW terahertz spectrometer pumped at 1.5μm wavelength," *Journal of Infrared, Millimeter, and Terahertz Waves*, vol. 32, no. 2, pp. 225–232, Feb. 2011.

Summary

Towards the Engineering of Pulsed Photoconductive Antennas

In recent years, Terahertz technology has attracted the interest of researchers for its potential applications in a variety of domains. In particular, THz sensing has found application in security screening, medical imaging, spectroscopy, and non-destructive testing. The emergence of all these applications has been driven by the availability of photoconductive antennas, which have made available bandwidth in the THz spectrum at relatively low cost, thanks to several breakthroughs in photonics, and semiconductor technology. Photoconductive antennas are optoelectronic electromagnetic sources that resort to optically pumped semiconductor materials. Such devices exploit the photoconductivity phenomenon to generate and radiate power over a broadband up to the THz frequencies. However, nowadays the use of photoconductive antennas are confined to niche short-range applications, because of the bottleneck of the low power emitted. Early in this research work, it was understood that such bottleneck came from the fact that there was not a clear description about the coupling between the photocondcutive source and the antenna. For this reason, this work has been focused to develop a Thévenin or Norton equivalent circuit for the photoconductor generators of photoconductive antennas.

A Norton equivalent circuit for pulsed photoconductive antennas has been derived, starting by the electrodynamic model of the photogeneration of free carriers in laser pumped semiconductor material. Such equivalent circuit allows to maximize the radiated power as function of the geometry of the gap, the properties of the semiconductor material, and the features of the laser pump, providing a clear description of the coupling between the photoconductor generator and the antenna over the operative bandwidth.

An electromagnetic model of the quasi-optical (source-to-detector) channel, typically used for measuring power and spectrum radiated by photoconductive antennas, has been proposed. Such model jointly with the developed Norton equivalent circuit allows a complete characterization of the power budget from the source to the detector. Providing for the first time a complete description about the dispersion introduced by the quasi-optical channel on the energy spectrum radiated by photoconductive antennas. The entire proposed model (equivalent circuit and channel) has been validated by spectrum and power measurements of photoconductive antenna prototypes.

The proposed equivalent circuit and the electromagnetic model of the quasi-optical channel provide a powerful engineering tool to design photoconductive antennas, opening the way for more standard engineering optimization of wide band laser pumped sources,

resorting to the vast heritage of wide band microwave engineering tools that have been developed mostly for analyzing detectors in radiometric domains.

The radiation performances of logarithmic spiral antennas as feed of dense dielectric lenses has been intensively analyzed. The results of the investigation have demonstrated the presence of the leaky wave radiation, when the spiral antenna are printed at the air dielectric interface, leading to a design of a logarithmic spiral antenna lens antenna, which provides an high aperture efficiency over a decade frequency bandwidth. However, only using extremely thin substrate allows to feed this design with a planar feeding system without limiting the bandwidth. A new design of a logarithmic spiral lens antenna has been proposed for relaxing such limitation, introducing a small air gap between the spiral feed and the bottom lens interface, which enhances the leaky wave radiation. Such new design, coupled with a synthesized elliptical lens, achieves directive patterns without sidelobes over a decade frequency bandwidth. Moreover, the new spiral design can be used also as feed of a hemispherical lens with low extension height, when the dispersion of the radiated pulses has to be minimized.

A novel design for photoconductive sources has been proposed, aiming to increase dramatically the radiated power with respect to the current photoconductive antennas. The new source is based on the well established concept in the microwave community of connected array. Thanks to the intrinsic wide band behavior of the connected array, the proposed solution is able to radiate efficiently the wide band energy spectrum generated by the photoconductive source. Such design is suitable to be employed also as receiver of ultra-wide bandwidth radiation, increasing the sensitivity with respect to the current photoconductive receivers. In order to implement the design of the photoconductive connected array, an ad-hoc biasing network has been proposed, in order to properly bias all the array cells, preserving the connected structure of the elements. Moreover, a design of an optical system has been proposed, in order to optically excite all the elements of the photoconductive array coherently. Using the proposed Norton equivalent circuit for photoconductive generator, a photoconductive connected array generating an average power of 2.35 mW over a bandwidth from $0.1\,\mathrm{THz} - 0.4\,\mathrm{THz}$ has been designed. A demonstrator of the proposed photoconductive source design is going to be realized, and a complete characterization of the prototype will be performed by means of power and spectrum measurements, proving the validity of the concept.

Samenvatting

Naar de Engineering van Gepulste Fotogeleidende Antennes

In de afgelopen jaren heeft terahertz technologie door haar potentiele toepassingen in verscheidene domeinen veel belangstelling verworven bij onderzoekers. Veiligheidsscreening, medische beeldvorming, spectroscopie en niet-destructief onderzoek zijn belangrijke voorbeelden. De verhoogde belangstelling wordt voornamelijk gedreven door verschillende doorbraken in fotonica en de halfgeleidertechnologie waardoor fotogeleidende antennes voor relatief lage kosten toegang geven tot de beschikbare energie in het terahertz spectrum. Fotogeleidende antennes zijn opto-elektronische elektromagnetische bronnen waarvan de werking gebaseerd is op optisch gepompte halfgeleiders. Met zulke instrumenten kan over een grote bandbreedte, tot terahertz frequenties, vermogen gegenereerd en uitgestraald worden dankzij de fotogeleidende eigenschappen. Echter, vandaag de dag is het gebruik van fotogeleidende antennes beperkt tot niche toepassingen, met name toepassingen die werken over korte afstand. De reden hiervoor is het lage vermogen dat de antennes uitstralen. In het begin van dit onderzoek werd dit knelpunt toegewezen aan het feit dat er geen duidelijke beschrijving bestond van de koppeling tussen de fotogeleidende bron en de antenne. Om deze reden focust dit werk zich op de ontwikkeling van een equivalente Thévenin of Norton schakeling van fotogeleidende generatoren en antennes.

Een equivalente Norton schakeling voor gepulseerde fotogeleidende antennes is afgeleid. Het uitgangspunt is het elektrodynamische model van de generatie van vrije ladingdragers in laser gepompte halfgeleiders. Zo'n equivalente schakeling maakt het mogelijk om het uitgestraalde vermogen te maximaliseren als functie van de afmetingen van de opening, de eigenschappen van de halfgeleiders en de kenmerken van de laserpomp. Deze schakeling geeft een heldere beschrijving van de koppeling tussen de generator en de antenne over de gehele operationele bandbreedte.

Een elektromagnetisch model van het quasi optische (bron-naar-detector) kanaal wordt gepresenteerd dat veelal gebruikt wordt om het vermogensspectrum dat wordt uitgestraald door de fotogeleidende antenne te meten. Samen met de ontwikkelde equivalente Norton schakeling maakt dit model het mogelijk om het vermogensbudget volledig te karakteriseren vanaf de bron tot de detector. Voor het eerst wordt een volledige beschrijving gegeven van de frequentiedispersie, die wordt veroorzaakt door het quasi-optische kanaal, op het energiespectrum uitgestraald door de fotogeleidende antennes. Het volledige model (equivalente circuit en kanaal) is gevalideerd door middel van spectrum- en vermogensmetingen van fotogeleidende antenne prototypes.

De voorgestelde equivalente schakeling en het elektromagnetische model van het quasi optische kanaal dienen als een krachtig ontwerp hulpmiddel voor fotogeleidende antennes. Hiermee wordt het mogelijk een meer gestandaardiseerde optimalisatie van breedbandige laser gepompte bronnen uit te voeren, waarbij ook de uitgebreide bestaande kennis betreffende het analyseren van detectors voor radiometrie kan worden gebruikt.

De stralingprestaties van logaritmische spiraalantennes in de nabijheid van diëlektrische lenzen met hoge diëlektrische constante is uitgebreid onderzocht. Het resultaat van dit onderzoek demonstreert de aanwezigheid van lekgolven (English: leaky-waves) wanneer de spiraalantennes gefabriceerd zijn op de lucht-diëlektriek overgang van de lens. Door gebruik te maken van deze lekgolven is er een ontwerp gepresenteerd van een logaritmische spiraalantenne met een hoge efficiëntie over een decade frequentiebandbreedte. Desondanks kan deze bandbreedte alleen werkelijk behaald worden wanneer de antenne gevoed wordt door een vlak voedingsnetwerk in extreem dunne substraten. Om deze limitatie te verkleinen is er een nieuw ontwerp gepresenteerd van een logaritmische spiraal-lensantenne waarin een klein luchtgat tussen de spiraal antenne en de diëlektrische lens wordt geplaatst die de stralingseigenschappen van de lekgolven bevorderd. Een dergelijk ontwerp, samen met een gesynthetiseerde elliptische lens, geeft hoogwaardige stralingspatronen over de volledige decade frequentiebandbreedte. Wanneer de frequentiedispersie van de uitgestraalde puls moet worden geminimaliseerd kan het ontwerp ook gebruikt worden in combinatie met een halfronde sferische lens met een korte extensie.

Een nieuw ontwerp voor fotogeleidende bronnen is voorgesteld met het doel om het uitgestraalde vermogen dramatisch te verhogen in vergelijking met de huidige fotogeleidende antennes. De nieuwe bron is gebaseerd op het, in de microgolf-gemeenschap bekende, concept van verbonden antennestelsels (English: connected arrays). Dankzij de intrinsieke breedbandige eigenschappen van de verbonden antennestels straalt de voorgestelde oplossing efficiënt energie uit over een breedbandige energiespectrum. Zo'n ontwerp kan ook gebruikt worden voor het ontvangen van ultra-breedbandige straling in tegenstelling tot huidige fotogeleidende ontvangers. Om een ontwerp van een fotogeleidende verbonden antennestelsel te implementeren is er een ad-hoc voorspanningsnetwerk netwerk voorgesteld. Verder is er een ontwerp van een optisch systeem voorgesteld zodat alle elementen van een fotogeleidend netwerk coherent optisch aangeslagen kunnen worden. Door de equivalente Norton schakeling te gebruiken is er een fotogeleidende verbonden antennestelsel ontworpen welke een gemiddeld stralingsvermogen van 2.35 mW heeft over een bandbreedte van $0.1\,\mathrm{THz} - 0.4\,\mathrm{THz}$. De geldigheid van het concept zal worden bewezen met een prototype dat zal worden gerealiseerd van de voorgestelde fotogeleidende bron en waarvan een complete karakterisering zal worden uitgevoerd door middel van vermogens- en spectrummetingen.

List of Publications

Journal Papers

J1. S. van Berkel, A. Garufo, N. Llombart and A. Neto, "A Quasi-analytical tool for the characterization of transmission lines at high frequencies," *IEEE Antennas and Propagation Magazine*, vol. 58, no. 3, pp. 82–90, Jun., 2016.

J2. A. Garufo, N. Llombart and A. Neto, "Radiation of logarithmic spiral antennas in the presence of dense dielectric lenses," *IEEE Transactions on Antennas and Propagation*, vol. 64, no. 10, pp. 4168–4177, Oct., 2016.

J3. A. Garufo, G. Carluccio, N. Llombart and A. Neto, "Norton equivalent circuit for pulsed photoconductive antennas Part I: Theoretical model," *IEEE Transactions on Antennas and Propagation*, under review.

J4. A. Garufo, G. Carluccio, J. R. Freeman, D. R. Bacon, N. Llombart, E. H. Linfield, A. G. Davies, and A. Neto, "Norton equivalent circuit for pulsed photoconductive antennas Part II: Experimental validation," *IEEE Transactions on Antennas and Propagation*, under review.

Conference Papers

C1. A. Toccafondi, A. Garufo, C. Della Giovanpaola, "Coplanar waveguide-fed compact antenna for UWB RFID applications," *7th European Conference on Antennas and Propagation (EUCAP 2013)*, Gothenburg, Sweden, April 8–12, 2013.

C2. A. Garufo, N. Llombart and A. Neto, "Enhanced spiral feeds for dielectric lens antenna," *7th European Conference on Antennas and Propagation (EUCAP 2013)*, Gothenburg, Sweden, April 8–12, 2013.

C3. A. Garufo, N. Llombart and A. Neto, "Enhanced radiation properties of spiral lens antennas," *IEEE International Symposium on Antennas and Propagation and USNC-URSI National Radio Science Meeting (APS/URSI 2013)*, Orlando, Florida, USA, July 7–13, 2013.

C4. A. Garufo, N. Llombart and A. Neto, "38th International Conference on Infrared, Millimeter and Terahertz Wave," *IEEE Antennas and Propagation Society International Symposium (IRMMW-THz 2013)*, Mainz, Germany, September 1–6, 2013.

C5. A. Garufo, N. Llombart and A. Neto, "Demonstration of the enhanced radiation in dielectric lens spiral antennas," *8th European Conference on Antennas and Propagation (EUCAP 2014)*, The Hague, Netherlands, April 6–11, 2014.

C6. A. Garufo, N. Llombart and A. Neto, "Improvement of the radiation efficiency in a logarithmic spiral lens antenna," *IEEE International Symposium on Antennas and Propagation and USNC-URSI National Radio Science Meeting (APS/URSI 2014)*, Memphis, Tennesse, USA, July 6–11, 2014.

C7. S. van Berkel, A. Garufo, N. Llombart and A. Neto, "Characterization of printed transmission lines at high frequencies," *9th European Conference on Antennas and Propagation (EUCAP 2015)*, Lisbon, Portugal, April 12–17, 2015.

C8. A. Garufo, G. Carluccio, N. Llombart and A. Neto, "Theoretical model based on spectral Green's function representation for photoconductive slot antennas," *9th European Conference on Antennas and Propagation (EUCAP 2015)*, Lisbon, Portugal, April 12–17, 2015.

C9. A. Garufo, G. Carluccio, N. Llombart and A. Neto, "Spectral Green's function representation for photo-conductive slot antennas," *IEEE International Symposium on Antennas and Propagation and USNC-URSI National Radio Science Meeting (APS/URSI 2015)*, Vancouver, British Columbia, Canada, July 19–24, 2015.

C10. A. Garufo, G. Carluccio, N. Llombart and A. Neto, "Equivalent circuit model based on spectral Green's function representation for photo-conductive slot antennas," *39th International Conference on Infrared, Millimeter and Terahertz Wave (IRMMW-THz 2015)*, Hong Kong, China, August 22–28, 2015.

C11. A. Garufo, G. Carluccio, N. Llombart and A. Neto, "Equivalent Norton circuit model for photo-conductive antennas," *36th ESA Antenna Workshop on "Antennas and RF Systems for Space Science*, ESA/ESTEC, Noordwijk, The Netherlands, October 6–9, 2015.

C12. A. Garufo, G. Carluccio, N. Llombart and A. Neto, "Equivalent Norton circuit model for photo-conductive antennas," *Joint Symposium URSI-Benelux, NARF, and IEEE AP-S Meeting on "Smart Antennas and Propagation*, Enschede, The Netherlands, December 7, 2015.

C13. A. Garufo, G. Carluccio, N. Llombart and A. Neto, "Derivation of an equivalent Norton circuit model for photo-conductive antennas," *10th European Conference on Antennas and Propagation (EUCAP 2016)*, Davos, Switzerland, April 10–15, 2016. (**invited paper**)

C14. A. Garufo, G. Carluccio, N. Llombart and A. Neto, "Design of photo-conductive connected arrays for pulsed terahertz radiation," *10th European Conference on Antennas and Propagation (EUCAP 2016)*, Davos, Switzerland, April 10–15, 2016.

C15. A. Garufo, G. Carluccio, N. Llombart and A. Neto, "Analysis of the power radiation from photoconductive antennas by equivalent Norton circuit model," *IEEE International Symposium on Antennas and Propagation and USNC-URSI National Radio Science Meeting (APS/URSI 2016)*, Fajardo, Puerto-Rico, June 26–July 1, 2016.

C16. A. Garufo, G. Carluccio, N. Llombart and A. Neto, "Photo-conductive connected array solution for pulsed terahertz radiation," *IEEE International Symposium on Antennas and Propagation and USNC-URSI National Radio Science Meeting (APS/URSI 2016)*, Fajardo, Puerto-Rico, June 26–July 1, 2016.

C17. J. R. Freeman, D. R. Bacon, E. H. Linfield; A. Giles Davies, A. Garufo, G. Carluccio, N. Llombart and A. Neto, "Power measurements of photoconductive antennas and comparison with the power estimated by an equivalent circuit model approach," *41st International Conference on Infrared, Millimeter, and Terahertz Waves (IRMMW-THz 2016)*, Copenhagen, Denmark, September 25–30, 2016.

C17. A. Garufo, G. Carluccio, N. Llombart and A. Neto, "Photoconductive connected array: a novel solution for pulsed terahertz radiation," *41st International Conference on Infrared, Millimeter, and Terahertz Waves (IRMMW-THz 2016)*, Copenhagen, Denmark, September 25–30, 2016.

C18. A. Garufo, G. Carluccio, J. R. Freeman, D. R. Bacon, N. Llombart, E. H. Linfield, A. G. Davies, and A. Neto, "Validation by power measurements of a Norton equivalent circuit model for photoconductive antennas," *11th European Conference on Antennas and Propagation (EUCAP 2017)*, Paris, France, April 19–24, 2017.

C19. A. Garufo, G. Carluccio, N. Llombart and A. Neto, "Power measurements of THz radiation from photoconductive antennas for validating a Norton equivalent circuit," *IEEE International Symposium on Antennas and Propagation and USNC-URSI National Radio Science Meeting (APS/URSI 2017)*, San Diego, California, USA, July 9–14, 2017.

C20. A. Garufo, G. Carluccio, J. R. Freeman, D. R. Bacon, N. Llombart, E. H. Linfield, A. G. Davies, and A. Neto, "Characterization of the Quasi-Optical channel for the measurements of the power radited by photoconductive antennas," *42nd International Conference on Infrared, Millimeter, and Terahertz Waves (IRMMW-THz 2017)*, Cancún, México, August 27–September 1, 2017.

C21. A. Garufo, G. Carluccio, N. Llombart and A. Neto, "On the use of equivalent Norton circuit model for photoconductive antennas," *International Conference on Electromagnetism in Advance Applications and IEEE-APS Topical Conference on Antennas*

and Propagation in Wireless Communications (ICEEA-IEEE APWC 2017), Verona, Italy, September 11–15, 2017.

C22. A. Garufo, G. Carluccio, N. Llombart, A. Neto, and I. E. Lager, "Analysis of Photoconductive Antennas Power Radiation by Norton Equivalent Circuit," *European Microwave Week (EuMW 2017)*, Nürnberg, Germany, October 8–13, 2017.

Patents

P1. International patent: Photoconductive Antenna Array, 2017 (Publication no. WO2017023172-A1, Inventors: A. Neto, A. Garufo, G. Carluccio, and N. Llombart).

Thesis Co-Supervised

T1. S. Zhou, "Analysis and design of pulsed photoconductive antennas," M.Sc. thesis, Delft University of Technology, Delft, Netherlands, 2015.

About the Author

Alessandro Garufo was born on April 24$^{\text{th}}$, 1982 in Rome, Italy. He received his B.Sc. and M.Sc. degrees in Telecommunication Engineering from University of Siena, Siena, Italy in October 2007 and April 2012, respectively. For his B.Sc. Thesis, he carried out a six-month internship at Wavecomm, Siena, Italy, from January 2007 to June 2007. From March 2011 to February 2012, he was as an intern in the Antenna Group at Thales Alenia Space, Rome, Italy, where he developed his M.Sc. degree thesis.

From April 2012 until September 2012, he was a researcher in the Applied Electromagnetic Laboratory (LEA) at the University of Siena, Siena, Italy.

From October 2012, he started pursuing his Ph.D. degree at the THz Sensing Group of the Microelectronics department of Electrical Engineering, Mathematics, and Computer Science (EEMCS) faculty at Delft University of Technology, Delft, Netherlands. His Ph.D. topic was about modelling and design of pulsed photoconductive antennas. This research has been carried out under the supervision of Prof. Dr. Ir. Andrea Neto as promotor, Dr. Ir. Nuria Llombart as copromotor, and Dr. Giorgio Carluccio as supervisor. The research has resulted in four journal papers, twenty-two proceedings in international conferences, of which one was an invited paper, and one international patent in 2017. From November 2013 to April 2014, he was a visiting researcher at the Metamaterial and Plasmonic Research Laboratory of Electrical and Computer Engineering faculty at University of Texas, Austin, Texas, United States. His research interests include analytical and numerical method for antennas and transmission lines characterization, design of wideband antennas, dielectric lens antennas, antenna arrays, modelling and design of THz sources based on laser pumped semiconductor.

During his Ph.D., he has co-supervised one M.Sc. student S. Zhou (Delft Univesity of Technology).

He is serving as a reviewer for IEEE Transactions on Antennas and Propagation (IEEE-TAP), IEEE Antennas and Wireless Propagation Letters (IEEE-AWPL), and IEEE Transactions on Terahertz Science and Technology (IEEE-THz).

Acknowledgements

This thesis work would have not been accomplished without the substantial support, and guidance of many people. I consider myself very lucky to have had the chance to work with them.
First of all, I would like to thank my promotor prof. dr. ir. Andrea Neto, who chose me for working in one of the topics of his ERC Grant and for being part of his group as a PhD student. He convinced me to move to the Netherlands with only one Skype call. The door of his office has been always opened and he has been always present for discussion about work and results and for giving feedbacks and support. His enthusiastic approach to research has been very helpful in the difficult moments of my PhD, and I consider me very lucky to have had the chance to have been part of his group. I really appreciated the discussions while we were drinking the coffee early in the morning in the coffee room, when nobody still was at the office.
The second person that I would like to thank is my co-promotor dr. ir. Nuria Llombart, at the beginning of my PhD she taught me many tricks for programming and for realizing all the tools that I used during my PhD, without her guidance all the results shown in this thesis would have been even more difficult to reach. She also explained me how to present myself and the results of the research, which I was pursuing. She has been always present for discussion and also in her case the door of her office has been always opened, even when she was very busy.
This thesis would have never been realized without the daily supervision of dr. Giorgio Carluccio, without his support I would not have been able to come this far. During the last years, we had fun and we have faced together also the difficult moments, when it seemed that the results were impossible to achieve. He has been a mentor but mainly a friend with whom to talk at any moment. We already knew each other before, because we have attended and worked at same university in Italy, but our friendship has been consolidated here in the Netherlands, I have been really lucky to have him as supervisor.
Another person that I would like to thank is prof. Alberto Toccafondi, my supervisor of my master thesis, who suggested me to look for my future beyond the italian borders, and introduced me to prof. Neto.
A special thanks is for Waqas, Ozan, and Bea, who have been part of the first generation of PhD students of the Terahertz Sensing Group together with me. They have been the first people that i knew when i arrived in the Netherlands. They have been excellent office mates and friends, i really enjoyed the time spent together, thanks to them the first years in

the Netherlands have been less tough. Of course, I would like to thank also the other PhD students of the group, Sven, Shahab, Cristina, Alejandro, Marta, Sebastian and Nuri, and all the former and present master students of the group. A particular thanks is for Sven and Sjoerd for the translation of the summary into Dutch. I would like to thank the other colleagues of the group dr. Daniele Cavallo, dr. Erio Gandini, dr. ir. Ioan Lager, and dr. Darwin Blanco. Thanks to Daniele I learnt how to do nice pictures for my presentations, and he also gave me advices for realizing the cover of this thesis, and thanks to Erio I met my girlfriend. I cannot forget to thank also the people of the astronomic instrumenation of the group, dr. ir. Jochem Baselmann, dr. Juan Bueno, dr. Akira Endo, dr. Kinichi Karatsu, and ir. David Thoen, for their suggestions, the assembly of the components of the prototypes, and for having made me use their instrumentations for the characterization of the detector.

I would like to dedicate my thesis to my family, my parents Ignazio and Simonetta and my brother Lorenzo. They are my real pillars on which I support, they always encouraged to pursue my dreams, even if they would have taken me far away from them. The physical distance between us does not really matter, because i know that you are always close to me, i will be always grateful for your example and all your sacrifices. To my brother, I am really sorry for having missed all your theater plays in the last years, but I know that you are doing well, keep up like this.

Vorrei dedicare questa tesi alla mia famiglia, i miei genitori Ignazio e Simonetta, e a mio fratello Lorenzo. Loro sono i veri pilastri su cui mi sorreggo, mi hanno sempre incoraggiato a perseguire i miei sogni, anche se questi mi avrebbero portato lontano da loro. La distanza fisica tra noi non conta veramente, perché so che siete sempre vicino a me, vi saro sempre grato per il vostro esempio e tutti i vostri sacrifici. A mio fratello, mi dispiace molto per aver mancato a tutti i tuoi spettacoli teatrali in quest'ultimi anni, ma so che stai andando bene, continua così.

Finally, I would like to thank my girlfriend Carol, you have been always close to me in the last two and half years, you have always supported me and you always kept me with the feet on the ground. Thanks to your presence I have always felt at home. Without you and your smile, I would have never accomplished this goal, this thesis is also dedicated to you. Now that this stage of life is close, I am looking forward to see what the future reserves to us.